Biomedical imaging and therapy with physically and physiologically tailored magnetic nanoparticles

Amit Praful Khandhar

A dissertation
submitted in partial fulfillment of the
requirements for the degree of

Doctor of Philosophy

University of Washington

2013

Reading Committee:
Kannan M. Krishnan, Chair
Christine K. Luscombe
Xiaoming Yang
Julian A. Simon

Program Authorized to Offer Degree:
Materials Science & Engineering

University of Washington

Abstract

Biomedical imaging and therapy with physically and physiologically tailored magnetic nanoparticles

Amit Praful Khandhar

Chair of the Supervisory Committee:
Professor Kannan M. Krishnan
Materials Science & Engineering

Magnetic particle imaging (MPI) and magnetic fluid hyperthermia (MFH) are emerging imaging and therapy approaches that have the potential to improve diagnostic safety and disease management of heart disease and cancer – the number 1 and 2 leading causes of deaths in the United States. MPI promises real-time, tomographic and quantitative imaging of superparamagnetic iron oxide nanoparticle (SPION) tracers distributed *in vivo*, and is targeted to offer a safer angiography alternative for its first clinical application. MFH uses ac-fields to dissipate heat from SPIONs that can be delivered locally to promote hyperthermia therapy (~42°C) in cancer cells.

Both technologies use safe radiofrequency magnetic fields to exploit the fundamental magnetic relaxation properties of superparamagnetic iron oxide nanoparticles (SPIONs), which must be tailored for optimal imaging in the case of MPI, and maximum hyperthermia potency in the case of MFH. Furthermore, the magnetic core and shell of SPIONs are both central to the optimization process; the shell, in particular, bridges the translational gap between the optimized core and its safe and effective use in the physiological environment. Unfortunately, existing SPIONs that were originally designed as

MRI contrast agents lack the basic physical properties that enable the clinical translation of MPI and MFH.

In this work, the core and shell of monodisperse SPIONs were optimized in concert to accomplish two equally important objectives: (1) biocompatibility, and (2) MPI and MFH efficacy of SPIONs in physiological environments. Critically, it was found that the physical and physiological responses of SPIONs are coupled, and impacting one can have consequences on the other. It was shown that the poly(ethylene glycol) (PEG)-based shell when properly optimized reduced protein adsorption to SPION surface and phagocytic uptake in macrophages – both prerequisites for designing long-circulating SPIONs. In MPI, tailoring the surface coating reduced protein adsorption and improved colloidal stability, which were critical in retaining the magnetization relaxation properties of the SPIONs. The improvements in surface coatings enabled the use of larger SPION cores (> 20 nm core diameter), which were used to demonstrate benchmark-imaging performance in some of the world's first MPI scanners at Philips Medical Imaging and University of California, Berkeley. In MFH, it was shown for the first time that optimization of heat loss from SPIONs (W/g) is possible by tailoring the core size and size distribution for the given ac-field conditions. Biodistribution and blood circulation studies in mice showed that SPIONs accumulated primarily in the liver and spleen with minimal renal involvement, and demonstrated gradual clearance. Circulation time was evaluated using the MPI signal detected over time in blood, which offered insight on the relevant circulation time for angiography applications. In comparison with carboxy-dextran coated Resovist® SPIONs, the PEG-coated SPIONs developed in this work circulated substantially longer; furthermore, reducing the hydrodynamic diameter showed a 4.5x improvement in blood half-life.

The work presented in this thesis demonstrates that the combined effort in optimizing the core and shell properties of SPIONs enhances biocompatibility and efficacy, with the *in vivo* studies providing critical feedback on the success (or failure) of the optimization process. Future work will entail designing functionalized SPIONs for target-

ing specific disease sites, which will further enable the molecular level diagnosis and therapy of diseases.

TABLE OF CONTENTS

Page

ACKNOWLEDGEMENTS

First, the author would like to thank his advisor, Prof. Kannan M Krishnan, for providing generous support and direction for this thesis. Prof. Krishnan is an excellent educator and role model, but his support has often gone beyond education. He puts a genuine focus on balancing life and work, and has enthusiastically looked after the interests of his students. The author thanks Prof. Krishnan in giving the opportunities to continue pursuing the commercialization of the work presented in this thesis.

The author thanks the National Institutes of Health (NIH) and the National Institutes of Biomedical Imaging and Bioengineering (NIBIB) for providing the financial support to conduct this work.

For their collaborative research support, the author thanks Dr. Julian A Simon and his research group at Fred Hutchinson Cancer Research Center for providing access to cell culture facilities and scientific discussions. The author also thanks Dr. Steven Conolly and his group at University of California, Berkeley, and the research group at Philips Medical Imaging (Hamburg, Germany) for providing access to MPI scanners.

The author is extremely grateful for his fellow group members, especially Dr. R. Matthew Ferguson and Hamed Arami, for their support and making those long hours in the lab worthwhile.

Finally, the author thanks his near friends and family, especially his wife Rutu, for their unconditional love, and believing in his academic endeavors.

LIST OF FIGURES

Abbreviated captions Page

LIST OF TABLES

Abbreviated captions Page

GLOSSARY

ATP: Adenosine Triphosphate – the molecule responsible for the storage and generation of energy in cells.

BD: Biodistribution – a study used to determine the distribution and accumulation of materials in an *in vivo* model.

CHD: Coronary Heart Disease – a disease that affects blood flow to the heart due to narrowing of the coronary arteries.

CIN: Contrast induced Nephropathy – an impairment of kidney function that is prevalent after intravenously administering iodinated contrast media to patients with chronic kidney disease.

CKD: Chronic Kidney Disease – a condition characterized by a gradual loss of kidney function.

CT: (x-ray) Computed Tomography – an x-ray based imaging modality that produces image slices of the scanned region of interest.

DLS: Dynamic Light Scattering – also known as photon correlation spectroscopy, it is a technique used to measure the hydrodynamic size of particles dispersed in a liquid.

FFP: Field-free point – a point of zero magnetic field generated by electromagnets in MPI scanners; it is the point sensitive to the presence of SPIONs.

ICM: Iodinated Contrast Media – contrast agents used in x-ray CT angiography to highlight lumina of blood vessels.

LDH: Lactate dehydrogenase – an enzyme present inside viable cells; an LDH assay is a quantitative measure of cell toxicity, determined from the amount of extracellular LDH.

LRT: Linear Response Theory

MFH: Magnetic Fluid Hyperthermia

MPI: Magnetic Particle Imaging

MPS: Magnetic Particle Spectrometer

PEG: Poly(ethylene glycol) – a biocompatible polymer containing ethylene oxide as the repeating unit.

PK: Pharmacokinetics – a study that helps determine the *in vivo* circulation kinetics, such as blood half-life, of intravenously administered materials.

PMAO: Poly(maleic anhydride-alt-1-octadecene) – a block co-polymer containing alternating units of maleic anhydride and octadecene.

RES: Reticuloendothelial System – also known as the mononuclear phagocytic system, it is part of the immune system that contains phagocytic cells – monocytes and macrophages – housed mainly in the liver, spleen, lymph nodes and bone marrow.

RPMI: Roswell Park Memorial Institute media – a cell culture growth medium.

SPIONs: Superparamagnetic Iron Oxide Nanoparticles

TEM: Transmission Electron Microscopy

VSM: Vibrating Sample Magnetometer

DEDICATION

To Mom and Dad

Chapter 1.

INTRODUCTION

Superparamagnetic iron oxide nanoparticles (SPIONs) have a history of clinical use, most notably as magnetic resonance imaging (MRI) contrast agents for detecting liver lesions. In MRI, SPIONs are used as ‘negative’ contrast agents – they diminish the pre-existing signal emanating from tissues, thereby resulting in dark image contrast. However, negative contrast is often difficult to interpret in the presence of ubiquitous background signal from tissues; thus the clinical use of SPION-based MRI has been short-lived, ultimately leading to discontinuation of all commercial SPION contrast agents. On the other hand, clinical interest for novel technologies that exploit the intrinsic properties of SPIONs, such as magnetic particle imaging (MPI) and magnetic fluid hyperthermia (MFH), is growing. Though the intended clinical outcomes of MPI and MFH are clearly distinct, yet complementary, both technologies rely on the unique magnetic properties of SPIONs – MPI exploits the magnetization reversal dynamics of SPIONs for diagnostic imaging, while MFH harnesses the same process to generate heating for cancer therapy. Unfortunately, the lack of biocompatible SPIONs with magnetic properties tailored specifically for MPI and MFH impedes the clinical translation of these novel technologies. The challenge here is *not* the inability to synthesize SPIONs with tailored magnetic properties or rendering them biocompatible – both have been accomplished as separate goals – but to balance the two whilst ensuring that SPIONs deliver optimal MPI or MFH performance within the constraints imposed by the physiological environment. It turns out that the physical and physiological optimizations of SPIONs are not mutually exclusive processes; thus, it is critical that these are carried out in concert.

Previous work conducted in our group in optimizing SPIONs for MPI (R. M. Ferguson, PhD thesis 2012) and MFH (M. Gonzales-Weyhmiller, PhD thesis 2007) has focused on tuning the magnetic core properties of SPIONs by controlling their size and size distribution. In this work, SPIONs were tuned for optimal MPI and MFH performance and further engineered to translate their optimal performance *in vitro*, and ultimately to the more realistic *in vivo* system. It will be shown that due to the numerous physical and physiological limits (Chapter 2 and Chapter 3), both the superparamagnetic core and the biocompatible polymer shell are integral components that determine the final MPI or MFH performance. Critically, the polymer shell bridges the translational gap between optimizing the magnetic core and its *safe and efficient* use in the body; as a result, a polymer shell that preserves the optimized magnetic properties in the physiological environment was developed (Chapter 4 and Chapter 5). Finally, *in vivo* biodistribution of SPIONs and their blood circulation time pertaining to MPI angiograms were evaluated in a rodent model (Chapter 6).

The following sections provide the clinical motivations – heart disease (§1.1) and cancer (§1.2) – for MPI and MFH and their potential impact on diagnostics and therapy, followed by an outline and scope of this thesis (§1.3).

1.1 MOTIVATION – HEART DISEASE

MPI is an emerging real-time, highly sensitive and quantitative imaging modality that uses safe magnetic fields (no ionizing radiation) for imaging SPION tracer distributions [1]. Table 1-1 highlights the characteristics and the fairly competitive position of MPI in comparison with existing imaging modalities – a prerequisite for introducing any new technology. Another crucial prerequisite for the successful introduction of new clinical procedures is their potential to improve patient safety and healthcare. For its first clinical application, MPI is initially being developed as a safer angiography alternative for diagnosing coronary heart disease (CHD) – the leading cause of deaths in the United States according to the National Vital Statistics Report released in 2011 (Figure 1-1) [2]. In angiography procedures, contrast agents highlight lumina of coronary arteries and aid in delineating occlusions (blockages) or aneurysms (abnormal widening) that may affect blood flow in the heart.

Table 1-1. Comparison of MPI with existing imaging modalities (modified from [3]). Spatial resolution and sensitivity of MPI are theoretical predictions.

	Radiation	Spatial resolution	Temporal resolution	Contrast agent (~qty. used)	Sensitivity [mol/L]	Summary
Positron Emission Tomography (PET)	γ-rays	1-2mm	s to min	Radio-isotopes (ng)	10^{-12}-10^{-11}	Sensitive; quantitative; many probes available; no tissue contrast; short probe shelf-life (min-hrs) – requires cyclotron
Single-photon Emission Computed Tomography (SPECT)	γ-rays	1-2mm	min	Radio-isotopes (ng)	10^{-11}-10^{-10}	
X-ray angiography	x-rays	50-200µm	s to min	ICM (mg-g)[a]	-[b]	Angiography requires catheterization; background tissue noise; fast
Magnetic Resonance Imaging (MRI)	DC-field & radiowaves	25-100µm	min to hr	GdBCA (g)[a]	10^{-5}-10^{-3}	Highest spatial resolution; background tissue noise; slow
Magnetic Particle Imaging (MPI)[c]	DC-field & radiowaves	200-500µm	s to min	SPIONs (µg-mg)[d]	10^{-9}-10^{-6}	Quantitative with good sensitivity; no tissue contrast; fast

a – typical dose used in angiograms
b – not well characterized
c – spatial resolution & sensitivity of MPI are theoretical estimates
d – estimate for angiograms

The current standard in coronary angiography uses x-rays to image iodinated contrast medium (ICM) administered through an arterial catheter; computed tomography (CT) angiography is an alternative that does not require catheterization but still uses x-rays and intravenously administered ICM. In addition to the safety concerns associated with high doses of radiation exposure to both patients and physicians, there are significant risks associated with the use of ICM agents in x-ray angiography. Since ICM agents undergo renal clearance, patients with impaired renal function or chronic kidney disease (CKD) are at a high risk of contrast induced nephropathy (CIN) [4] – commonly defined as the occurrence of acute renal failure within 48 hours of exposure to contrast material. Furthermore, CKD is prevalent with age (nearly 25% of persons over 65 in the

U.S. have CKD [5]), diabetes (~33%) and hypertension (~21%) [4] – all significant risk factors for developing CHD. Thus, the coincidence of CKD and CHD suggests a large population that would benefit from angiograms is also at a high risk of developing some degree of CIN due to angiography procedures.

MPI promises a safer alternative to the CKD population because it uses SPION tracers for generating images, which do not undergo renal clearance like ICM and Gadolinium-based T1 contrast agents (GdBCAs) used in MR-angiography (MRA) [6,7]. SPIONs are significantly larger than molecular contrast agents – the total (hydrodynamic) size can range from 20-150 nm [diameter] [6] – and escape filtration through the 6-15 nm fenestrae found in kidney glomeruli [8]. Depending on the hydrodynamic size and surface characteristics, circulation times may vary, but most SPION formulations are eventually cleared by the mononuclear phagocytic system: a collection of phagocytic cells housed in the liver, spleen and lymph nodes (Chapter 3). To further highlight the safety of SPIONs for CKD patients, Feraheme™ (ferumoxytol), a dextran-coated iron oxide nanoparticle formulation (30 nm hydrodynamic diameter [6]) administered as two 510 mg IV injections was approved in 2009 specifically for iron replacement therapy in CKD patients [9]. In addition to negligible renal involvement, SPIONs designed to circulate in blood for long periods may not require cardiac catheterization, but can be safely administered intravenously, and offer both, first-pass and blood pool imaging opportunities.

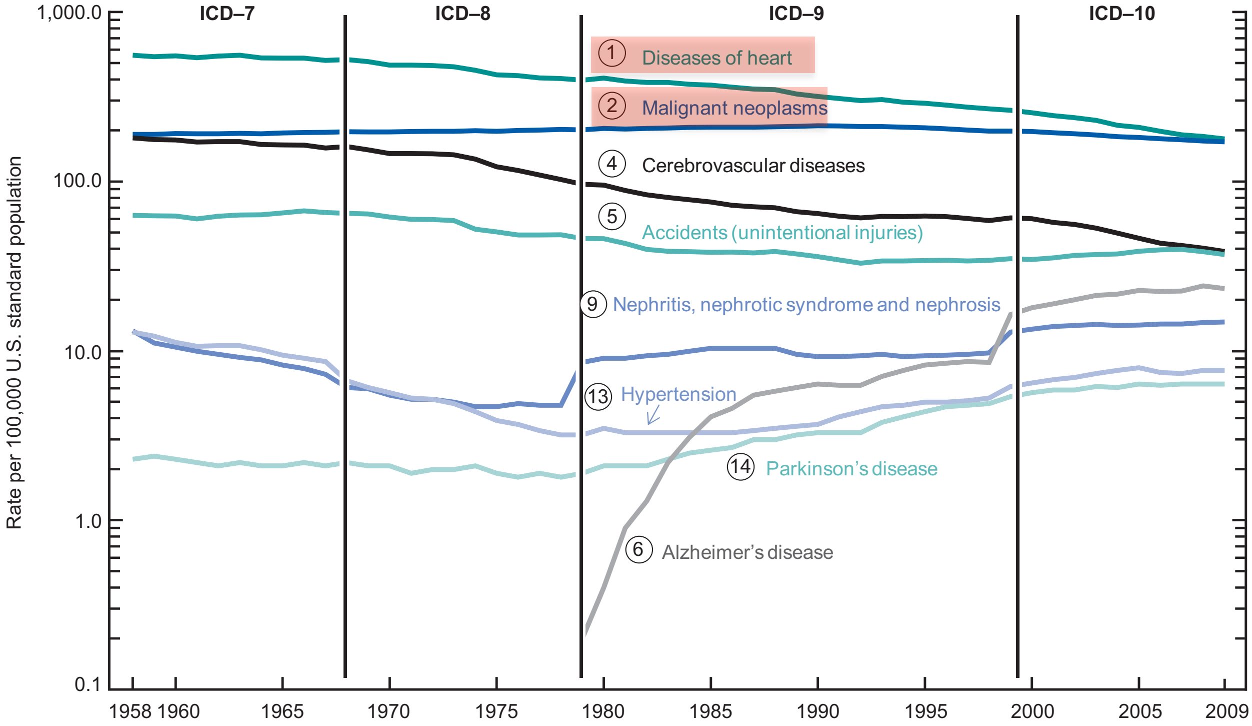

NOTES: ICD is the *International Classification of Diseases*. Circled numbers indicate ranking of conditions as leading causes of death in 2009.
SOURCE: CDC/NCHS, National Vital Statistics System, Mortality.

Figure 1-1. Age-adjusted death rates for selected leading causes of death: United States, 1958-2008 (adapted from [2])

The physical basis of MPI using SPIONs is fundamentally different from MRI; as a result, existing SPIONs optimized for MRI are grossly inadequate for MPI. Unlike MRI, where the large magnetic moment of SPIONs increases T2-relaxivity of nearby protons to enhance negative tissue contrast, MPI exploits the characteristic nonlinear magnetization of SPIONs to construct high temporal (millisecond time-scales) and spatial resolution (sub-mm) images of nanoparticle distributions. Physical simulations and models [10-12] suggest the possibility of sub-mm resolution and nanomolar sensitivity in MPI, while experimental results [13,14] show that micromolar sensitivity and ~1 mm resolution are already attainable [1]. However, as demonstrated in the work presented here, further development and clinical validation of MPI requires tailoring the magnetic properties of SPIONs for optimal performance in physiologically relevant *in vivo* environments.

1.2 MOTIVATION – CANCER

In 2009, cancer was still the second leading cause of deaths in the US behind heart disease, but trends indicate that it will soon surpass it (Figure 1-1). Conventional therapy typically requires surgical removal of the tumor mass (if its location is known) as the first option, followed by high doses of chemotherapy, radiation or a combination of the two; high doses are required to effectuate a therapeutic outcome, but often result in adverse side effects that cause severe patient discomfort. Alternatively, the potency of chemo- and radiotherapies can be increased using adjuvant therapies, ultimately lowering their effective dose and alleviating the subsequent side effects. One approach is to heat cancer cells, typically to ~ 42-46°C, to disrupt cellular metabolism, which is long known to improve the effectiveness of the above mentioned conventional therapies [15-17]. The challenge, however, is to restrict heating to the disease site in order to minimize non-specific heating of healthy tissue. Magnetic Fluid Hyperthermia (MFH) – the heating of SPIONs under the influence of ac-fields (§2.3) – offers the possibility of focusing hyperthermia therapy to the affected site through active or passive targeting of SPIONs to the disease site [18-23]. Active targeting requires surface conjugation of targeting moieties that have specific binding affinity for over-expressed receptors on tumor cells [24]; on the other hand, an example of passive targeting is the enhanced permeability and retention (EPR) of SPIONs in tumors due to the leaky tumor vascular network that is coupled with poor drainage to the lymphatic system [25]. However, there are several fundamental steps that must be achieved before MFH can be successfully implemented; particularly, the heating capacity of SPIONs must be maximized for a given amount of material. The latter is crucial since the localization of nanoparticles at the disease site is typically low due to the host of pre-existing physiological barriers encountered *in vivo* (Chapter 3).

Like MPI, MFH exploits the fundamental magnetic properties of SPIONs. Details are provided in §2.3, but briefly, the ac-field performs 'excess' work on the magnetization that gets released in the form of heat. Critically, to optimize the amount of heat released over time, per mass of material (also called the specific loss power (SLP); W/g), the magnetization response of the SPIONs must be tuned for the given ac-field conditions. Thus far, MFH has been studied in both *in vitro* [20,23,26-28] and *in vivo* [20,27] platforms, but without much effort devoted to tailoring SPION properties for optimum performance. Since magnetization response depends on SPION size, it is assumed that SLP is also size-dependent. Furthermore, magnetization response of SPIONs varies with field conditions; thus, the key question is whether there is an optimum size for a given set of ac-field conditions. For safety reasons, ac-field parameters are constrained – earlier experiments indicated that the product of frequency (f) and amplitude (H_o) must be less than $5x10^9$ $Am^{-1}s^{-1}$ to prevent non-specific inductive heating of tissues [29]. In this work, a dedicated commercially available MFH system operating at f = 375 kHz and H_o = 17 $mT\mu_o^{-1}$ (f *H_o ~ $5x10^9$ $Am^{-1}s^{-1}$) was used to determine whether SLP is indeed size-dependent and how well experimental results match with theoretical predictions. The work presented in this thesis focuses on tuning the physical properties of SPIONs (size and size distribution) for optimizing SLP for the chosen set of ac-field conditions, and further demonstrating hyperthermia efficacy in cancer cells.

1.3 THESIS OUTLINE AND SCOPE

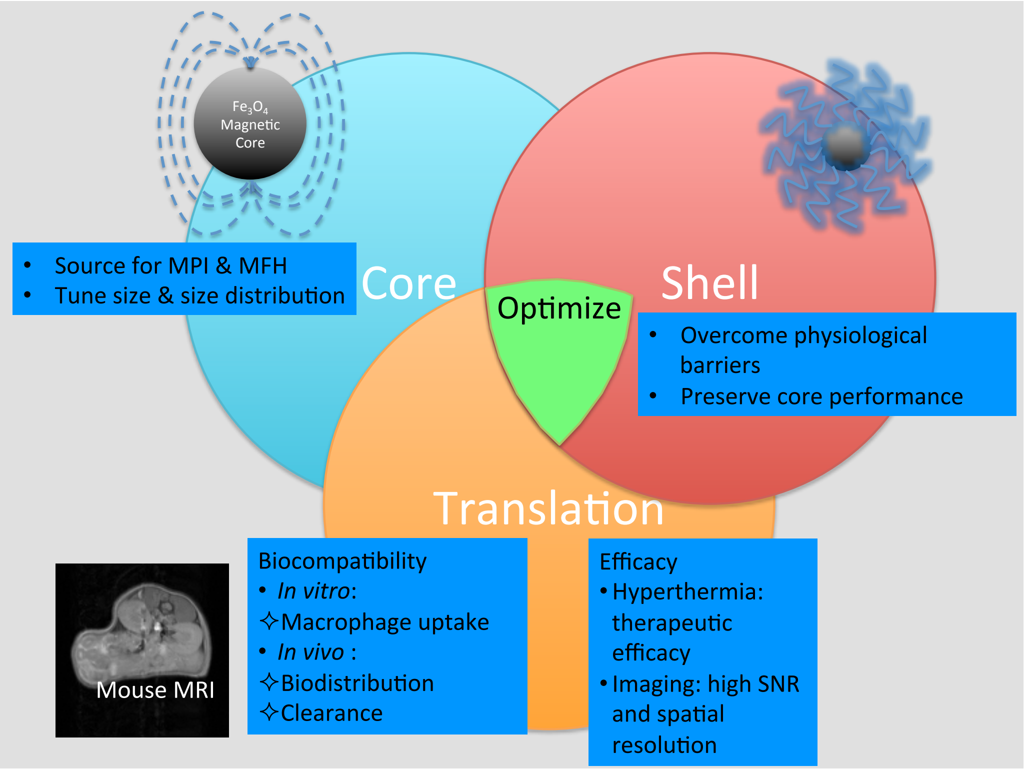

Figure 1-2. Thesis outline and scope: the main objectives of this work are to optimize the core and shell properties of SPIONs to demonstrate (1) biocompatibility and (2) MPI and MFH efficacy in physiological environments.

The work discussed in this thesis is graphically outlined in Figure 1-2. First, we describe some of the physics of superparamagnetism that underline the working principles of MPI and MFH (Chapter 2). The goal here is to highlight the significance of SPION (specifically, superparamagnetic magnetite: Fe_3O_4) size and size distribution in optimizing MPI and MFH performance. Next, we consider the physiological barriers that lay down the criteria for designing biocompatible long-circulating SPIONs; critically, the role of the polymer surface coating is highlighted. The polymer shell must (1) render the SPIONs biocompatible and safe for physiological use and (2) retain the magnetic properties of the core – responsible for MPI and MFH – in physiological environments. In this work, a PEG-based amphiphilic polymer was used to disperse monodisperse, yet hydrophobic, SPIONs in the aqueous phase (synthesis and characteristics are discussed in 4.1). Colloidal stability in biological media (§4.2.2), *in vitro* phagocytic uptake (§4.2.3) and cytotoxicity (§4.2.4) were evaluated to demonstrate the overall biocompatibility of the SPIONs. As mentioned above, both biocompatibility and efficacy are equally important, thus MPI performance of SPIONs was evaluated in serum-rich biological media, gel and blood to simulate the various physiological environments. For MFH, the efficacy of hyperthermia therapy in cancer cells was evaluated *in vitro*. Finally, biodistribution and blood circulation characteristics, with specific relevance to MPI angiography, were evaluated in a rodent model. The main objectives of this work are to optimize the core and shell properties of SPIONs to demonstrate both biocompatibility and efficacy in physiological environments. However, demonstrating complete safety, which requires statistically rigorous animal studies, is not in the scope presented here. It should be noted, however, that the *in vivo* studies presented here demonstrate basic biocompatibility and are the first of many steps towards achieving clinical translation.

Chapter 2.

THE PHYSICS OF MPI AND MFH

Magnetite ($Fe^{2+}Fe_2^{3+}O^{2-}_4$) consists of both ferrous (Fe^{2+}) and ferric (Fe^{3+}) ions, which are arranged in the inverse spinel structure (Figure 2-1(a)). The unit cell is face-centered cubic constructed from 32 O^{2-} ions packed in the [111] direction, 8 Fe^{2+} ions occupying the octahedral sites and 16 Fe^{3+} ions distributed equally between octahedral and tetrahedral sites. The magnetic moments of the Fe^{2+} and Fe^{3+} ions are arranged in an antiparallel alignment, and their unequal magnitudes gives rise to a net non-zero magnetic moment per unit cell, which gives bulk magnetite its characteristic ferrimagnetic properties. Similar to ferromagnets, ferrimagnetic materials have multiple domains and exhibit spontaneous magnetization below the Curie temperature (850 K for magnetite [30]), and also show magnetic hysteresis in response to an external field – a phenomenon characterized by a non-zero coercive field ($\mu_o H_C$) and remnant magnetization (M_R) (Figure 2-2 (a)). However, below the critical single domain size (d_{sd}), multiple domains cease to exist because the exchange energy cost of maintaining a domain wall is greater than the competing anisotropy energy, which aligns magnetization in preferred directions determined by the relative contributions from magnetocrystalline and shape energy densities [31]. Further reduction in size results in superparamagnetism – a thermally excited state where the magnetization response to an external field, for a given measurement time, is nonlinear – characterized by the Langevin theory of paramagnetism [32,33] – and shows non-hysteretic behavior, i.e. both the coercive field and remnant magnetization are zero (Figure 2-2 (b)).

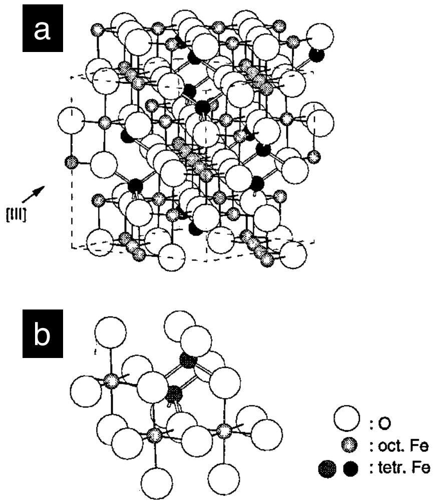

Figure 2-1. Adopted from [30]. (a) Ball-and-stick model showing the cubic inverse spinel structure of magnetite. 8 Fe^{2+} ions occupy the octahedral sites and 16 Fe^{3+} ions are distributed equally between octahedral and tetrahedral sites. Unit cell is outlined using dashed line. (b) A closer look shows that an octahedral site is coordinated by 6 O^{2-} ions and 4 O^{2-} ions for a tetrahedral site.

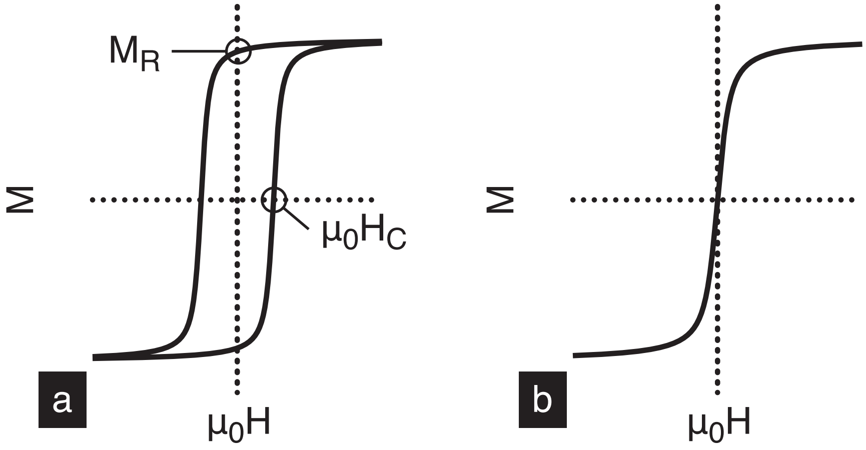

Figure 2-2. Similar to ferromagnetic materials, ferrimagnetic materials have a net non-zero magnetization below the Curie temperature, and show (a) hysteresis or an open loop magnetization response to the applied field. The magnetization requires a coercive field ($\mu_0 H_c$) to reverse magnetization and shows remanence (M_R) in the absence of a field. (b) Below a critical size, however, the magnetization becomes thermally unstable, resulting in superparamagnetism. The magnetization shows no hysteresis, but a nonlinear response that is described by the Langevin function for paramagnetism.

Superparamagnetism is a nanoscale phenomenon that is observed in magnetite (Fe_3O_4) particles smaller than ~30 nm in diameter [32], and forms the physical basis for biomedical applications of SPIONs. The characteristic nonlinear magnetization response of SPIONs to an external field is central to their applications in both MPI and MFH. In the following sections, we will consider the physics of magnetization reversal in SPIONs, the various parameters that influence reversal, and ultimately, the theoretical and practical relevance of magnetization reversal to MPI and MFH. Finally, it should be mentioned that in addition to the critical role of superparamagnetism in MPI and MFH physics, it also offers some practical utility – the zero remnant magnetization of SPIONs in the absence of an external field prevents agglomeration in solution or when administered *in vivo*, which would otherwise induce an immunogenic response (§3.1) or even block blood flow in capillaries due to the larger hydrodynamic size of aggregated SPIONs.

2.1 NANOPARTICLE RELAXATION AND SUPERPARAMAGNETISM

Depending on the field and temperature conditions, magnetization reversal in single domain superparamagnetic particles is explained either by the linear response theory (LRT) (§2.1.2) [34,35] or the Stoner-Wohlfarth model (§2.1.3) [36,37]. The LRT is valid in low field conditions ($H \rightarrow 0$), whereas the Stoner-Wohlfarth model assumes the temperature $T \rightarrow 0$. When considered separately, the assumptions are invalid for MPI and MFH applications, where both H and T are non-zero; however, a combined treatment of the two will help lay the foundation for magnetization reversal in single domain nanoparticles.

Before tackling the details of the two theories in the presence of external fields, a general description of a typical single domain nanoparticle and its magnetization relaxation characteristics in the absence of external fields is necessary. Consider the single domain nanoparticle in Figure 2-3(a) of volume V_c [m^3] and a saturated magnetic moment [Am^2] per unit volume, M_s [A/m], resulting from the exchange coupling between individual atomic spins in the nanoparticle. The preferred or 'easy' directions of magnetization are determined by the effective magnetic anisotropy energy density K_{eff} [J/m^3]. The latter is a material property of either crystalline or shape origin; nanoparticles have an additional contribution from surface spins due to the large surface area to volume ratio. For simplicity, we neglect its origin and assume the effective anisotropy is uniaxial, which results in two preferred magnetization directions as indicated by the dashed line in Figure 2-3(a). In the absence of an external field (H = 0 Tμ_0^{-1}), the magnetic energy is predominantly determined by the effective anisotropy, which for the uniaxial case varies sinusoidally with θ – the angle between the magnetic moment and easy axis – such that $E_{anisotropy} = K_{eff}V_c \sin^2(\theta)$ (Figure 2-3 (b)). The energy of the system is minimum when M_s is aligned either parallel ($\theta = 0$) or antiparallel ($\theta = \pi$) with the easy axis, while the energy maximum, also called the energy barrier (ΔE) to switch between the two easy directions is $K_{eff}V_c$ – it is located at $\theta = \pi/2$, which is the 'hard axis' of magnetization for the uniaxial case.

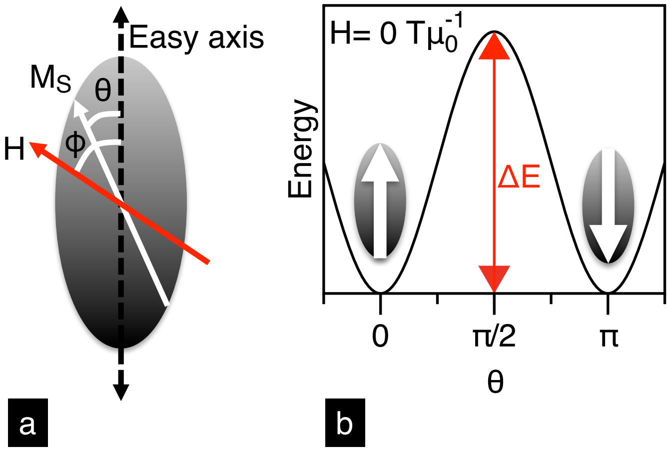

Figure 2-3. (a) A single domain nanoparticle with uniaxial anisotropy. (b) The magnetic energy profile in zero field, where the energy barrier, *ΔE*, depends solely on the anisotropy energy.

In the subsequent sections, we will consider nanoparticle relaxation mechanisms in the absence of a field and conditions that dictate whether or not a single domain particle is superparamagnetic. Finally, we will examine the magnetization reversal processes in the presence of non-zero alternating magnetic fields to simulate conditions encountered in MPI and MFH applications.

2.1.1 Néel and Brownian relaxation

When the thermal energy, k_bT (~ 25 meV at T = 298 K), is large enough to overcome the energy barrier ($K_{eff}V_c/k_bT < 1$), the single domain uniaxial particle in Figure 2-3(a) is thermally excited and is referred to as magnetically 'unblocked'. In this condition, and in the absence of an external field, magnetization direction alternates between parallel and anti-parallel alignment with respect to the easy axis. The atomic spins rotate coherently inside the particle at a rate given by the Néel relaxation time τ_N [38]:

$$\tau_N = \tau_0 \exp\left(\frac{K_{eff}V_c}{k_bT}\right)$$

Eq. 2-1

where τ_o is the attempt time typically in the range of 10^{-9}-10^{-11} seconds [38]. For a spherical particle of core diameter d_c, Eq. 2-1 becomes:

$$\tau_N = \tau_0 \exp\left(\frac{K_{eff}\pi d_c^3}{6k_bT}\right)$$

Eq. 2-2

On the other hand, when $K_{eff}V_c/k_bT > 1$, the magnetization is blocked in the easy axis direction. As a result, when a static field is applied, the particles must physically rotate to align the easy axis with the field direction. *The time it takes for the particles to randomize their easy axes once the field turns off is called the Brownian relaxation time – particles relax due to rotational diffusion and random collisions*. In this particular case, the energy barrier is a combination of drag forces that resist the rotation process, such as the solution's viscosity (η) and the nanoparticle's hydrodynamic volume (V_h); thus, the Brownian relaxation time constant (τ_B) in the absence of a field is expressed as:

$$\tau_B = \frac{3\eta V_h}{k_b T}$$

Eq. 2-3

For a spherical nanoparticle with a uniform shell thickness, t, the Brownian relaxation time can be expressed as a function of the core diameter d_c:

$$\tau_B = \frac{4\eta\pi\left(\frac{d_c}{2} + t\right)^3}{k_b T}$$

Eq. 2-4

In summary, Eq. 2-2 and Eq. 2-4 give us the two fundamental magnetization relaxation times of nanoparticles in solution in the absence of an external field; critically, the interplay between thermal energy and the anisotropy energy barrier dictates the dominant magnetization reversal mechanism. When the thermal energy is greater than the anisotropy energy barrier, magnetization is unblocked and Néel relaxation occurs via coherent reversal of magnetization inside the particle; on the other hand, when the thermal energy is less than the anisotropy energy barrier, magnetization is blocked in the easy axis direction and Brownian relaxation occurs via physical rotation of the entire particle. Figure 2-4 shows a plot of the two time constants associated with each relaxation mechanism as a function of nanoparticle diameter; the shorter of the two times determines the relaxation mechanism, and the effective relaxation time (τ_{eff}) near the transition region is given by:

$$\frac{1}{\tau_{eff}} = \frac{1}{\tau_N} + \frac{1}{\tau_B}$$

Eq. 2-5

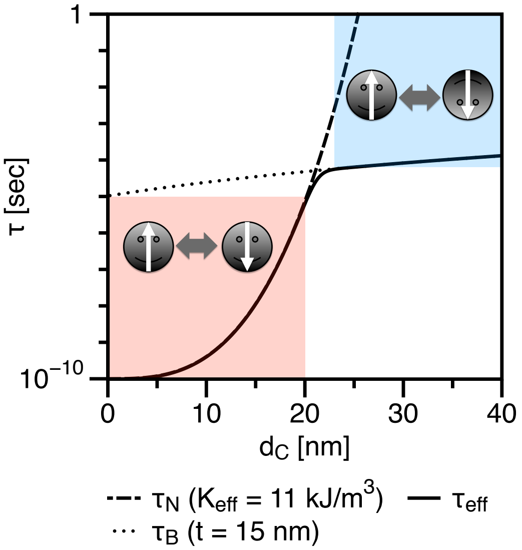

Figure 2-4. Plots for Néel and Brownian relaxation times as a function of nanoparticle diameter. The effective relaxation time τ_{eff} is determined by the shorter of the two time constants. For the Néel plot, $\tau_0 = 10^{-10}$ s and the bulk crystalline anisotropy of magnetite are used. For the Brownian plot, a shell thickness (t) of 15 nm and the viscosity of water ($\eta = 10^{-3}$ Pa.s) are used.

It should be mentioned that the Néel and Brownian relaxation times are relative quantities and must be compared with the measurement frequency for the proper context. For instance, an infinite measurement frequency ($1/t_m = f_m \rightarrow \infty$) relative to the nanoparticle relaxation time will depict the magnetization reversal of single domain particles as hysteretic, which is the assumption made in the Stoner-Wohlfarth model discussed later in §2.3.3. Superparamagnetism is therefore a relative phenomenon that is meaningless without clearly defining a measurement time (t_m); unless explicitly specified, a standard measurement time of 100 seconds is used to define the critical transition from ferromagnetic to superparamagnetic behavior. Thus, using Eq. 2-1 – the relaxation time for a magnetically unblocked particle – we can derive a general condition that meets the requirement of superparamagnetism in a single domain particle:

$$K_{eff}V_c < k_b T ln\left(\frac{t_m}{\tau_0}\right)$$

Eq. 2-6

For the standard 100 seconds measurement time, it is convenient to remember that nanoparticles are superparamagnetic when $K_{eff}V_c < 25k_bT$. Eq. 2-6 can be further rearranged to give the critical superparamagnetic diameter (d_{sp}) for a spherical nanoparticle:

$$d_{sp} = \left[\frac{\ln\left(\frac{t_m}{\tau_0}\right) 6k_bT}{K_{eff}\pi}\right]^{\frac{1}{3}}$$

Eq. 2-7

For comparison, the superparamagnetic transition sizes for magnetite (Fe_3O_4: K_{eff} = 11 kJ/m^3), maghemite (Fe_2O_3: K_{eff} = 6 kJ/m^3) and cobalt ferrite ($CoFe_2O_4$: K_{eff} = 60 kJ/m^3) are shown in Figure 2-5; in general, the transition size is higher for lower anisotropy values. Table 2-1 further illustrates the effect of measurement time ($t_m = 1/2f_{AC}$; where f_{AC} is the frequency of an ac-field)[*] on d_{sp} of magnetite nanoparticles for different anisotropy values; in general, increasing the frequency shifts the superparamagnetic transition size lower. Note that the first order magnetocrystalline anisotropy for bulk magnetite is around 11-13 kJ/m^3 [39], however nanoparticle anisotropy values can range from 23-40 kJ/m^3 for magnetite – higher values are possibly due to the increased contribution from disordered surface spins with decreasing particle size [39-42]. Furthermore, the choice of the three measurement times is intentional; particularly, 20μs and 1.3μs correspond to the measurement times imposed by the ac-fields used in this work for MPI and MFH, respectively.

---

[*] It takes ½ a period of an ac-field to rotate the moment π rad, i.e. parallel to anti-parallel alignment, hence $t_m = 1/2f_{AC}$ and NOT $1/f_{AC}$

So far we have looked at nanoparticle relaxation and the resulting magnetization reversal process in the absence of an external field. However, both MPI and MFH applications require alternating fields with non-zero field amplitudes to drive magnetization reversal. In the following sections, we will consider the effect of such alternating fields on the magnetization reversal process and their implications on MPI and MFH performance.

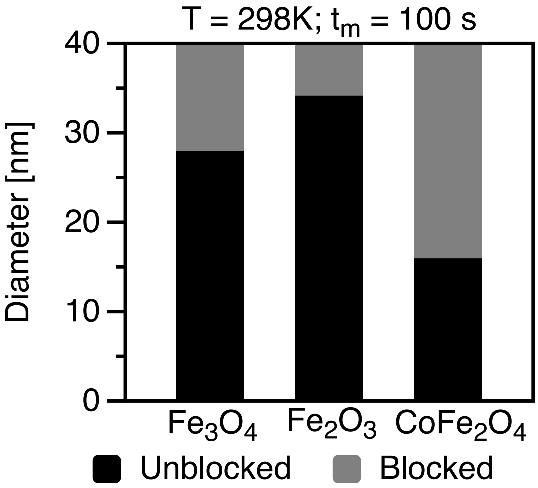

Figure 2-5. The critical transition from magnetically blocked to superparamagnetic (unblocked) behavior as the core diameter decreases at room temperature (298 K) for a measurement time of 100 seconds. The anisotropy energy densities used in the plot are 11 kJ m^{-3}, 6 kJ m^{-3} and 60 kJ m^{-3} for Fe_3O_4, Fe_2O_3 and $CoFe_2O_4$, respectively.

Table 2-1. Range of superparamagnetic transition sizes (d_{sp}) for magnetite at room temperature (T = 298K) as a function of measurement time and various K_{eff} values.

Magnetite (Fe_3O_4) at T = 298 K; $\mu_o H = 0$				
		d_{sp} for various K_{eff}		
t_m [sec]	f_{AC} [Hz]	11 kJ/m^3 (Bulk)	23 kJ/m^3	40 kJ/m^3
1.00E+02	5.00E-03	27.0	21.1	17.6
2.00E-05	2.50E+04	20.6	16.1	13.4
1.33E-06	3.75E+05	18.9	14.8	12.3

2.1.2 The linear response theory (LRT)

The magnetization response of superparamagnetic nanoparticles (Figure 2-2 (b)) to an external field, *M(H)*, is characterized by the Langevin theory of paramagnetism [43]:

$$M(H) = M_s\left[\coth(\xi) - \frac{1}{\xi}\right]$$

Eq. 2-8

where $\xi = \frac{\mu_0 H M_S V_c}{k_b T}$ and M_s is the saturation magnetization value. In Figure 2-6(a), a comparison between simulated (lines) and experimentally measured (symbols) magnetization responses of monodisperse magnetite nanoparticles for various sizes shows excellent agreement with the Langevin function. At very low fields ($\xi < 1$), the magnetization response is linear, and Eq. 2-8 simply reduces to $M(H) = \frac{M_S \xi}{3} = \frac{\mu_0 H M_S^2 V_c}{3 k_b T}$. The slope of the linear response region (*m'(H)*) is called the susceptibility (χ_o), which is expressed as following for spherical nanoparticles with a core diameter d_c:

$$\chi_0 = \left[\frac{dM}{dH}\right]_{H\to 0} = \frac{\mu_0 M_S^2 \pi d_c^3}{18 k_b T}$$

Eq. 2-9

The above expression confirms experimental observations (Figure 2-6(a)) that susceptibility increases with size; critically, the two share a cubic relationship (Figure 2-6(b)). Note that the susceptibility as defined in Eq. 2-9 is a dimensionless quantity called the volume susceptibility. Experimentally, it is more convenient to use the mass susceptibility (units: m^3 kg^{-1}) – obtained by dividing the volume susceptibility by the material density. Mass susceptibility is often used for comparative purposes because the mass/concentration of a sample is accurately measured using elemental analysis methods (e.g. ICP – see §4.2). Note that Eq. 2-9 is not valid for sizes above the critical superparamagnetic size (d_{sp}) because the magnetization response shows hysteresis and no longer adheres to the Langevin model. By convention, d_{sp} is defined for a measurement time of 100 seconds; however, ac-fields used in MPI and MFH impose shorter time windows that shift the superparamagnetic transition to smaller sizes (Table 2-1), adjusting the susceptibility response accordingly (Figure 2-6(b)).

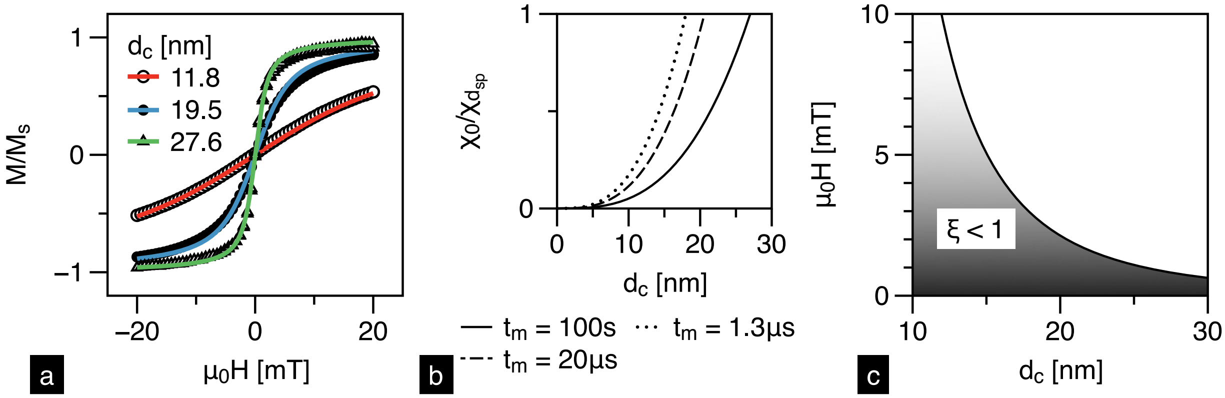

Figure 2-6. (a) Simulated and experimentally measured magnetization responses of monodisperse SPIONs of various sizes shows an increase in susceptibility with size; critically, the two share a cubic relationship. (b) Furthermore, since the superparamagnetic transition size (d_{sp}) depends on the measurement time, the normalized susceptibility (χ_0/χ_{dsp}) adjusts accordingly. Note that the linear response region, and thus the validity of LRT, decreases rapidly with size, as seen in (c).

Furthermore, in low amplitude ac-fields that meet LRT's $\xi < 1$ condition (Figure 2-6(c)), the susceptibility has an in-phase (real) and out-of-phase (imaginary) component. Early experimental measurements of the susceptibility as a function of frequency have shown that the complex susceptibility ($\chi = \chi' - i\chi''$) models after the Debye spectra for polar molecules [44]; thus, the real (χ') and imaginary (χ'') components are expressed as follows:

$$\chi' = \frac{\chi_0}{1 + \left(2\pi f_{AC}\tau_{eff}\right)^2}$$

Eq. 2-10

$$\chi'' = \frac{\chi_0 2\pi f_{AC}\tau_{eff}}{1 + \left(2\pi f_{AC}\tau_{eff}\right)^2}$$

Eq. 2-11

where τ_{eff} [sec], introduced earlier in Eq. 2-5, is the effective relaxation time of superparamagnetic nanoparticles and f_{AC} [sec^{-1}] is the ac-field frequency. Normalized plots of χ' and χ'' in Figure 2-7(a) show that the out-of-phase component is maximum when $2\pi f_{AC}\tau_{eff} = 1$, and coincides with (½)$\chi'_{max}$. At the peak position of χ'', magnetization is perfectly out-of-phase with the applied field – in other words, it shows maximum hysteresis, and any further increase in f_{AC} reduces χ'' because the magnetization is unable to keep up with the rapidly changing field. The peak in χ'' shifts to higher frequencies (fast relaxation times) as particle size decreases, which is consistent with the calculations in Table 2-1 that suggest a shift to lower sizes when the frequency increases. It should be mentioned that the out-of-phase susceptibility has practical implications, as will be discussed later in §2.3.2 – it is a critical parameter for MFH optimization in low amplitude ac-field conditions and is called the “loss” component due to its role in power losses.

In order to test the validity of the LRT, complex susceptibility measurements of PEG-coated SPIONs were performed in collaboration using the DynoMag AC susceptometer system (IMEGO – Gothenburg, Sweden). The hydrodynamic diameter of the two samples with median core diameters 26 and 23 nm was measured using dynamic light scattering and was approximately 40 nm (volume weighted) [45]. The 26 nm sample, which lies in the Brownian relaxation regime (Figure 2-4), shows a distinct peak at ~1 kHz in Figure 2-7(b), which is characteristic of Brownian relaxation; in contrast, the 20 nm sample, which is near the Néel to Brownian transition in Figure 2-4, shows mixed relaxation behavior – a Brownian peak is observed near 10 kHz and a wide Néel relaxation peak at ~100 kHz (Figure 2-7(c)). Compared to Brownian relaxation, Néel relaxation time is highly sensitive to variations in the core diameter: $\tau_N \sim \exp[d_c^3]$ (Eq. 2-2); consequently, there is a wide distribution of relaxation times for an otherwise modest spread in core diameters. As a result, the χ'' peak in the 20 nm sample is broad even though the size distribution – as indicated by the standard deviation of the lognormal distribution – is less than the 26 nm sample. Our experimental measurements confirm that magnetization reversal in the linear response region ($\xi < 1$) is similar to the Debye model for relaxation of polar molecules [44,46,47].

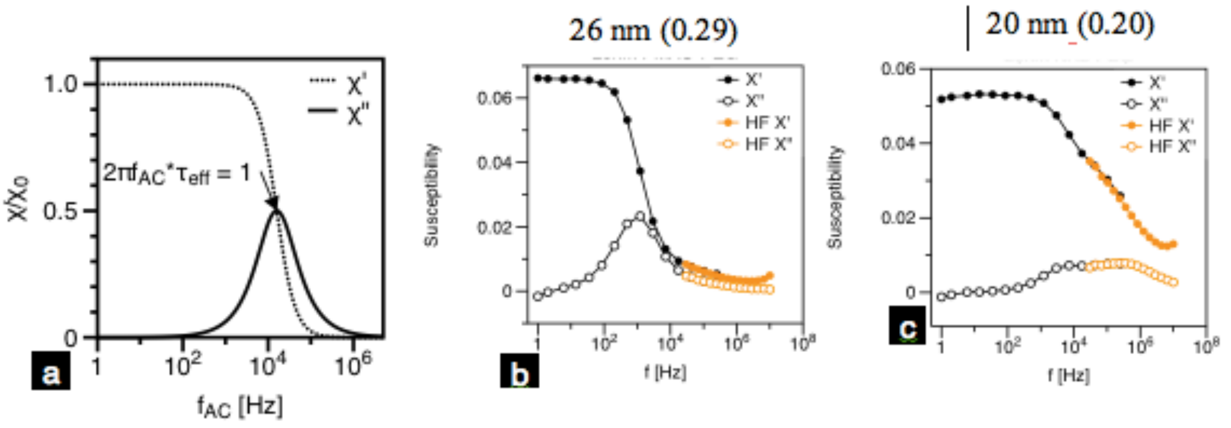

Figure 2-7. (a) Simulated real (χ') and imaginary (χ'') components of the complex ac-susceptibility. The out-of-phase component, which is also called the "loss" component due to its role in power losses (§2.3.2), is maximum when $2\pi f_{AC}\tau_{eff} = 1$. (b) and (c) are experimental susceptibility measurements of 26 nm and 20 nm SPIONs, respectively, taken in IMEGO's Dynomag AC susceptometer (Gothenburg, Sweden). The values in parenthesis are standard deviations assuming a lognormal size distribution. The distinct peak at ~1 kHz in (b) corresponds to Brownian relaxation, while the broad peak at ~100 kHz is characteristic of Néel relaxation. Experimental data shown is stitched from low (black) and high (orange) frequency (HF) systems. Field amplitude was ~0.5 $\mathrm{mT}\mu_0^{-1}$[†].

[†] The magnetic field strength is constant below 1 kHz, but falls off at higher frequencies – Dynomag data sheet: http://www.imego.com/CommonResources/Files/www.imego.com/Documents/DataSheets/AC_Susceptometer.pdf

2.1.3 Field-driven relaxation: the Stoner-Wohlfarth model

So far, we have discussed magnetization reversal mechanisms in zero or very low field amplitude ($\xi < 1$) conditions that ensure the magnetization response is always in the linear response region. We will now use the Stoner-Wohlfarth model [36] to explore the effects of applying higher field amplitudes that begin to excite the nonlinear region of the magnetization response. Consider the single domain particle with uniaxial anisotropy introduced earlier in Figure 2-3(a). When a non-zero field, $\mu_o H$, is applied, it exerts a torque of magnitude $\mu_o M_s V_c H \sin(\phi - \theta)$ on the magnetic moment m (= $M_s V_c$). The energy expended by the field to rotate the magnetic moment is called the Zeeman energy and is expressed as:

$$E_z = \int \mu_o M_s V_c H \sin(\phi - \theta)\, d\theta = -\mu_0 M_s V_c H \cos(\phi - \theta) + C$$

Eq. 2-12

On the other hand, the competing anisotropy energy (E_A) forces the magnetic moment to align in the easy axis direction, which is expressed as $K_{eff} V_c \sin^2(\theta)$ for the first order uniaxial case [31]. A critical assumption in the Stoner-Wohlfarth model is that the temperature T = 0 K; hence, thermal fluctuations are neglected and the total energy of the system is simply the sum of the Zeeman and anisotropy energies. For the simple case when the field is aligned with the easy axis (ϕ = 0), the total energy of the system is:

$$E = E_A + E_z = K_{eff} V_c \sin^2(\theta) - \mu_0 M_s V_c H \cos(\theta) + C$$

Eq. 2-13

In order to find the energy minima and maxima, we differentiate Eq. 2-13 with respect to θ and set it equal to zero:

$$\frac{dE}{d\theta} = 0 = 2K_{eff}V_c \sin(\theta)\cos(\theta) + \mu_0 M_s V_c H \sin(\theta)$$

$$\mu_0 H = -\left(\frac{2K_{eff}}{M_s}\right)\cos(\theta)$$

Eq. 2-14

The energy is minimum when the moment is aligned with the easy axis (θ = 0), which also happens to be the field direction for the ϕ = 0 case. Secondly, at θ = π, we find the anisotropy field, $\mu_0 H_K = \frac{2K_{eff}}{M_S}$, which is the coercive field required to overcome the anisotropy energy barrier for the aligned case (ϕ = 0). Unlike the energy minimum, we find that the location of the maximum depends on the field strength: $\theta = \cos^{-1}[-\frac{H}{H_K}]$; as a result, the energy barrier (ΔE) for magnetization reversal, which is the difference between the maximum and minimum energies, also depends on the field strength (Figure 2-8).

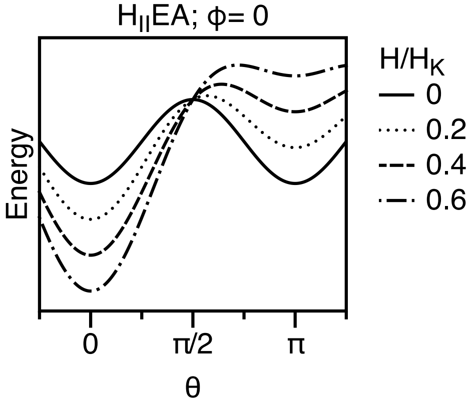

Figure 2-8. The energy barrier for magnetization reversal depends on the field strength. Note the energy maximum is located at $\theta = \pi/2$ – the ‘hard’ axis of magnetization – in the absence of an external field ($H/H_K = 0$).

Mathematically, ΔE is the difference between the maximum, at $\theta = \cos^{-1}\left[-\frac{H}{H_K}\right]$, and the local minimum, at $\theta = \pi$ (for $\phi = 0$). Inserting the corresponding θ values in Eq. 2-13, and replacing M_S with $2K_{eff}/\mu_o H_K$ we get:

$$E_{max} = K_{eff}V_c\left[1+\left(\frac{H}{H_K}\right)^2\right]+C$$

Eq. 2-15

$$E_{min} = K_{eff}V_c\left[\frac{2H}{H_K}\right]+C$$

Eq. 2-16

Thus, the energy barrier, ΔE, for magnetization reversal is:

$$\Delta E = E_{max} - E_{min} = K_{eff}V_c\left(1-\frac{H}{H_K}\right)^2$$

Eq. 2-17

Substituting the energy barrier in Eq. 2-2 with the field-dependent barrier above, we get the expression for Néel relaxation time in the presence of an external field:

$$\tau_{N-field} = \tau_0 \exp\left[\frac{K_{eff}\pi d_c^3\left(1-\frac{H}{H_K}\right)^2}{6k_bT}\right]$$

Eq. 2-18

Thus, by reducing the energy barrier (Figure 2-8), an applied field shortens the Néel relaxation time; consequently, increasing the probability for magnetization reversal. Figure 2-9 shows the effect of field amplitudes used in MFH (17 $\text{mT}\mu_o^{-1}$) and MPI (20 $\text{mT}\mu_o^{-1}$) on the Néel relaxation time. The corresponding measurement times imposed in MPI and MFH are highlighted as well.

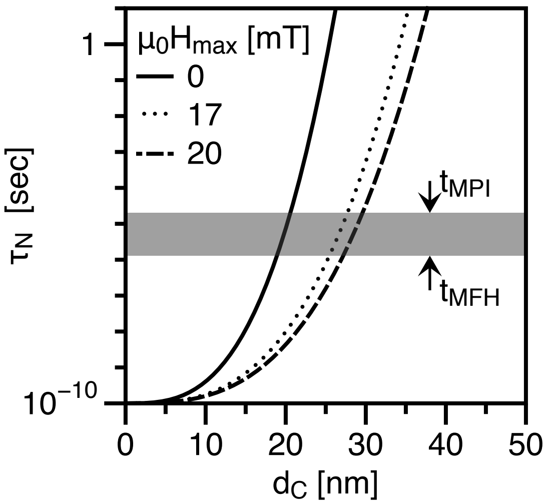

Figure 2-9. Increasing field strength shortens the Néel and Brownian relaxation times. The measurement times – t_{MPI} and t_{MFH} – pertaining to the respective frequencies used in MPI and MFH are shown. For magnetite, K_{Fe3O4} = 11 kJ/m^3 and $M_{s\text{-}bulk}$ = 460 kA/m [30] at T = 298 K).

Now, replacing $\tau_{N\text{-}field}$ with the measurement time t_m and rearranging Eq. 2-18 gives the switching, or the coercive field (H_c) for any combination of measurement time and temperature as a function of the core size d_c:

$$H_c = H_K\left[1-\left(\frac{\ln\left(\frac{t_m}{\tau_0}\right)6k_bT}{K_{eff}\pi d_c^3}\right)^{\frac{1}{2}}\right]$$

Eq. 2-19

Combining Eq. 2-7 with the equation above and normalizing the coercive field with the anisotropy field ($H_c/H_k = h_c$) simplifies Eq. 2-19 to:

$$h_c = \frac{H_c}{H_K} = 1 - \left(\frac{d_{sp}}{d_c}\right)^{\frac{3}{2}}$$

Eq. 2-20

It should be noted that the above equation is only valid for $d_c < d_{sd}$, where d_{sd} is the single domain size limit. Nanoparticles larger than d_{sd} have multiple domains separated by domain walls, resulting in incoherent magnetization reversal due to domain wall motion. Compared to single domain structures, the switching field in multiple domain structures is lower [48]. At the other extreme, nanoparticles below the superparamagnetic limit ($d_c < d_{sp}$) are thermally activated, i.e. $\Delta E < \ln(t_m/\tau_o)k_BT$, and the magnetization with respect to the applied field shows closed loop behavior ($h_c = 0$). Furthermore, Eq. 2-20 is derived under the assumption that the easy axes of all nanoparticles are aligned with the field – an unrealistic situation for non-interacting nanoparticles dispersed in solution; it is possible for nanoparticles to align with applied field if the nanoparticle concentration is high enough to promote dipole-dipole interaction. Consequently, Stoner and Wohlfarth averaged the directional cosines of the various angles the field makes with the magnetic moment to derive the coercive field expression for randomly oriented easy axes with respect to the applied field [36]:

$$h_c = \frac{H_c}{H_k} = 0.48\left[1 - \left(\frac{d_{sp}}{d_c}\right)^{\frac{3}{2}}\right]$$

Eq. 2-21

Figure 2-10 shows a plot of the reduced coercive field for magnetite (K_{bulk} = 11,000 kJ m^{-3}) as a function of core diameter for three measurement times at room temperature, emphasizing its effect on the switching field; critically, reducing the measurement time shifts the superparamagnetic transition size (d_{sp}) lower, which is where the plots intercept the x-axis in Figure 2-10. As mentioned earlier, the theory is only valid for particles below the critical single domain size ($d_c < d_{sp}$) – approximately 83 nm for magnetite [32] (shaded region in Figure 2-10 indicates the multiple domain region). Finally, overlaying the the field amplitudes used in MPI and MFH, labeled as h_{MPI} and h_{MFH}, respectively, provides some practical insight on the magnetization reversal process; critically, SPIONs with diameters below these horizontal lines (20 mTμ$_o^{-1}$ for MPI and 17 mTμ$_o^{-1}$ for MFH) have coercive fields less than the field amplitude, and will undergo field-driven magnetization reversal.

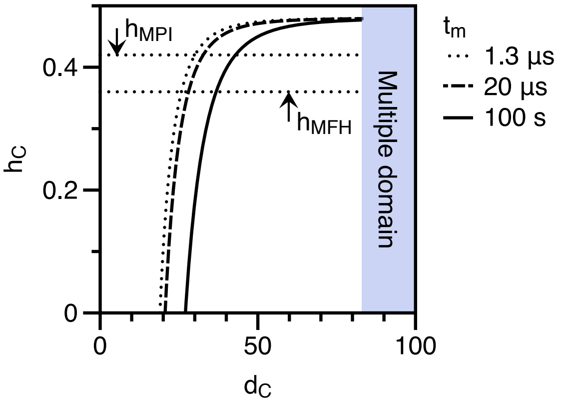

Figure 2-10. The effect of frequency, or the measurement time (t_m) on the coercive field as a function of core diameter (K_{Fe3O4} = 11 kJ/m^3; M_s = 460 kA/m). Reducing measurement time shifts the superparamagnetic transition (closed-open loop) size to smaller diameters.

Finally, the effect of non-zero fields on the Brownian time should also be mentioned. Since analytical solutions of the field-dependent Brownian relaxation time are rather complicated, Yoshida et al performed numerical simulations to derive the following expression for the field-dependent Brownian relaxation time [49]:

$$\tau_{B-field} = \tau_B\sqrt{1 + 0.07\xi^2}$$

Eq. 2-22

where τ_B is given by Eq. 2-4 and $\xi = \frac{\mu_0 M_S V H}{k_b T}$. The above expression suggests that the Brownian relaxation time is shortened when an external field is applied; however, compared to its effect on the shortening of the Néel relaxation time (Eq. 2-18), the external field has a relatively subtle effect on the Brownian relaxation time.

Eq. 2-18 and Eq. 2-22 summarize the Néel and Brownian relaxation times of a single domain nanoparticle in the presence of an applied field. As mentioned earlier in §2.1.1, the shorter of the two relaxation times will determine the predominant reversal mechanism. For the work presented in this thesis, we will see later (§2.2.2) that Brownian relaxation can be neglected because it is often slower than Néel relaxation time, and not the predominant reversal mechanism for the field conditions used in MPI (25 kHz/20 mT$\mu_o^{-1}{}_{max}$) and MFH (375 kHz/17 mT$\mu_o^{-1}{}_{max}$).

2.1.4 Summary of relaxation theory

To summarize the preceding discussion, we will conduct a few thought experiments to illustrate the various conditions for magnetization reversal. Firstly, if the magnetically *unblocked* condition described in Eq. 2-6 is met ($K_{eff}V_c < k_bT * \ln(t_m/\tau_o)$), then the thermal energy will reverse the magnetization inside the particle via Néel relaxation, resulting in a closed loop response to the field (Figure 2-2(b)) that is independent of the solvent viscosity and nanoparticle hydrodynamic size. However, if the magnetization is *blocked* along the easy axis direction for a given measurement time and temperature, then the nanoparticle must physically rotate (Brownian relaxation) in order to align itself with the field direction; thus, the solvent viscosity and hydrodynamic size dictate the energy barrier. In the latter case, unless τ_B from Eq. 2-3 is less than t_m, the magnetization response will show hysteresis (Figure 2-2(a)). In general, the shorter of the two relaxation times determines the reversal mechanism and the effective relaxation time τ_{eff}. Furthermore, the equilibrium magnetization response will be linear and closed loop as long as the field amplitude satisfies $\xi < 1$; however, under non-equilibrium conditions, the susceptibility (χ) varies with measurement frequency. The corresponding magnetization response can show hysteresis, which is maximum when $2\pi f_{AC}\tau_{eff} = 1$. Finally, if the field amplitude is large enough such that the energy barrier for Néel reversal reduces as per Eq. 2-18, and the resulting relaxation time $\tau_N < \tau_B < t_m$, then the magnetization will reverse inside the nanoparticle before it can physically rotate. The switching occurs when the applied field $\mu_0 H > \mu_0 H_c$ and the magnetization response is open loop as illustrated in Figure 2-2(a).

In conclusion, for a given combination of field and temperature conditions, the shortest relaxation time will dictate the primary magnetization reversal mechanism in a *perfectly monodisperse* ensemble of nanoparticles with uniform shell thickness and dispersed in solution. However, real nanoparticle solutions invariably have a distribution of sizes. For small particle solutions, the size distribution is usually described by a lognormal distribution [43]:

$$f(d) = \frac{1}{d\sigma\sqrt{2\pi}} \exp\left(-\frac{\ln\left(\frac{d}{d_0}\right)^2}{2\sigma^2} \right)$$

Eq. 2-23

where d is the range of core diameters, σ is the standard deviation of ln(d) and d_o is the median diameter. Thus in a real dispersion of superparamagnetic nanoparticles, the energy barriers and coercive fields (for $d_c > d_{sp}$) will take a range of values; consequently, a broad size distribution will result in a mixture of Néel, Brownian and field-driven reversal mechanisms, which ultimately deteriorates performance in MPI and MFH.

In the following sections, the working principles of MPI and MFH using the relaxation theory physics introduced in the foregoing sections are discussed. The effects of relaxation on MPI and MFH performance, particularly in physiological environments, are also discussed.

2.2 BASIC PRINCIPLES OF IMAGE GENERATION IN MPI

In a 2-D or 3-D magnetic particle imaging scanner, a time-independent field gradient (~2-8 $\mathrm{T}\mu_o^{-1}\mathrm{m}^{-1}$) is superimposed with a time-varying field (25 kHz and 20 $\mathrm{mT}\mu_o^{-1}$) within the region of interest (ROI). The field-gradient creates a single point of zero-field (Figure 2-11(a)) called the field-free point (FFP), while the time-varying field excites the nonlinear magnetization of SPIONs distributed within the FFP (Figure 2-11(b)). According to Faraday's law of induction, the resulting time-varying magnetic moment, $m(H(t))$ [Am^2], induces a voltage in the receive coil that is proportional to its time derivative, $m'(H(t))$ [$\mathrm{Am}^2\mathrm{s}^{-1}$] (Figure 2-12). The constants of proportionality relating the latter to the measured voltage, $V(t)$, are the coil sensitivity, S [m^{-1}], and permeability of free space, μ_o [$4\pi\times10^{-7}$ $\mathrm{VsA}^{-1}\mathrm{m}^{-1}$]: $V(t) = -\mu_o S m'\big(H(t)\big) = -\mu_o S m'(H) H(t)$. Due to the nonlinearity of the magnetic response, $m'(H(t))$ is a bell-shaped curve as illustrated in Figure 2-12(c); the latter is a parametric plot of $m'(H)$ [m^3] vs $H(t)$ [$\mathrm{Am}^{-1}\mathrm{s}^{-1}$] that depends on SPION size and size distribution – see §2.2.1. On the other hand, SPIONs located outside the FFP experience magnetic saturation and do not show any signal (Figure 2-11(b)). In order to localize the $m'(H(t))$ signal from SPIONs located in the FFP, the FFP is steered in 3D space using a set of orthogonally located drive coils (see [1,50,51] for more details). The $m'(H(t))$ signal from SPIONs is spatially correlated with the FFP's real-time position in the ROI. Secondly, the volume of the FFP determines the instrument's viewing window within which SPIONs are resolved in space. Large field gradients result in small FFP, and thus improve spatial resolution; for instance, a 6 $\mathrm{T}\ \mu_o^{-1}\mathrm{m}^{-1}$ field gradient generates an approximately millimeter scale spheroid FFP [51]. Together, the SPION tracer's response, governed by $m'(H)$, and the MPI scanner's field gradient strength [$\mathrm{T}\ \mu_o^{-1}\mathrm{m}^{-1}$] and FFP velocity [m/s], determine the system Point Spread Function (PSF); critically, the PSF is a property of the tracer *and* hardware. The full width at half maximum (FWHM) of the PSF, in units of distance [mm], is the system spatial resolution and the height is the signal intensity that scales linearly with the amount of SPIONs. Finally, it should be mentioned here that there are currently two primary approaches employed for image reconstruction: the *x-space* approach [52] and the *system* *matrix* approach [53]. In the former technique, image reconstruction is achieved by a convolution of the tracer distribution and PSF, while the latter uses matrix inversion of system function measurements[‡]. Regardless of the reconstruction method, the fundamental working principle of MPI is identical and SPION properties must be tailored to the field conditions used in MPI.

Since commercial MPI scanners were still in early stages of development during the span of this thesis, a home-built magnetic particle spectrometer (MPS) [54] operating at the same ac-field conditions planned for future MPI scanners (25 kHz and 20 mTμ_0^{-1}) was used as the primary tool for evaluating $m'(H)$. An MPS is a 0-dimensional MPI scanner that is used to characterize the raw SPION signal without actually generating an image; thus, it is a precursor to MPI, similar to nuclear magnetic resonance (NMR) is a precursor to magnetic resonance imaging (MRI). In this thesis, MPS was specifically adopted to evaluate *in vitro* performance of SPIONs in simulated physiological environments, and further evaluate their *in vivo* performance and bioavailability (circulation time) in a rodent model.

[‡] The system function measurement maps the particle response to the frequency in the field of view. The data, which is stored in frequency-space and used as a background for the actual image, is later inverted in real-space for image reconstruction.

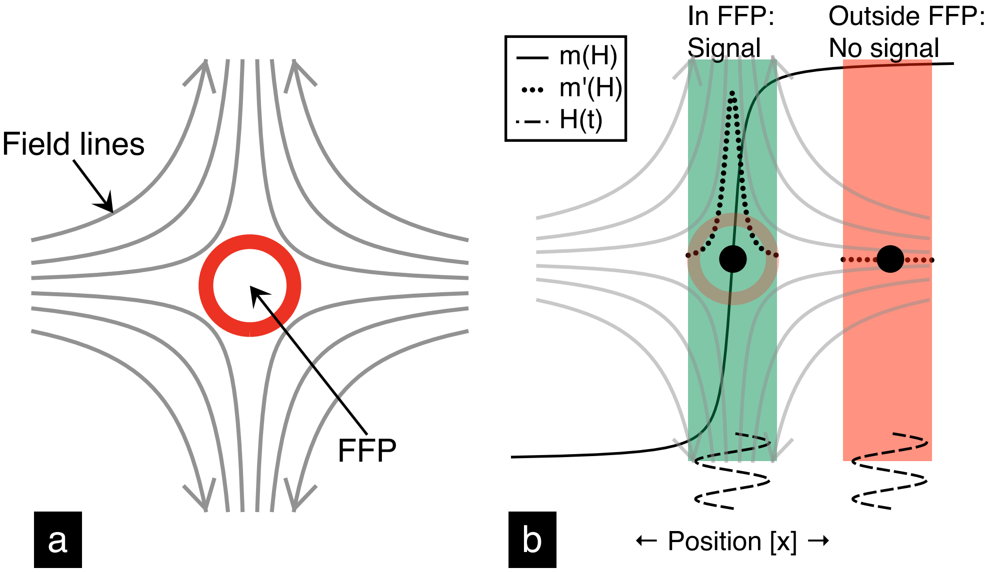

Figure 2-11. The basic principle of signal localization in MPI. (a) A field gradient is used to create a zero-field region called the field free point (FFP) – the volume of the FFP depends on the field gradient strength (~2-8 $T\mu_0^{-1}m^{-1}$) and determines the viewing window within which nanoparticles are detected. (b) The FFP is superimposed with a time-varying field indicated by the sinusoidal wave. SPIONs, shown schematically as black circles, in the FFP exhibit the characteristic non-linear change in magnetic behavior that induces a signal in the receive coil. On the other hand, saturated SPIONs located outside the FFP undergo negligible change in magnetic moment with time. The FFP is steered in space using drive coils to image the distribution of SPIONs in the entire region of interest.

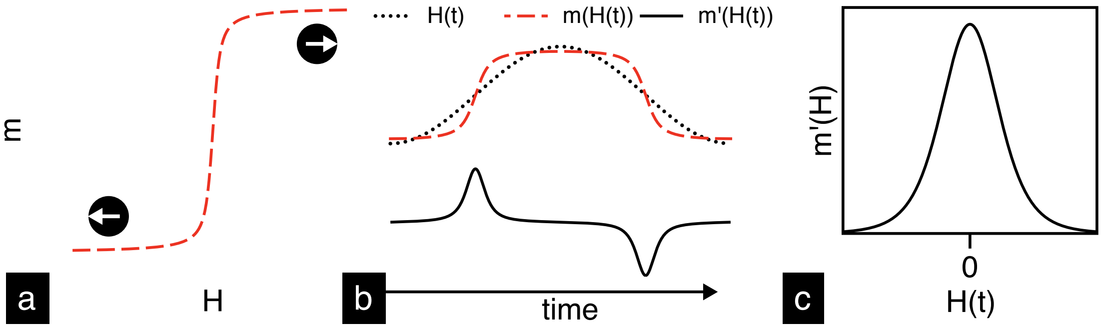

Figure 2-12. The working principle of MPI: (a) the characteristic nonlinear magnetization response of SPIONs is excited in a sinusoidal ac-field. (b) The resulting change in magnetization induces a voltage in the receive coil that is proportional to (c) the rate of change of magnetization with field (*m'(H)*) – a unique property of every SPION formulation.

2.2.1 Optimizing SPIONs for MPI

In order to optimize SPIONs for MPI, the magnetic moment must reach saturation quickly in response to an applied field – in other words, have the maximum possible susceptibility. The cubic relationship (Eq. 2-9) between susceptibility (χ_o) and core diameter (d_c) suggests that bigger particles, relative to smaller particles, have a higher χ_o (Figure 2-6(a)) and thus a narrower and sharper $m'(H)$ curve. However, above the superparamagnetic size ($d_c > d_{sp}$) magnetic reversal is hysteretic (open loop) and further increases in χ_o are negligible [55]; instead, the $m'(H)$ peak position begins to shift towards the coercive field value ($\mu_o H_c$) corresponding to the core size. The evolution of $m'(H)$ as the core size crosses the superparamagnetic size limit is illustrated schematically in Figure 2-13(a-c). Note for $d_c > d_{sp}$, the two $m'(H)$ peaks are from the ascending (solid) and descending (dashed) branches of the hysteresis curve.

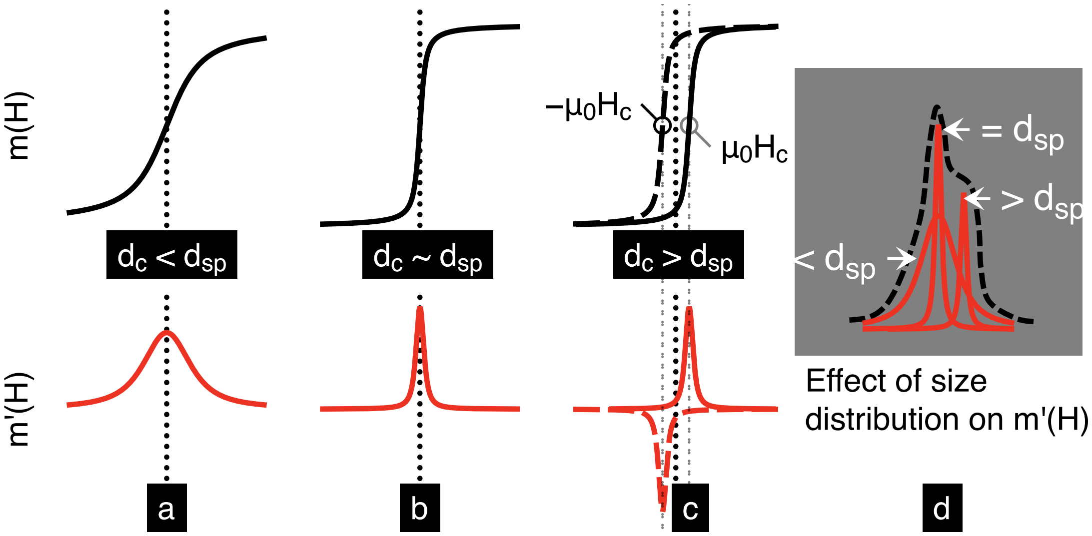

Figure 2-13. Schematic drawing illustrating the effect of core size (d_c) – (a) $d_c < d_{sp}$, (b) $d_c \sim d_{sp}$ and (c) $d_c > d_{sp}$, where d_{sp} is the superparamagnetic transition size – and (d) size distribution on $m'(H)$. In (c), the two $m'(H)$ peaks represent the ascending (solid) and descending (dashed) branches of the hysteresis curve.

From the above discussion it is clear that *m'(H)* for a *perfectly monodisperse* sample is optimal when the core size is equal to d_{sp}. In real samples, however, some size distribution is inevitable; consequently, *m'(H)* represents an effective curve that incorporates a range of nanoparticle sizes as illustrated in Figure 2-13(d). It can be seen that size distribution in general has a deteriorating effect on *m'(H)* and must be as narrow as possible to optimize the effective *m'(H)* response of SPIONs. Moreover, the cubic relationship between susceptibility and diameter suggests that *m'(H)* of nanoparticles below d_{sp} is very sensitive to size distributions. On the contrary, models indicate that susceptibility change is negligible above d_{sp} [55]; only the coercive field changes modestly as a function of core size – $\mu_0 H_c \propto \left[1 - d_c^{-\frac{3}{2}}\right]; d_{sd} > d_c > d_{sp}$ (Eq. 2-21) – as a result, it is beneficial to tailor SPIONs such that their median diameter falls above, rather than below the superparamagnetic transition size. However, increasing SPION size above ~27 nm results in ferromagnetic behavior at room temperature (T = 298 K; Table 2-1), and the permanently magnetized nanoparticles can spontaneously aggregate even in zero field conditions. Thus, in theory *the optimum size for MPI in a 25 kHz field is between 20.6-27 nm*. In practice, however, the optimum size is skewed towards bigger sizes due to size distribution effects.

It should be noted that the optimum size range depends on the effective anisotropy. In the case above, the bulk anisotropy of magnetite (11 kJ/m^3) is assumed, but the anisotropy constant of SPIONs often varies with size [39-41] – the high surface area to volume ratio increases the contribution from disordered surface spins; as a result, the anisotropy typically increases as size decreases.

2.2.2 Nanoparticle aggregation and MPI performance

We will now consider MPI performance of SPIONs within the physiological framework of *in vivo* systems, which is necessary for demonstrating potential clinical applications such as vascular imaging for diagnosing heart diseases and quantitative perfusion-weighted imaging for detecting inflammation sites such as plaques and tumors. In order to realize the several clinical possibilities of MPI, significant innovation and advancement in both imaging hardware and SPION tracers will be necessary. The latter in particular must be tailored such that the signal and FWHM of *m'(H)* are preserved in the *in vivo* environment, which presents a host of physiological and immunological barriers. Foreign entities, such as SPIONs, that stimulate an inflammatory or immunogenic response – either due to poor surface coating or a net surface charge (§3.2 and §3.3) – tend to aggregate due to adsorption of specialized proteins called 'opsonins', and are eventually sequestered by the mononuclear phagocytic system (see Chapter 3). The result of such SPION aggregation is unpredictable, and often adversely affects the critical relaxation processes (Néel and Brownian) that govern the *m'(H)* response of magnetic nanoparticles; as a result, *in vivo* MPI efficacy of SPIONs would be significantly diminished. Appropriately designed surface coatings are central in preventing SPION aggregation and ensuring the preservation of magnetization reversal processes that govern MPI performance. Comprehensive discussion on the role of surface coatings in SPION pharmacokinetics and MPI performance is presented in Chapter 3, while experimental measurements demonstrating the same are presented in Chapter 4, Chapter 5 and Chapter 6; in this section, we will consider the impact of aggregation – an eventuality in physiological systems – on Brownian and Néel relaxation mechanisms.

As mentioned earlier in §2.1.1, Brownian relaxation is the physical rotation of SPIONs to align magnetic moments with the applied field; hence, SPION hydrodynamic volume and the viscosity of the surrounding environment are critical parameters that affect the relaxation time (Eq. 2-3). Physical rotation of SPIONs in the aggregated state, which increases the hydrodynamic volume, or entrapped in high viscosity environments such as the fibrous extra-cellular matrix, may be either partially or completely blocked.

Thus, designing SPIONs that primarily rely on physical rotation (Brownian relaxation) for magnetization reversal may not be an ideal approach to optimization because of the sensitivity to the surrounding environment, which is highly dynamic and often unpredictable in physiological systems. Furthermore, calculations indicate that the Brownian relaxation time of SPIONs in the optimal core size range (~20.6-27 nm) for the field conditions used in MPI (25 kHz and 20 $\mathrm{mT}\mu_o^{-1}{}_{\mathrm{max}}$) and ~15 nm thick outer shell is slow. For instance, using Eq. 2-18 and Eq. 2-22, we find that the Néel and Brownian relaxation times of 25 nm [core dia.] SPIONs with a shell thickness of 15 nm (typical for polymer coated SPIONs in water) are ~0.1 μs and ~23 μs, respectively, in a 25 kHz ac-field with a 20 $\mathrm{mT}\mu_o^{-1}$ field amplitude. Since the Néel relaxation time is significantly slower than the Brownian relaxation time, it is also the predominant magnetization reversal mechanism, and the role of physical rotation can be neglected for the field conditions used in MPI.

On the other hand, aggregation can have an adverse effect on Néel relaxation as well. SPIONs with core diameters in the optimal size range for MPI field conditions (20.6-27 nm) are also above the superparamagnetic transition size; as a result, the magnetization reversal process is governed by the field-driven Néel mechanism (§2.1.3). The formation of aggregated clusters promotes magnetic dipole-dipole interactions that can arrange SPIONs in either linear chains or loop structures to minimize stray fields [56-58]. Since the clusters form at random and are of non-uniform sizes and shapes, the magnetization reversal process spreads out over a range of field strengths and consequently broadens the effective *m'(H)* plot. In summary, regardless of the magnetization reversal mechanism – Néel vs. Brownian – it is important that nanoparticle aggregation is avoided, or realistically speaking, delayed to preserve MPI performance of SPION tracers in the physiological environment.

2.2.3 Summary of MPI optimization

MPI is an inductive method that exploits the nonlinear magnetization response of SPIONs to generate 3-dimensional images of particle distributions. The rate of change of SPION magnetic moment (*m'(H)*) under the influence of an ac-field is the source of the MPI signal – it induces a voltage in the receive coil, which is then spatially localized by moving the field-free point in the region of interest (§2.2). On the other hand, an MPS is a 0-dimensional MPI scanner that measures the *m'(H)* response of SPIONs in the absence of field gradients, thus providing a first order evaluation of SPION performance independent of MPI scanners. For the field conditions used in MPI (25 kHz and 20 mT$\mu_0^{-1}{}_{\mathrm{max}}$), the optimal size range that promises the best *m'(H)* response, and thus MPI performance, is between 20.6-27 nm (§2.2.1). Finally, colloidal stability of SPIONs in physiological environments is a prerequisite for translating the optimized performance to *in vivo* systems. Consequently, surface coatings that form physical barriers between the iron oxide cores and the surrounding environment play a central role in preventing surface adsorption of blood serum proteins and subsequent nanoparticle aggregation, which can otherwise disrupt magnetization reversal processes (Néel and Brownian) that form the basis for MPI and also alter particle pharmacokinetics (see Chapter 3).

In this work, the core and surface coating properties of SPIONs were tailored to optimize *m'(H)*, that was experimentally characterized using a home-built MPS operating at 25 kHz frequency and 20 mTμ_0^{-1} amplitude. Colloidal stability and MPS performance were characterized in serum-rich culture media to study the ability of surface coatings to preserve both MPI performance and stability in physiological environment. Finally, SPIONs administered in the tail veins of mice were allowed to circulate and blood samples were collected at various time points to characterize the blood half-life of SPIONs using MPS and a Vibrating Sample Magnetometer (VSM), which provided a glimpse into the future clinical potential of MPI-optimized SPIONs.

2.3 MAGNETIC FLUID HYPERTHERMIA

Hyperthermia therapy of cancer is an alternative treatment option that uses focused heating to treat tumor sites. A temperature rise of 3-5°C above the physiological temperature (37°C) has been shown to synergistically improve the potency of conventional radiation and chemotherapy approaches [16]; as a result, such mild heating can be employed as an adjuvant treatment option [27]. On the other hand, prolonged exposure to a temperature greater than 5°C above 37°C can overcome “thermotolerance” of cells – induced by the generation of heat-shock proteins (HSPs) that protect the cells from subsequent heating cycles – and has been demonstrated to cause significant cell death [16]. Even greater temperatures (up to 56°C) can lead to “thermoablation”, which results in significant cell necrosis due to carbonization [18,20]. A major challenge in promoting effective hyperthermia therapy, however, is focusing heat dissipation to the disease site in order to prevent damage to healthy tissue – SPION-induced hyperthermia, or magnetic fluid hyperthermia (MFH), offers the possibility of localizing heat dissipation *if* nanoparticles with optimized heating properties can be targeted and confined to the tumor site.

In MFH, an ac-field performs additional work in reversing the magnetization of SPIONs, which is consequently released in the form of heat to the surrounding environment, raising the temperature proportional to the environment’s heat capacity [JK^{-1}]. The amount of heat dissipated, and thus temperature rise achieved, depends largely on the magnetic response of SPION cores to the chosen ac-field conditions. Furthermore, in order to prevent non-specific inductive heating of tissues (due to eddy currents), the parameters of the ac-field – frequency and amplitude – are restricted; typically, safety dictates that the product of field amplitude and frequency ($H_{max} \cdot f_{AC}$) be less than ~5 x 10^9 $Am^{-1}s^{-1}$ [29]. Furthermore, field conditions are often fixed in a particular device, thus SPION properties must be tuned such that their magnetic response matches the latter and offer the maximum possible heating; in this work, the field conditions chosen are near the safety threshold: 375 kHz and 17 $mT\mu_o^{-1}{}_{max}$. In the following sections we will survey the underlying principles of heat generation in MFH, and highlight the key SPION properties that must be tuned for optimizing heating performance.

2.3.1 Principles of SPION heating in MFH

An external field applies a torque on the magnetization of SPIONs, and consequently, performs a certain amount of work. Thermodynamically, the work performed by the external field in aligning magnetization is expressed as follows [41]:

$$\Delta U = -\mu_0 \oint M dH$$

Eq. 2-24

where ΔU is the change in internal energy density [$\mathrm{Jm^{-3}}$] of the system, and the closed integral indicates that the energy is proportional to the area enclosed by the M vs. H curve. It is immediately clear from the above equation that *a lack of hysteresis will produce no heat*; critically, for a given measurement time ($t_m = 1/f_{AC}$), if $d_c \leq d_{sp}$[§], the magnetization response is closed loop (superparamagnetic) and no heat is generated. The *rate* of energy dissipation is called the volumetric power loss, P [$\mathrm{Wm^{-3}}$], and is simply the product of the internal energy density, ΔU [$\mathrm{Jm^{-3}}$], and the applied field frequency, f_{AC} [$\mathrm{s^{-1}}$]:

$$\Delta U f_{AC} = P = -f_{AC}\mu_0 \oint M dH$$

Eq. 2-25

In practice, it is easier to determine the total mass, rather than the volume, of nanoparticles using mass spectrometry techniques; as a result, the specific loss power

---

[§] The superparamagnetic transition size, d_{sp}, depends on the measurement time and will shift to lower sizes as the ac-field frequency (f_{AC}) increases (see Table 2-1).

(SLP: Wkg^{-1}) is typically used as the metric for characterizing heating capacity of SPIONs. Mathematically SLP is simply the volumetric power in Eq. 2-25 divided by the SPION density: P/ρ_{Fe3O4}, where ρ_{Fe3O4} is the bulk density of magnetite [5,200 kg m^{-3}]. However, experimental determination of SLP is more involved and entails careful measurement of the temperature ramp rate, $\Delta T/\Delta t$ [°C s^{-1}], of the colloidal solution containing a known amount of SPIONs [m_{SPION}] dispersed uniformly in a known amount of solvent [$m_{solvent}$]. The SLP and temperature ramp rate are related by the constant c [J kg^{-1} °C^{-1}], which is the specific heat capacity of the solvent. Using water as the solvent [c_{H2O} = 4,186 J kg^{-1} °C^{-1}], the following expression gives SLP from experimentally measured parameters:

$$SLP = c_{H_2O}\left(\frac{m_{H_2O}}{m_{SPION}}\right)\left(\frac{\Delta T}{\Delta t}\right)$$

Eq. 2-26

Notice that the expression above only gives information regarding the experimental determination of SLP; however, the underlying parameters that influence power loss are highlighted in Eq. 2-25. Power loss depends on the ability of both extrinsic (field frequency and amplitude) and intrinsic (magnetization reversal properties of SPIONs) parameters to induce magnetic hysteresis. Depending on the field amplitude, the magnetization response is either in the linear or nonlinear region. In the former case, the field amplitude is small such that $\xi < 1$, and the LRT – introduced in §2.1.2 – is used to define the evolution of hysteresis loops. However, for cases when $\xi > 1$, the magnetization response is nonlinear; consequently, LRT is no longer valid and Stoner-Wohlfarth model based theories (SWMBT) prove more useful – especially when $\xi >> 1$ – in predicting hysteresis profiles. In the following sections, we will consider the evolution of magnetic hysteresis due to time-varying fields in both LRT and SWMBT domains.

2.3.2 Hysteresis losses: LRT

In MFH, the applied field is typically time-varying of sinusoidal form: $H(t) = H_{max}\cos(\omega t)$, where the angular frequency $\omega = 2\pi f_{AC}$ and H_{max} is the field amplitude. In the linear response domain (ξ < 1), the magnetization response, *M(t)*, is related by the complex susceptibility, χ, which has both in-phase (χ': real) and out-of-phase (χ'': imaginary) components; thus, $M(t) = \chi H(t)$, where $\chi = \chi' - i\chi''$. Substituting the expressions for *H(t)* and χ, and using Euler's formula to expand, we get the following expression for the magnetization response: $M(t) = H_{max}[\chi' \cos(2\pi f_{AC}t) + \chi'' \sin(2\pi f_{AC}t)]$ [41]. Substituting the latter in Eq. 2-25 and solving the integral gives us the volumetric power loss in terms of f_{AC}, H_{max} and the out-of-phase susceptibility χ'':

$$P = \mu_0 \pi \chi'' f_{AC} H_{max}^2$$

Eq. 2-27

From the above equation, we can see that power loss depends on both extrinsic – the applied field (f_{AC} and H_{max}) – and intrinsic – out-of-phase susceptibility (χ'') of SPIONs – parameters, and for a fixed set of field conditions, power loss is maximum when χ'' is maximum. The latter occurs when the field frequency (f_{AC}) matches the nanoparticle effective relaxation time (τ_{eff}) and satisfies the condition $2\pi f_{AC}\tau_{eff} = 1$, where $\tau_{eff}^{-1}(H_{max}) = \tau_N^{-1}(H_{max}) + \tau_B^{-1}$ (§2.1.1). Eq. 2-27 makes physical sense because maximum hysteresis area, and thus energy loss, is achieved when the rate of magnetization reversal ($\omega_R = 1/\tau_{eff}$) lags and is perfectly out-of-phase with the applied field. Secondly, for a given nanoparticle size, there is a peak in χ'' (Figure 2-7) and therefore a peak in power loss as a function of frequency. Figure 2-14(a) illustrates that the inverse – *for a given frequency there is a peak in power loss vs. size* – is also true. It should be emphasized that normalizing the power loss as in Figure 2-14(a) does not remove the field dependence because χ'' is inherently dependent on both frequency and field amplitude. Figure 2-14(a) also shows that reducing the frequency shifts the peak to bigger sizes since magnetization reversal time slows down with size. A concurrent inspection of Eq. 2-9, Eq. 2-11 and Eq. 2-27 further indicates that power loss is directly proportional to nanoparticle volume; thus, small variations in diameter ($V \propto d^3$) can adversely affect power loss, as the model in Figure 2-14(b) illustrates.

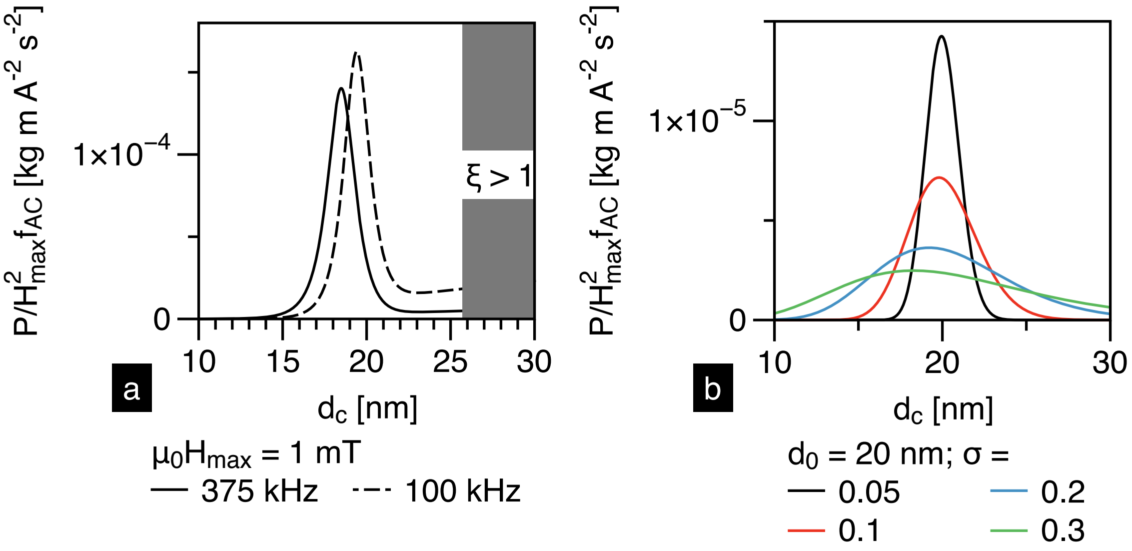

Figure 2-14. (a) Plots constructed from Eq. 2-27 show normalized power loss as a function of core diameter for two frequencies – 375 and 100 kHz – and 1 mT field amplitude; K_{eff} (11 kJ m^{-3}) and M_s (460 kA m^{-1}) values for bulk magnetite are used. Shaded area falls outside LRT's valid domain ($\xi > 1$). (b) Power losses decline significantly with increasing size distribution. The median diameter, d_0, is 20 nm and σ is the standard deviation of ln(d_c). Field conditions: f_{AC} = 375 kHz and $\mu_0 H_{max}$ = 1 mT.

Table 2-2. MFH optimum diameters for various K_{eff} values using Eq. 2-27 in a 375 kHz ac-field. $\mu_0 H_{max}$ = 1 mT; M_s = 460 kA/m (magnetite)

K_{eff} [kJ/m^3]	d_{opt}
11,000	18.5
23,000	14.4
40,000	11.9

Finally, the role of the anisotropy constant on the optimum size is highlighted in Table 2-2. The effective anisotropy of nanoparticles is usually assumed to be a constant, and in the models in Figure 2-14, the bulk value of magnetite (11 kJ m^{-3}) is used. However, it can vary with nanoparticle size, making accurate determination of the optimum diameter using models alone challenging. In general however, a reduction in anisotropy shifts the optimum diameter for MFH to larger particles, which subsequently improves power loss since it is directly proportional to nanoparticle volume.

2.3.2.1 Limitations of LRT

The linear response theory is valid for either very small particles or low amplitude field conditions that fulfill the $\xi < 1$ requirement. Inducing hysteresis and subsequent heating in small particles requires the application of alternating fields in the MHz range, which is often impractical due to the biological safety limits discussed earlier in §2.3. Additionally, low amplitude fields only excite minor hysteresis loops (Figure 2-15), which as the name implies, represent only a fraction of the full or major hysteresis area. In order to generate significant amounts of heat in MFH, bigger particles with large hysteresis area and high amplitude fields that cover the entirety of the hysteresis loop are needed. Since the latter results in nonlinear magnetization behavior, LRT is no longer the valid model for describing power loss. In the following section, we will discuss the evolution of magnetic hysteresis in large alternating fields that excite magnetization beyond the linear response domain.

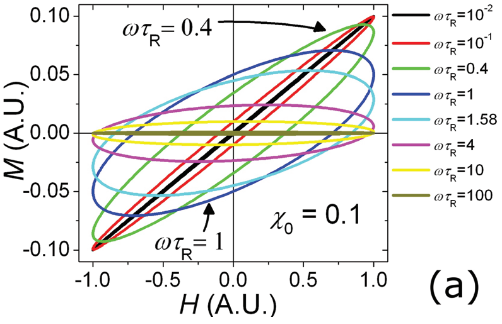

Figure 2-15. Evolution of the hysteresis loop as a function of $\omega\tau_R$ (adopted from [35]), where $\omega = 2\pi f_{AC}$ and τ_R is the nanoparticle relaxation time. Maximum hysteresis area is obtained when $\omega\tau_R = 1$, which is consistent with the peak position in χ'' (Eq. 2-11).

2.3.3 Hysteresis losses: Stoner-Wohlfarth model

As discussed earlier, power losses in MFH are directly proportional to the hysteresis area, and the linear response region only represents a fraction of the entire hysteresis curve. In order to excite major hysteresis loops, the field amplitude must be greater than the coercive field, which is simply the anisotropy field $\mu_o H_K$ for the ideal case when the easy axis of a single domain uniaxial particle is aligned with the field direction (ϕ = 0) – see Figure 2-3(a) in §2.1. Furthermore, since the loop is a perfect rectangle when the easy axis is aligned with the field (Figure 2-16(a)), the enclosed area, A, is simply $4\mu_o H_K M_s$. The product of the area and the field frequency gives the corresponding volumetric power loss:

$$P = Af_{AC} = 4\mu_0 H_K M_s f_{AC}\ (aligned\ case; \phi = 0)$$

Eq. 2-28

Thus, in the aligned case a field amplitude greater than or equal to $\mu_o H_K$ is sufficient to excite the major hysteresis loop. For the more realistic case however, the easy axes of an ensemble of nanoparticles are oriented at random angles with the field direction; consequently, the coercive field is reduced to approximately half the anisotropy field, or $\mu_o H_c \sim 0.48\mu_o H_K$ as shown in Figure 2-16(b).

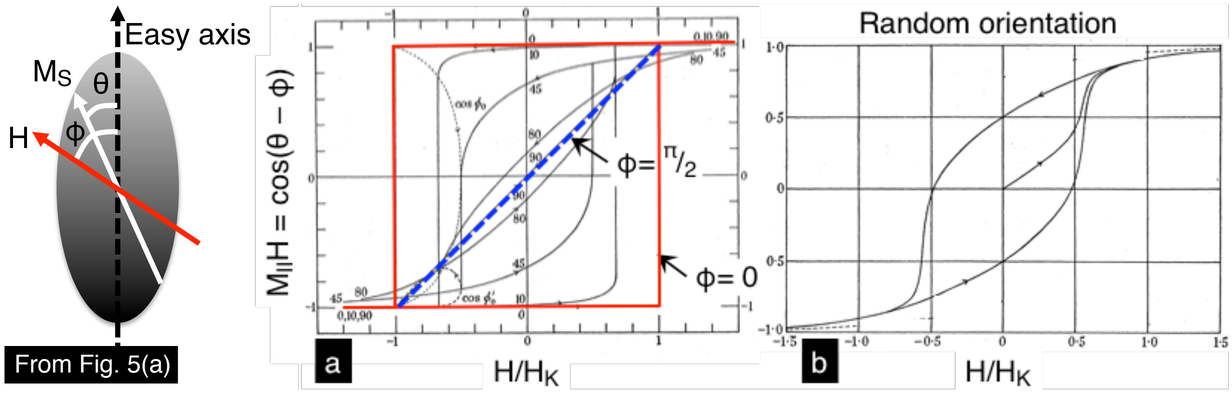

Figure 2-16. Simulated hysteresis loops for uniaxial ferromagnetic nanoparticles at T= 0K – adopted and modified from Stoner et al [36]. For convenience, the single domain uniaxial particle from Figure 2-3(a) is shown. The magnetization component parallel to the field – where θ and ϕ are the same angles labeled in Figure 2-3(a) – is plotted as a function of the reduced field: H/H_K. (a) For the aligned case (ϕ = 0), the hysteresis loop is square shaped and the coercive field coincides with the anisotropy field. In contrast, the magnetization response for the field in the hard axis ($\phi = \pi/2$) shows no hysteresis (dashed line in (a)). (b) Hysteresis profile for a realistic case where the easy axes of an ensemble of nanoparticles are oriented at random w.r.t. the applied field.

Note that the latter is simulated assuming ideal Stoner-Wohlfarth conditions [36], including a temperature of 0K – a condition certainly not true in MFH; nevertheless, the simulation is still a fairly accurate representation and adequate in predicting hysteresis loops of uniaxial ferromagnetic nanoparticles [37]. It is apparent from the shape of the hysteresis loop in Figure 2-16(b) that the field amplitude has to slightly exceed the coercive field in order to take advantage of the entire hysteresis curve; in fact, Carrey et al [35] performed numerical calculations and found that the field amplitude ($\mu_0 Hmax$) has to be ~20% greater than the coercive field to cover full hysteresis. Accordingly, the coercive field for randomly oriented nanoparticles as a function of the applied field is:

$$\mu_0 H_c \approx 0.81 \mu_0 H_{max}$$

Eq. 2-29

The resulting hysteresis area is:

$$A \approx 1.56\mu_0 H_{max} M_s \ (random\ orientation)$$

Eq. 2-30

Combining Eq. 2-29 with Eq. 2-21, and replacing H_K with $2K_{eff}/\mu_o M_s$, we derive the expression below. For a given combination of frequency ($f = 1/2t_m$) and field amplitude ($\mu_o H_{max}$), Eq. 2-31 gives us the optimum diameter for maximum heating in MFH:

$$d_{opt} = \left[\frac{\ln\left(\frac{t_m}{\tau_0}\right) 6k_b T}{K_{eff}\pi\left(1 - \frac{1.69\mu_0 H_{max} M_s}{2K_{eff}}\right)^{\frac{4}{3}}}\right]^{\frac{1}{3}}$$

Eq. 2-31

For the field conditions used in this work, 375 kHz and $\mu_o H_{max}$ = 17 mT, the optimum diameter for magnetite nanoparticles are listed in Table 2-3. Like the earlier discussion in §2.2, the optimum size as per SWMBT also depends on the anisotropy constant.

Table 2-3. Optimum diameters derived from Eq. 2-31 for various values of K_{eff}. f_{AC} = 375 kHz; $\mu_0 H_{max}$ = 17 mT; M_s = 460 kA/m (magnetite)

K_{eff} [J/m³]	d_{opt} [nm]
11000	28.0
23000	16.9
40000	13.1

There are a few differences between the two models used to describe hysteresis losses in MFH. In the LRT, *the hysteresis area peaks when the SPION size, and thus effective relaxation time, matches the applied frequency* ($2\pi f_{AC} {*} \tau_{eff} = 1$). On the other hand, according to the Stoner-Wohlfarth model, hysteresis area peaks when the *field* *amplitude is greater than the coercive field*; in fact, as long as the SPION size falls above the superparamagnetic size for the applied frequency (measurement time), the hysteresis area depends entirely on the field amplitude (Eq. 2-30).

2.3.4 Summary of MFH optimization

Hyperthermia is the use of heat therapy to kill cancer cells directly or indirectly by disrupting the local blood supply. Depending on the temperature rise and exposure time, cancer or other targeted cells experience either thermal ablation (>46°C) or programmed cell death (43-46°C). In MFH, an ac-field is applied to remotely trigger hysteresis losses in SPIONs that result in heat loss. Since SPIONs can be designed to specifically target cancer cells by surface conjugation of targeting moieties with a known binding affinity to receptors unique to or over-expressed on cancer cells [24], MFH offers the promise of focusing hyperthermia therapy only to the disease site and minimize damage to healthy tissue. There is also the prospect of using MFH as an adjuvant therapy approach with traditional chemotherapy or radiation therapy – in this case, even small increases in temperature (37-42°C) significantly enhance the potency of traditional therapies [16].

The thermodynamic basis of MFH is that the alternating field performs *excess work* in reversing magnetization of the SPIONs. The resulting energy loss is proportional to the area of the hysteresis loops; thus, maximizing the hysteresis area is a central goal in optimizing SPIONs for MFH. There are two basic models that help predict the evolution of magnetic hysteresis in SPIONs: (1) The linear response theory (LRT) and (2) the Stoner-Wohlfarth model. Both models are accurate within their respective domains. In the former case, magnetization response is restricted in the linear region ($\xi < 1$) where the susceptibility is a complex function similar to the Debye spectra for polar molecules. The power losses resulting from the elliptical minor hysteresis loops (Figure 2-15) rely on maximizing the out-of-phase susceptibility (χ''), which occurs when the field frequency matches the effective relaxation time ($2\pi f_{AC}{}^{*}\tau_{eff} = 1$) of optimum sized SPIONs. In practice, large amplitude alternating fields are used in MFH, and magnetization response is pushed outside LRT's domain of validity ($\xi > 1$). In the latter case, the Stoner-Wohlfarth model is more useful in predicting the major hysteresis loops. The relation between field amplitude ($\mu_o H_{max}$) and coercive field ($\mu_o H_c$) determines whether the major hysteresis loop is excited; for instance, $\mu_o H_{max} \geq 1.23\mu_o H_c \sim 0.48\mu_o H_K$ to take advantage of the entire hysteresis loop in randomly oriented SPIONs. Both models predict the existence of an optimum diameter for a given set of field conditions; thus, control over nanoparticle size and size distribution is central to improving the MFH performance.

Finally, the anisotropy constant plays a critical role in the determination of the optimum size using either model; however, it varies with size, which makes finding the optimum size difficult using a 'models-only' approach. Due to the fundamental challenge in characterizing the anisotropy constant and its subsequent variance with size, a more direct approach was taken in this thesis. In this work, the optimal diameter for MFH was determined empirically using a dedicated hyperthermia device operating at 375 kHz and $17\text{mT}_{\text{p-p}}$ drive field. Furthermore, the *in vitro* efficacy of MFH was evaluated in cells to demonstrate the translation of MFH as (1) a stand-alone approach, and (2) its role as an adjuvant therapy when couple with conventional options such as chemotherapy.

Chapter 3.

PHYSIOLOGICAL LIMITS: FACTORS AFFECTING SPION PHARMACOKINETICS AND BIODISTRIBUTION

SPIONs designed for *in vivo* use are typically coated with surface coatings that serve as aqueous dispersants and biocompatible layers (non-toxic and non-immunogenic) that impart characteristics necessary for favorable pharmacokinetics (PK) and biodistribution (BD). Pharmacokinetic studies of intravenously administered nanoparticles help determine their circulation kinetics, such as blood half-life, while biodistribution studies provide a preliminary evaluation of their clinical tolerability by observing distribution and accumulation of nanoparticles in various organs after clearance out of the circulatory system. Surface coatings contribute significantly to the hydrodynamic diameter (HD) and the net surface charge – both critical design parameters that determine the *in vivo* fate of nanoparticles. Furthermore, pre-existing physiological barriers, which comprises the mononuclear phagocytic system, and the filtration systems of the kidneys, liver and spleen, impose rules on the design parameters of nanoparticles; thus, knowledge of the physiological limits will aid in designing the first generation of biocompatible SPIONs optimized for MPI and MFH. The following discussion presents an overview of factors that affect nanoparticle PK and BD[**].

The vasculature network is the most commonly employed route for administering nanoparticle formulations, and presents several physiological barriers. It is comprised of blood vessels that are at some regions continuous with limited porosity to allow delivery

---

[**] It should be noted that a significant portion of evidence that defines physiological limits is circumstantial, often originating from experiments that test the PK and BD of plastic microspheres and nanoaparticles of various sizes, shapes and surface coatings. There is also diversity in characterization techniques and animal models in the literature, which adds to inconsistencies in information. Nevertheless, basic physiological clearance mechanisms are well understood, and knowledge of the same highlights nanoparticle parameters that affect PK and BD.

of nutrients (e.g. arteries, heart, muscles, lungs, brain etc.), and in other regions discontinuous and highly fenestrated to allow molecular and macromolecular exchange of materials (e.g. liver, spleen, lymph nodes, etc.). Continuous vessels with pore sizes of ~6-15 nm in the kidneys [8] prevent extravasation of most larger SPIONs, which are ultimately cleared in highly fenestrated filtration organs like the liver and spleen. SPIONs can also passively accumulate in tumor tissues or within small capillaries supplying oxygen and nutrients to these tissues; enveloped in a network of leaky vasculature with poor lymphatic drainage, tumor vessels have fenestrae up to 4 μm in size, which enhances permeability and retention (the "EPR" effect) of nanoparticles [59]. Nevertheless, in a healthy organism, the liver, spleen and kidneys are primarily responsible for nanoparticle clearance. The former two house a significant portion of the cells comprising the mononuclear phagocytic system – a collection of highly phagocytic cells including blood monocytes and other tissue-specific macrophages [60]. Macrophages remove large foreign particles through endo-phagocytic pathways, for instance, SPIONs that are either hydrophobic, aggregating, cationic or tagged with specific proteins called opsonins are quickly recognized and taken up by MPS cells [61]. The resident macrophages in the liver (Kupffer cells) line the interior of fenestrated sinusoidal capillary walls; unlike fenestrated non-sinusoidal capillaries (e.g. kidney glomerulus), sinusoidal capillaries lack a continuous basement membrane and consist of very large fenestrations ranging from 50-180 nm in the liver [8]. Macrophages in the spleen are located in the red pulp, the primary site of splenic filtration, and also the marginal zone between the red and white pulps [62]. The red pulp is part of the "open" circulation route in the spleen, which as the name suggests, lacks direct connections between the arterial and venous capillaries. Blood from the arterial capillary openings flows into the red pulp and re-enters circulation by seeping through the 200-500 nm inter-endothelial slits (IES) in the venous bed [8,63]. The deformability of healthy erythrocytes allows passage through the IES, while dead or rigid erythrocytes accumulate in the red pulp and are eventually cleared by the resident macrophages [63].

With the primary framework of physiological barriers laid out, we can now discuss the effects of SPION hydrodynamic size, surface charge and surface coating on nanoparticle PK and BD, and ultimately designing long-circulating SPIONs. Long-circulating SPIONs are necessary for both MPI and MFH applications. In MPI, SPIONs with long-circulating times that postpone clearance from the vasculature will enable physicians to not only carry out first-pass angiograms (§1.1) – the first targeted clinical application – but also allow for steady-state blood pool imaging. The latter will enable imaging of extremities to diagnose presence of vulnerable plaques or other diseases of the vascular network. Existing blood pool agents like Ablavar®, which is a T1 MRI contrast agent, circulates for up to 1 hour [www.ablavar.com]; however, given the real-time imaging capability of MPI, tracers with shorter circulation times may prove to be sufficient. For cancer diagnosis using MPI and therapy using MFH, long-circulating SPIONs will increase the probability to reach the disease sites – either through passive accumulation of SPIONs in tumors exhibiting leaky vasculature or via active targeting using functionalized SPIONs. Studies indicate that cancer targeting and therapy may require several hours of circulation time to reach the affected sites [64,65] and possibly remain at the site for days if repeated therapeutic exposure and imaging is desired [66].

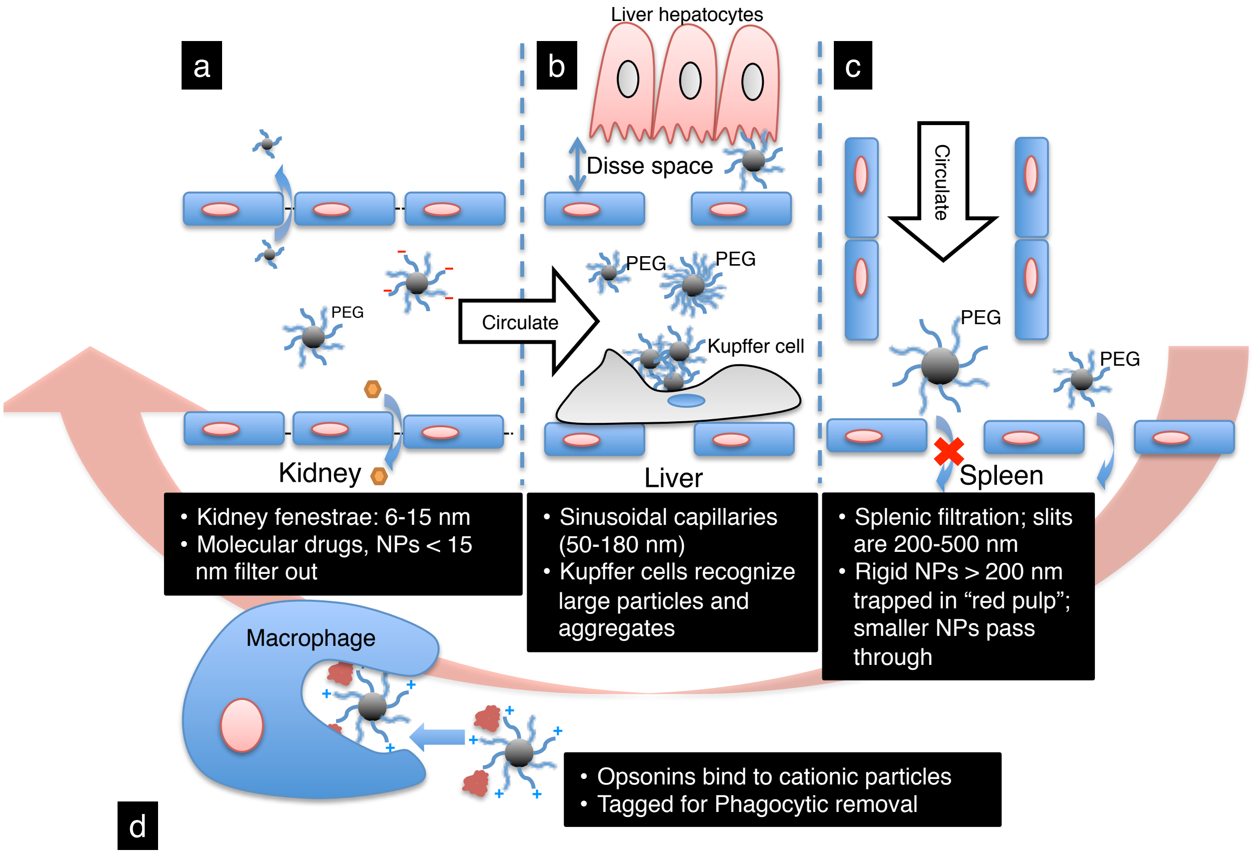

Figure 3-1. Illustration highlighting the key physiological barriers encountered by nanoparticles in circulation. (a) In human kidneys, nanoparticles less than ~15 nm in diameter are filtered out, thus imposing a lower size limit for designing long circulating nanoparticles. (b) Sinusoidal capillaries in the liver are fenestrated (50-180 nm) and lined with the Kupffer cells, which rapidly uptake large nanoparticles or agglomerates tagged with opsonins, and larger nanoparticles are trapped in the disse space. Meanwhile, nanoparticles <100 nm in diameter with non-fouling (prevent protein adsorption) and non-immunogenic (prevent immune response) coatings continue circulating. (c) The Spleen imposes the true upper limit in optimal size for circulation – nanoparticles larger than about 200 nm get trapped in the red pulp, where they are sequestered by the splenic macrophages. (d) Finally, opsonization is the tagging of nanoparticles with specialized proteins called opsonins for removal by phagocytic cells of mononuclear phagocytic system, which includes the Kupffer cells in the liver and the splenic macrophages in the red pulp.

3.1 EFFECT OF SIZE

Nanoparticles with a hydrodynamic diameter (d_h) smaller than kidney fenestrae (6-15 nm) are typically eliminated through renal filtration [61,67]; as a result, long-circulating SPIONs must at the minimum have a d_h larger than kidney fenestrae to avoid rapid renal clearance. Alternatively, SPIONs with d_h larger than the average spacing between inter-endothelial slits in the spleen (200-500 nm) will be retained and eventually cleared by macrophages in the red pulp (Figure 3-1). Thus, strictly based on the lower and upper size limits of physiological barriers, SPIONs with d_h between 15 and 200 nm should have long circulation times. However, PK and BD studies of dextran-coated SPIONs showed that circulation time trends higher with decreasing d_h (unless d_h is smaller than kidney fenestrae, in that case clearance is rapid through renal filtration). For instance, one study reported ferumoxtran-10 (d_h = 30 nm) had a blood half-life of 97-222 minutes, compared to merely 6 minutes for the substantially larger ferumoxides (Feridex I.V. – d_h = 150 nm) [68]; yet another study reported an increase in liver uptake with an increase in d_h – from 33 to 90 nm – of dextran-coated magnetite nanoparticles [69]. In general, *in vivo* cellular uptake increases with hydrodynamic size [70,71], suggesting larger nanoparticles are more susceptible to opsonization – an immune response that adsorbs a class of proteins called opsonins to foreign materials. MPS cells, such as the Kupffer cells in the liver, readily recognize opsonin-labeled nanoparticles for rapid removal through phagocytic processes [72-75]; indeed, Fang et al showed that protein adsorption to nanoparticles coated with the same 5,000 Da PEG, but different hydrodynamic diameters – 80 and 243 nm – increased from 6% to 34%, respectively [64].

3.2 EFFECT OF SURFACE CHARGE

Reducing opsonin binding is critical to designing long-circulation SPIONs, and while numerous factors contribute to protein adsorption on nanoparticle surfaces, surface charge is one of the most significant determinants. Unlike physical characteristics such as size, shape and curvature that only affect the number of bound proteins, surface charge plays a significant role in their identity; positively charged nanoparticles preferentially adsorb negatively charge proteins and vice versa [75]. A survey of the literature shows that nanoparticles with a neutral surface charge have lower opsonization rates than charged particles, and thus retained longer in circulation [61,72,75]. Metz et al [70] showed that carboxy-dextran (negatively charged) coated SHU 555C (d_h ~ 21 nm) showed greater uptake in monocytes than the comparable sized nonionic-dextran coated ferumoxtran-10 (d_h ~ 20-50 nm). In fact, the study suggested that surface charge induced a greater phagocytic effect than size; for instance, carboxy-dextran coated Ferucarbotran (d_h = 62 nm) showed 3x more uptake in monocytes than the significantly larger (d_h = 150 nm) nonionic-dextran coated Endorem. Finally, compared to nanoparticles coated with neutral or nonionic polymers that rely on steric repulsion between polymer chains for stabilization, charged nanoparticles rely on electrostatic repulsion, which is sensitive to changes in pH and can result in particle agglomeration. On the other hand, surface charge may be useful if efficient cell penetration is desired, which is the case for the non-viral delivery of DNA or siRNA to cells using charged polymers [76,77]; typically, positively charged polymers such as poly(ethyleneimine) (PEI) enhance cell penetration due to electrostatic attraction to the negative charge of phospholipids lining the cell membranes.

3.3 EFFECT OF SURFACE COATING

The physicochemical property of surface coatings influences the final hydrodynamic size, surface charge and hydrophobicity of SPION formulations. Hydrophobic surfaces, due to their insolubility in aqueous environments, often undergo rapid non-specific protein adsorption and are unsuitable for designing long-circulating SPIONs. As a result, hydrophilic polymer coatings, such as the polysaccharides (e.g. dextran) and the polyethers (e.g. PEG), which allow sufficient hydration (interaction of water molecules with the polymer shell), are widely used in stabilizing SPIONs; PEG coatings are particularly attractive due to their exceptional non-fouling (resistance to protein adsorption) characteristics [66,78]. Nevertheless, even partially hydrophobic regions, which may not affect solubility in aqueous media, can agglomerate SPIONs in biological media due to opsonization. For instance, hydrophilic polymers are often used to encapsulate and stabilize nanoparticle cores that are either intrinsically hydrophobic or coated with hydrophobic surfactants such as oleic acid, and large exposed regions, due to insufficient polymer coverage, can lead to protein adsorption and subsequent removal by the MPS. Thus, the density or surface coverage of coatings is a critical parameter in designing long-circulating SPIONs. For PEG coated nanoparticles, Storm et al suggest that low or high surface coverage results in either a 'mushroom' or 'brush' configuration, respectively (Figure 3-2) [74]. In the mushroom state, PEG chains are more flexible, and on average lay closer to the surface; critically, the low coverage exposes significant portions of the underlying core to opsonins. At the other extreme, high surface coverage extends PEG chains further into the solvent, but also reduces chain flexibility and mobility – critical features responsible for steric stabilization and non-fouling characteristics [78]. Thus, optimal PEG conformation facilitates both, sufficient cloaking of the underlying core from opsonins, and chain mobility to enhance nanoparticle solubility – a balance between the 'mushroom' and 'brush' configurations.

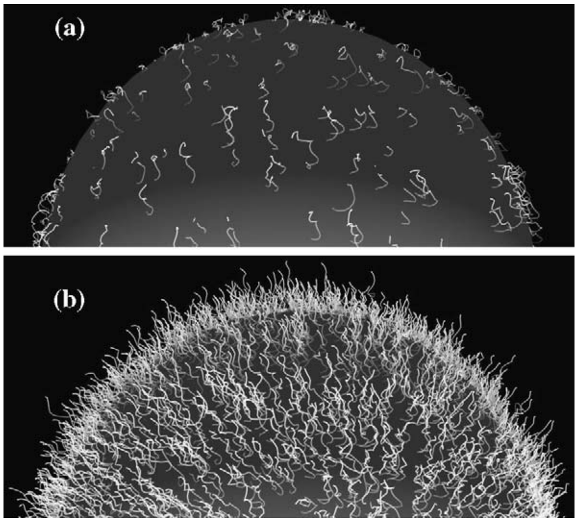

Figure 3-2. Schematic diagrams of PEG configurations on nanoparticle surface as a function of surface coverage (adopted from [72]). (a) In the 'mushroom' state, PEG chains are more mobile, but low surface coverage exposes the core to plasma proteins. (b) In the 'brush' configuration, the dense PEG coverage provides sufficient cloaking from plasma proteins, but minimizes chain mobility and flexibility, which is a critical characteristic that gives PEG its non-fouling characteristics.

3.4 SUMMARY

It is clear from the preceding discussion that the design of SPIONs intended for a specific *in vivo* application is constrained by the pre-existing anatomical and physiological framework. While the magnetic properties of SPION cores largely dictate their MPI and MFH performance, the physicochemical properties of the shell dictate their *in vivo* fate; critically, the pharmacokinetics and biodistribution. With the clinical end-use in perspective, the first generation of SPIONs designed for either *in vivo* MPI or MFH therapy must be biocompatible and demonstrate sufficient circulation times to enable vascular imaging or site-specific heating, respectively. For performing first-pass and subsequent blood pool imaging, a circulation time of approximately 1 hour should provide clinicians sufficient time; for instance, Ablavar® (Lantheus Medical Imaging) – a gadolinium-based MRI blood pool agent remains in circulation for up to 1 hour [www.ablavar.com]. However, given the real-time imaging capability of MPI, even shorter circulation times may be sufficient; ultimately, practical considerations such as the preferred administration route (intravenous injection or cardiac catheterization; the latter is preferred if *in situ* interventional procedures are deemed necessary) and the actual time it takes to ready patients for MPI scans will determine the optimum circulation time of SPIONs. On the other hand, studies indicate that cancer targeting – measured by targeting efficiency and not imaging speed – requires several hours (>1 hour) of circulation time [64,65]; typically, longer the circulation time, greater the probability of reaching the disease site [67].

In order to produce long-circulating SPIONs, the various parameters that affect colloidal stability, opsonization dynamics, PK and BD must be considered. First, the hydrodynamic diameter must be as small as possible, but no less than the size of kidney fenestrae (d_h ~15 nm) to avoid rapid renal clearance. Secondly, a nonionic (neutral surface charge), flexible polymer coating such as PEG that adequately cloaks the surface from opsonins is preferred. Based on these design criteria, and with the goal of designing long-circulating SPIONs, nanoparticles in this work were coated with a polymer containing a nonionic PEG outer shell. Surface density of the PEG outer layer was modified and the resulting *in vitro* phagocytic uptake of SPIONs was evaluated as a function of hydrodynamic diameter and for different surface coatings (§4.2.3). Finally, biodistribution and blood circulation studies were performed in a rodent model (Chapter 6).

Chapter 4.

PHASE TRANSFER OF MONODISPERSE SPIONS: COLLOIDAL STABILITY AND *IN VITRO* CHARACTERISTICS

Monodisperse SPIONs were synthesized via the thermal decomposition of Fe(III)-oleate in organic solvents; details of synthesis are included in Appendix A. Synthesis in organic solvents provides precise control over SPION size and size distribution – critical for optimizing the performance for MPI and MFH. The exceptional size selectivity, and the resulting tailored magnetic properties of the synthesis method are demonstrated in Figure 4-1, which shows the transmission electron microscopy (TEM) images and the normalized static magnetization curves for a range of SPION sizes. TEM size was determined using the free PSAr12 imagej plugin [http://code.google.com/p/psa-macro/], and the resulting histogram was fitted to a lognormal distribution function to obtain the median diameter and standard deviation (σ). The median magnetic core diameter and distribution were also determined by fitting magnetization curves to the Langevin function using the method developed by Chantrell et al [79] – see §B.1 in Appendix B for more details on the Chantrell method. A summary of comparison between the two measurements in Table 4-1 shows that the average discrepancy is <3%. Typically the TEM size is slightly larger than the magnetic size because the presence of disordered spins on the surface usually results in a magnetically 'dead' layer, which is undetected in the magnetic measurements.

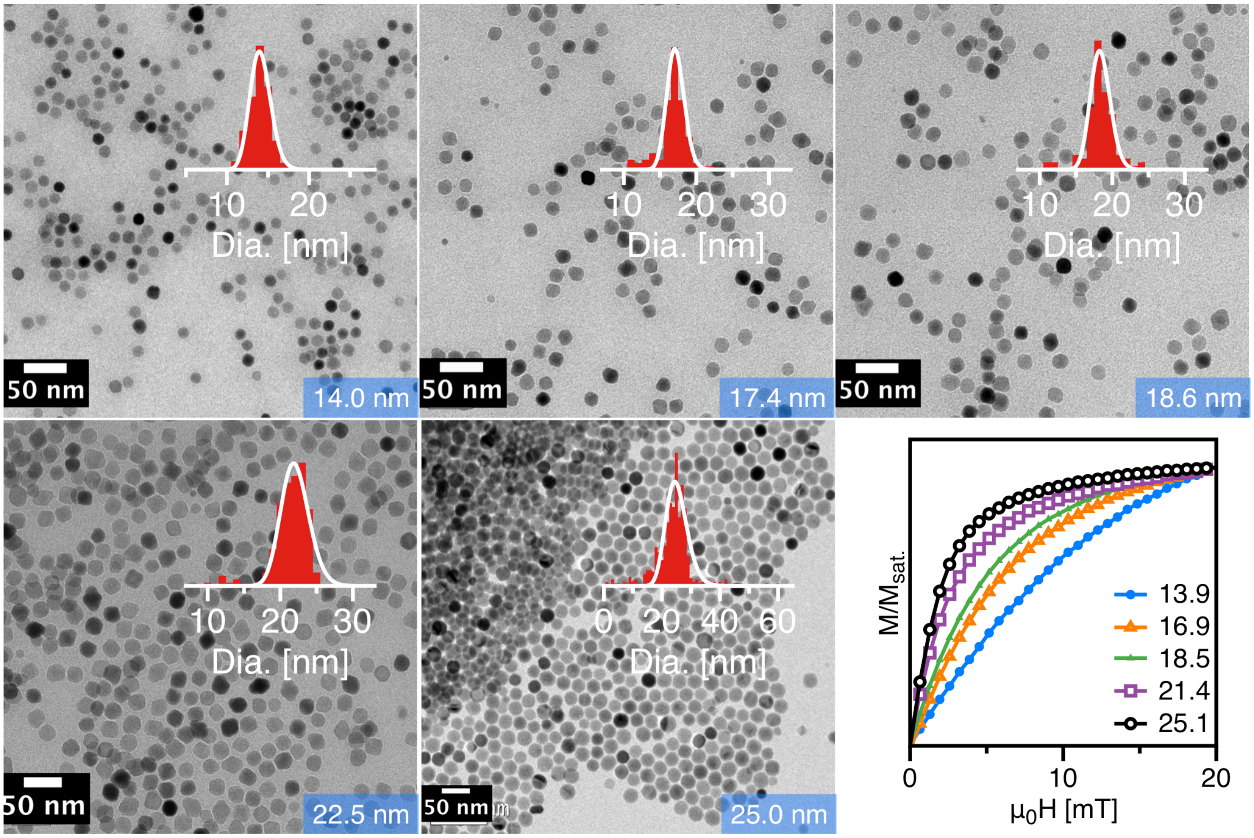

Figure 4-1. TEM images and magnetization curves (bottom right) of various size SPIONs. Insets in the TEM micrographs show histograms constructed using the free PSAr12 plugin in imagej software, which are fit to the lognormal size distribution to obtain the median diameter and the number size distribution. A comparison of size results from TEM and VSM measurements is provided below in Table 4-1.

Table 4-1. Comparison of core size and size distribution measurements obtained using TEM and VSM.

TEM: d_c nm (σ)	VSM: d_c nm (σ)
12.1 (0.24)	11.8 (0.12)
14.3 (0.25)	13.9 (0.11)
17.4 (0.21)	16.9 (0.20)
18.6 (0.22)	18.5 (0.19)
22.5 (0.24)	21.4 (0.25)
24.9 (0.15)	25.1 (0.18)

Powder x-ray diffraction θ-2θ scans (Figure 4-2) suggested that SPIONs have the same crystal structure as the cubic inverse spinel structure of magnetite (Fe_3O_4) and maghemite (γ-Fe_2O_3), but it was difficult to conclude the exact phase – whether magnetite or maghemite – using XRD alone; as a result, electron energy loss spectroscopy (EELS) was also performed in collaboration with the Technische Universität Graz (Graz, Austria). EELS is sensitive to the local ordering and valence of the iron cations in the crystal lattice, which enables differentiation between magnetite and maghemite [80]. Our results confirmed that the SPIONs were magnetite – the EELS spectrum for UW SPIONs (Figure 4-3(a)) showed excellent overlap with the magnetite (Fe_3O_4) reference (Figure 4-2 (c)) and did not show any pre-peaks that were clearly present in the maghemite (γ-Fe_2O_3) spectrum (Figure 4-3(b)).

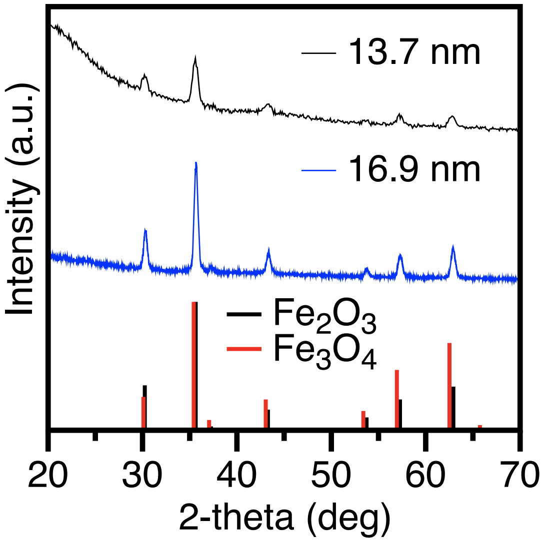

Figure 4-2. Powder X-ray diffraction, θ-2θ scans, of our SPIONs. Sizes indicated in legends were determined by Scherrer's formula[††] using the peak at 2θ=35.4°. Magnetite and maghemite references (bottom) were obtained from the International Centre for Diffraction Data (PDF# 019-0629 and PDF# 039-1346).

[††] $d = \frac{0.9\lambda}{W\cos\theta}$, where d is the crystal size, λ is X-ray wavelength (1.54 Å for Cu-K(α)), W is the peak width (rad) at FWHM and θ is the Bragg angle in consideration.

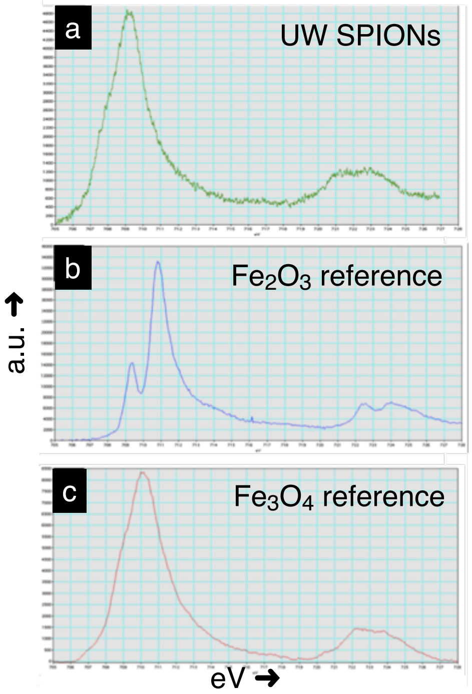

Figure 4-3. Electron energy loss spectroscopy data of (a) UW SPIONs compared with (b) Fe_2O_3 and (c) Fe_3O_4 references. Note that the sample spectrum shows excellent overlap with Fe_3O_4 reference spectrum, with no sign of the additional pre-peak otherwise observed in Fe_2O_3 reference.

Despite the excellent size control of the above synthesis method, SPIONs synthesized using this method are hydrophobic, and thus insoluble in the aqueous phase. In order to render the SPIONs usable in biological systems, they must be transferred to the aqueous phase. The following section discusses the phase transfer of SPIONs from organic to aqueous phase using a PEG-based amphiphilic polymer. SPIONs must be stable in water and serum-rich biological media, and their magnetic properties that govern MPI and MFH performance must be preserved in physiological environments.

4.1 PMAO-PEG POLYMER

In this work, monodisperse SPIONs synthesized in organic solvents were transferred from the organic to aqueous phase using an amphiphilic polymer, poly(maleic anhydride-alt-1-octadecene) (PMAO) that was modified with poly(ethylene glycol) (PEG). The structure of PMAO is shown in Figure 4-4(a); it has an average molecular weight (M_n) of 30,000-50,000 Da and consists of alternating octadecene (hydrophobic) and anhydride (hydrophilic) repeating units. The octadecene chains can form hydrophobic-hydrophobic bonds with the oleic acid coated SPIONs, while the anhydride rings undergo hydrolysis in the aqueous phase, each releasing two carboxylic acid groups. Due to the negative charge of carboxylic acid, the solubility of PMAO-coated nanoparticles is usually enhanced in alkaline conditions that deprotonate the carboxylic group. The robustness of a PMAO coating can be further improved using diamine cross-linkers that form bridges between neighboring chains. For instance, Pellegrino et al used a slight variation of PMAO, poly(maleic anhydride-alt-1-tetradecene), to solubilize hydrophobic nanocrystals in water using bis(6-aminohexyl)amine – a diamine cross-linker [81].

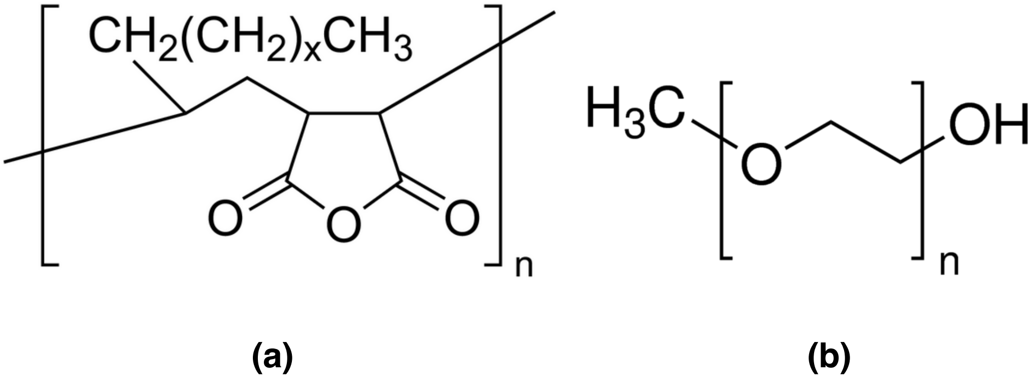

Figure 4-4. (a) Chemical structures of poly(maleic anhydride-alt-1-octadecene) (PMAO) and (b) poly(ethylene glycol) capped with a methyl ether group.

Alternatively, the solubility and biocompatibility of PMAO-coated nanoparticles can be improved through ‘PEGylation’, which is the process of attaching PEG [82,83]. PEG is an FDA approved biocompatible polyether compound that comes with a variety of end groups – the structure of a PEG molecule with a methyl ether with two hydroxyl end groups (Figure 4-4(b)) that has been widely used to improve the pharmacokinetic properties of several pharmaceutical carriers [84]. Some of its non-fouling properties discussed in §3.3 are critical in reducing the immunogenicity of PEG-coated nanoparticles. It is commercially available in a wide range of molecular weights (500 Da to 30,000 Da) and functional groups – both play a critical role in the non-fouling and surface charge properties of the polymer. PEGylation of PMAO is achieved by forming an ester-linkage between one of the PEG hydroxyl end-groups and a carboxylic acid group in PMAO. In order to prevent cross-linking, a monofunctional PEG with a free hydroxyl group on one end and an inert methoxy group at the other end was used in this work (methoxy-PEG). The reaction scheme for the proposed chemistry is shown in Figure 4-5; under acid catalysis, the hydroxyl end group reacts with the anhydride to achieve PEGylation via the formation of an ester bond. Furthermore, based on the molecular weight of PMAO (~40,000 Da), it has approximately 114 anhydride rings, which offers the possibility of varying the PEGylation density by simply adjusting the PEG/PMAO molar ratio.

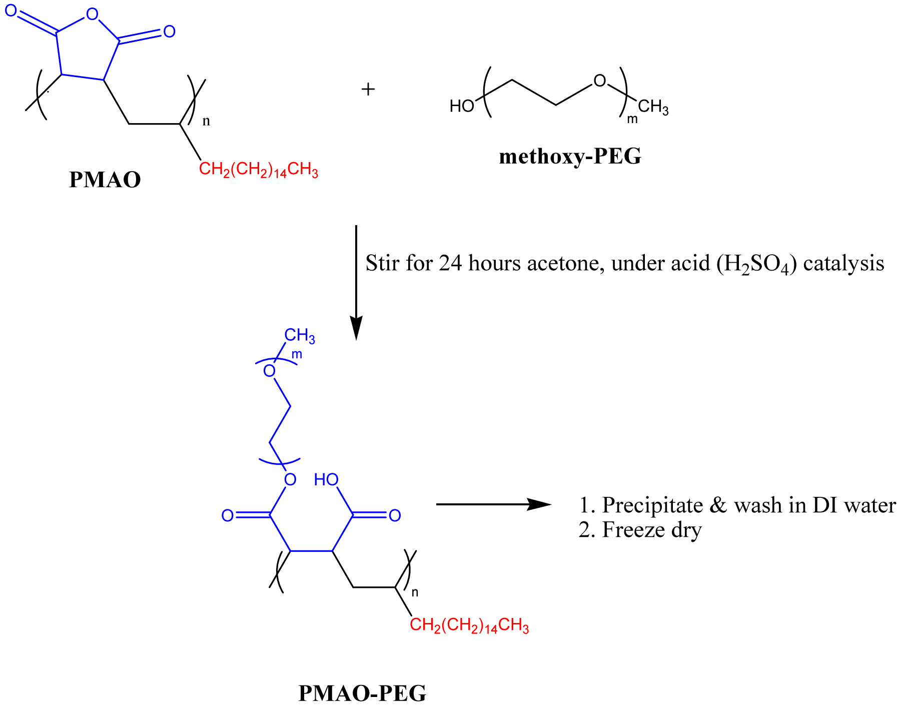

Figure 4-5. Reaction scheme showing the grafting of methox-PEG to PMAO.

The molecular weight of PEG is an important parameter that dictates the final hydrodynamic size and the surface adsorption of proteins, which are critical determinants in the *in vivo* fate of nanoparticles (Chapter 3). Gref et al studied the plasma protein adsorption rate and phagocytic uptake of polymeric nanoparticles coated with PEG chains ranging from 2,000-20,000 Da and found that 5,000 Da PEG demonstrated maximum reduction in protein adsorption [85], while Maldiney et al showed that increasing the molecular weight of PEG from 5,000 to 20,000 Da had only 'negligible influence' on the *in vivo* biodistribution of silicate-based nanoparticles [86]. In an *in vitro* cytotoxicity study, Häfeli et al concluded that magnetite nanoparticles coated with triblock polymers containing PEG lengths above 2,000 Da are biocompatible and appropriate for *in vivo* application [87]. Finally, literature reviews [66,84] on PEG coatings for nanoparticles and drug delivery show that lower molecular weight PEGs, ranging from 1,000-5,000 Da, are preferred for large nanoparticle systems (50-100 nm) and further increase might deteriorate pharmacokinetics due to the increase in hydrodynamic size.

In this study, a 5,000 Da methoxy-PEG was used for all *in vivo* experiments. Furthermore, colloidal stability and *m'(H)* (MPI performance) in serum-rich cell culture medium, macrophage uptake, and *in vivo* biodistribution of SPIONs coated with two surface densities PEG/PMAO ratios of 20 and 30. Finally, more recent measurements of SPIONs coated with a 20,000 Da PEGylated PMAO are also shown, and demonstrate excellent colloidal stability and sustained MPS signal in serum-rich environments. In the following section, the general experimental procedure used for synthesizing PMAO-PEG polymers, and their characterization using Gel Permeation Chromatography (GPC) is presented.

4.1.1 Synthesis of PMAO-PEG

In this work, methoxy-poly(ethylene glycol) of various molecular weights (m-PEG, M_n = 750/2,000/5,000/20,000 Da; Sigma Aldrich) were used to PEGylate PMAO[‡‡] (Sigma Aldrich). Under acid catalysis, the hydroxyl group on m-PEG forms an ester bond with the anhydride ring on PMAO [82,83]. In a typical reaction for the synthesis of PMAO-PEG(5000) with a PEG/PMAO = 20, 2 g of PMAO (≈ 50 μmol) was reacted with 5 g (for m-PEG(5000)) of m-PEG (≈ 1000 μmol) in 20 ml of acetone; 100 μl of concentrated sulfuric acid was added as a catalyst. For higher density PMAO-PEG, only the amount of m-PEG was changed, keeping PMAO amount constant at 2 g. The mixture was refluxed at 58°C in an argon atmosphere. After 24 hours, the mixture was cooled to room temperature and the polymer was obtained by precipitation in excess DI water. After several more DI water washes by sonication and centrifugation, the white polymer cake was freeze dried for 24 hours. The final product was obtained as a white powder and stored at room temperature. Gel Permeation Chromatography (GPC) data in Figure 4-6 compares the elution spectra of PMAO-PEG(5000) and PMAO-PEG(750) – both have a PEG/PMAO = 20 – with PMAO-only control. In GPC the highest molecular weight materials come out first, thus the shift in the peak positions (arrows) to earlier times with PEG conjugation confirms successful conjugation. Furthermore, consistent with their expected molecular weights, the PMAO-PEG(5000) elutes out before PMAO-PEG(750).

[‡‡] Note that the PMAO-PEG polymer synthesized using the 20,000 Da PEG is a recent development; as a result, only preliminary evaluation, such as colloidal stability (§4.2.2) and MPS results (§5.1.2) are presented for SPIONs coated with this polymer. Future work will entail *in vivo* pharmacokinetics and biodistribution studies similar to those in Chapter 6.

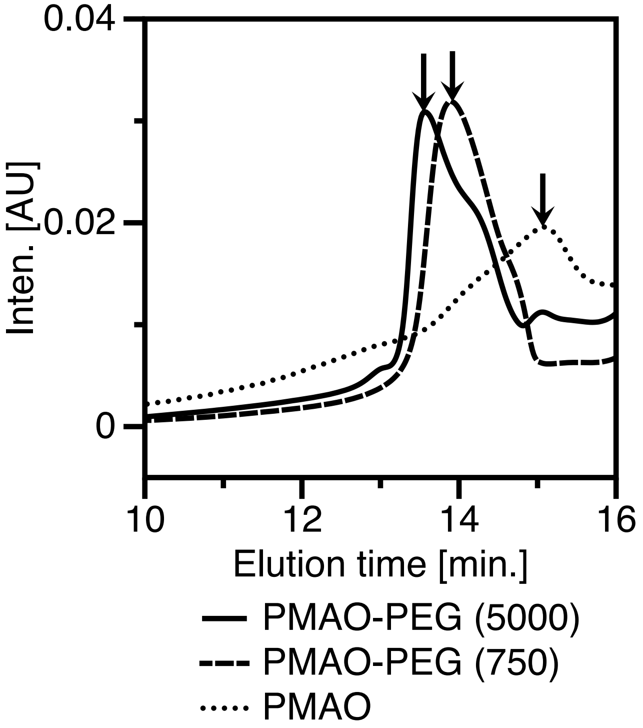

Figure 4-6. GPC data shows an increase in molecular weight with PEGylation of PMAO, suggesting successful conjugation. As expected, PMAO conjugated with higher molecular weight PEG (5000 Da) elutes before lower molecular weight (750 Da). The molar ratio of PEG/PMAO is 20 for both high and low molecular weight PEGs.

4.2 PHASE TRANSFER OF HYDROPHOBIC SPIONS USING PMAO-PEG

In a typical phase transfer process (Figure 4-7), about 10 mg of oleic acid coated SPIONs (SPION@OA) and 10 mg of PMAO-PEG were dissolved in 1–2 mL of chloroform. The mixture was sonicated in an ultrasonic bath for about 15 min and dried under a stream of argon. The dried nanoparticle-polymer complex was dispersed in 1 mL of 1x Tris-acetate-EDTA (TAE) buffer by a 30-min sonication step. SPION coated PMAO-PEG (SPION@PMAO-PEG) were filtered using a 0.2-µm nylon syringe filter. To remove excess unbound polymer, SPION@PMAO-PEG were passed through a Sephacryl™ S-200 HR gel column (GE Healthcare Life Sciences). Either deionized (DI) water or 1x phosphate buffered saline (PBS) was used as the eluent. Nanoparticles were stored at 4^{o}C until further use. Iron concentration was determined using an Inductively Coupled Plasma-Omission Emission Spectrophotometer (ICP-OES, Perkin Elmer). The core size of SPIONs was determined from TEM and VSM measurements. In the latter method, magnetization curves were fit to the Langevin function using the Chantrell method to determine the median core diameter and the standard deviation assuming a lognormal distribution of sizes [43].

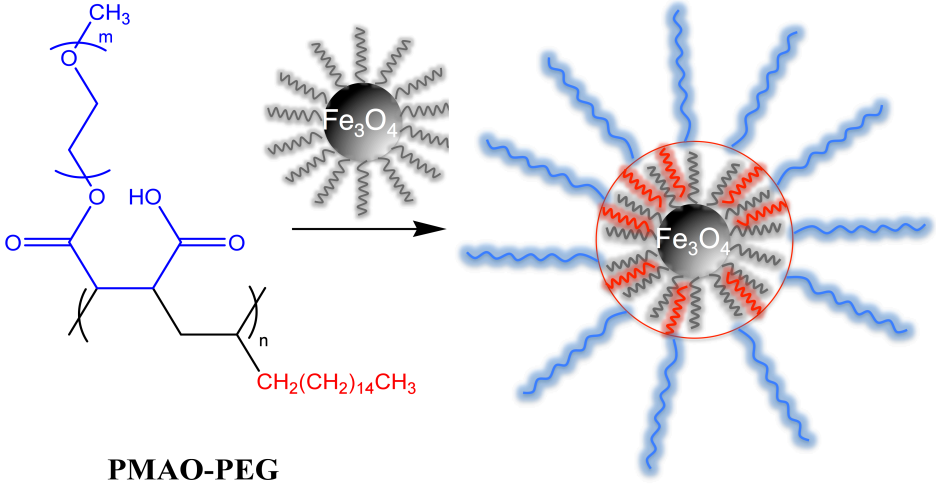

PMAO-PEG

Figure 4-7. Schematic depiction of the PMAO-PEG coating on oleic acid coated SPIONs. The hydrophobic octadecene chains (red) in PMAO interact with the surface oleic acid (black) through hydrophobic-hydrophobic interactions. The hydrophilic PEG chains (blue) extend outwards in the aqueous phase, providing the necessary solubility.

4.2.1 Surface properties of PMAO-PEG coated SPIONs

The colloidal stability of SPIONs transferred in the aqueous phase was evaluated using Dynamic Light Scattering (DLS; Malvern), which measures the hydrodynamic diameter of nanoparticles dispersed in liquids. DLS size data is typically presented as intensity, number and volume distribution. In order to understand the differences between the three distributions, consider a colloidal dispersion of spherical nanoparticles containing equal numbers of particles at 2 sizes, say 5 nm and 50 nm. The number distribution will show two peaks of the same height at 5 nm and 50 nm. The volume distribution, since it scales as cube to the diameter, will show a peak at 50 nm that is 1000x the height of the peak at 5 nm. Finally the intensity distribution will show a peak at 50 nm that is 1,000,000x the peak at 5 nm, because the intensity, from Rayleigh's approximation, scales to the sixth power of diameter. For a perfectly monodisperse size distribution, peaks from the intensity, volume and number distribution line up. However, small variations in size that show up only minutely in the tails of the intensity distribution are magnified in the volume and number distributions; in general, the number and volume distributions give more information on the various size fractions present in a polydisperse sample. In order to get a more complete picture of the evolution of SPION hydrodynamic size, all three distributions will be studied. Furthermore, zeta potential measurements as a function of pH were done to determine the net surface charge of SPIONs. Unlike hydrodynamic size, zeta potential provides information on the physical basis of colloidal dispersion, i.e. electrostatic versus steric repulsion.

Depending on the core size of SPIONs, the ratio between PEG and PMAO and PEG molecular weight (chain-length), the mean hydrodynamic diameter of PMAO-PEG coated SPIONs was found to range from 40-60 nm in DI water. Variability in phase transfer from batch to batch also plays a significant role in the final hydrodynamic diameter as indicated in Table 4-2, which shows that smaller core size did not always correlate with a smaller hydrodynamic diameter. It is also possible that smaller SPIONs get coated in clusters, which may explain their relatively larger hydrodynamic diameters. Variability in phase transfers can potentially be minimized in more controlled or automated processes. Finally, zeta potential measurements showed a nearly neutral surface potential as a function of the solvent pH, suggesting the SPIONs are stabilized primarily via steric repulsion (Figure 4-8).

Table 4-2. Hydrodynamic diameters of various SPION cores coated with PMAO-PEG(5000) in DI water; PEG/PMAO = 20 for all samples.

VSM-d_c (σ)	DLS-d_h (PDI)
11.8 (0.12)	61.9 (0.15)
13.9 (0.11)	47.1 (0.13)
16.9 (0.20)	61.2 (0.15)
18.5 (0.19)	51.1 (0.14)
21.4 (0.25)	54.8 (0.15)

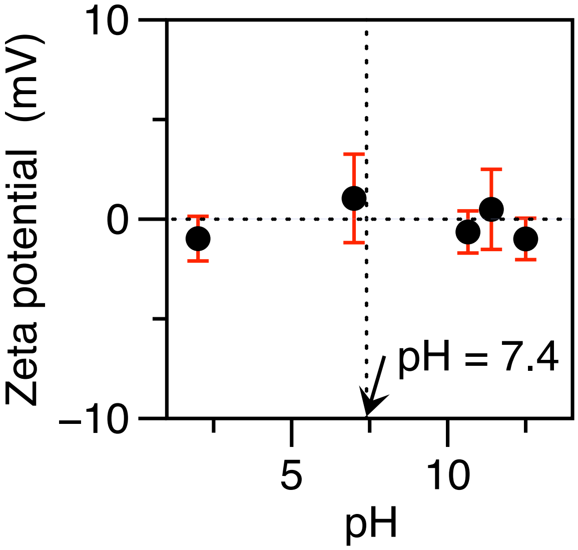

Figure 4-8. Zeta potential measurements of SPIONs coated with PMAO-PEG(5000) and a PEG/PMAO = 20. The surface charge is neutral across a range of pH values, suggesting stabilization via steric repulsion of PEG chains.

4.2.2 Colloidal stability in physiological environments

In Figure 4-9, the hydrodynamic size evolution of SPIONs in RPMI cell culture medium, containing 10% fetal bovine serum (FBS), is shown. The core diameter of the SPIONs was greater than 20 nm; for more information on core diameter see the title column. SPIONs were coated with either one of the two PMAO-PEG(5000) polymers – PEG/PMAO = (a) 20 or (b) 30 – or (c) PMAO-PEG(20,000) with a PEG/PMAO = 30. For reference, DLS size data of RPMI+10%FBS (dashed curve) was collected for each sample as a background reference. The mean hydrodynamic diameters (d_h) of all three samples in DI water are summarized in Table 4-3 below.

Table 4-3. Hydrodynamic size data of SPIONs in DI water; for more information on core diameter, see Figure 4-9. SPIONs were coated with either PMAO-PEG(5000) or PMAO-PEG(20,000). The hydrodynamic size increases with PEG chain length, but remains nearly constant when the density (PEG/PMAO) increases from 20 to 30.

PEG – M_n [Da]	PEG/PMAO	DLS: d_h nm (PDI)
5,000	20	44.1 (0.13)
5,000	30	46.1 (0.13)
20,000	30	62.1 (0.06)

The hydrodynamic diameters of SPIONs coated with the same chain-length PEGylated PMAO (5,000 Da PEG), but different PEG density coatings are quite similar. On the other hand, SPIONs coated with similar PEG density, but different chain lengths show more significant differences in hydrodynamic size; typically, a longer chain length resulted in a larger hydrodynamic size for the same core size particles. Colloidal stability measurements in cell culture medium, shown in Figure 4-9, provide a more complete and relevant evaluation of the surface coatings. The intensity distribution in both shorter chain-length PEG-coated SPIONs suggests that the hydrodynamic size increases dramatically immediately after dispersion in RPMI+10%FBS; however, closer inspection shows that the new peaks at larger sizes coincide with the background spectrum of the media. Since sample preparation process for DLS measurements requires diluting SPIONs by a factor of almost 100 (v/v), the size peaks attributed to SPIONs are indistinguishable due to their relatively dilute concentration compared to the various proteins present in RPMI+10%FBS cell culture medium. As a result, we turn our attention to the volume and number distribution plots, which provide more discernable information about the evolution of hydrodynamic size with time. Let us first consider the size evolution of SPIONs coated with the lower PEG-density polymer (Figure 4-9(a)). Immediately after dispersing in RPMI [t = 0h], both the volume and number distributions show a decrease in the peak positioned at around 10 nm, which corresponds to the proteins present in RPMI, and new peaks appear at larger sizes. Critically, the new peaks are located at several hundreds of nm and do not coincide with the original DI water DLS size spectrum (solid lines). The latter observation suggests the potential formation of nanoparticle agglomerates. The decrease in the 10 nm protein peak reflects reduction in the number of free proteins, potentially due to their role in adsorbing to the SPION surface. At the 0.5-hour time-point, the 10 nm peak corresponding to the free proteins shifts towards larger size in both volume and number distribution plots, suggesting a large fraction of the free proteins are actively adsorbed to the nanoparticles. Furthermore, the number distribution indicates a bimodal distribution of nanoparticles. Finally, 1 hour after dispersion in RPMI+10%FBS, the volume distribution shows an additional peak between 5,000-10,000 nm, indicating very large agglomerates, while both distributions show nearly no peak corresponding to the free proteins at 10 nm.

Next we consider the size evolution of SPIONs coated with the 5,000 Da PEG and a PEG/PMAO of 30 (Figure 4-9(b)), which is 1.5-fold greater than the polymer discussed above. Immediately after dispersion in RPMI [t = 0h], the volume and number distribution curves, similar to the intensity distribution curve, only show peaks corresponding to the free proteins; no peaks from the highly diluted SPIONs suggests nanoparticles are still stable. The stability is preserved even 1 hour after dispersing in RPMI, but 24 hours later, reduction in the peaks corresponding to free proteins and appearance of new peaks at the larger sizes suggests the onset of agglomeration. Moreover, at the 24 hour time-point, there is a significant peak corresponding to the original SPION size spectrum in DI water (solid lines), suggesting the fraction of free SPIONs is still significant, while the amount of agglomerates are few, as seen by the small peaks in the volume distribution at >100 nm.

Finally, we look at the effect of keep PEG/PMAO constant at 30, but changing the PEG chain-length by increasing the molecular weight 20,000 Da (Figure 4-9(c)). As mentioned above in Table 4-3, the hydrodynamic size does increase with an increase in chain-length despite having similar surface PEG densities. However, the alignment of volume and number distributions with the RPMI+10%FBS peaks after SPION dispersion in culture medium suggests that the nanoparticles, despite having the largest core diameter among the three samples, show the best long-term stability. The protein peaks almost completely dominate the size profile even after incubating SPIONs for 24 hours in the serum-rich environment.

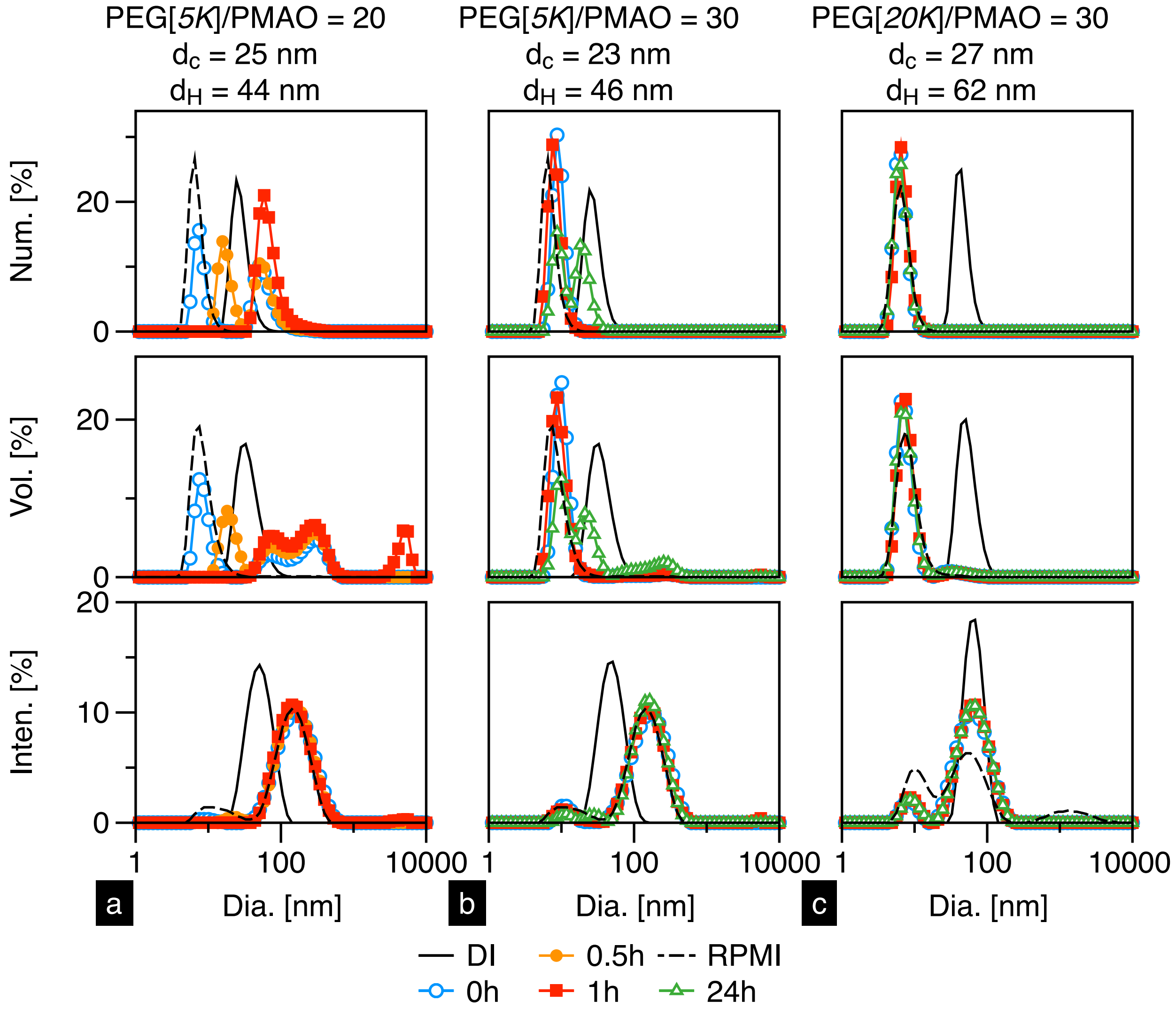

Figure 4-9. Hydrodynamic size evolution of PMAO-PEG coated SPIONs in RPMI+10%FBS cell culture medium. SPIONs with median core diameters over 20 nm were coated with 5,000 Da PEG and a PEG/PMAO surface density of either (a) 20 or (b) 30, or (c) 20,000 Da PEG with a PEG/PMAO = 30. The background DLS spectrum from cell culture medium showed some variance with time alone; hence was measured separately each time (dashed lines).

In summary, increasing the molar amount of PEG conjugated to PMAO from 20 to 30 does improve the colloidal stability of SPIONs in serum-rich cell culture medium, but a longer chain-length PEG shows the most improvement in colloidal stability. The effects of PEG surface density versus chain length were discussed earlier in Chapter 3;

critically, the two counter each other and must be balanced to achieve the optimum configuration on the surface. Increasing polymer density provides SPIONs a higher degree of protection from serum proteins. However, a high surface density also reduces the characteristically high mobility of PEG chains that give the polymer its excellent non-fouling properties. Increasing the chain length alleviates this problem, since mobility increases with molecular weight. The DLS results presented here confirm that balancing the polymer surface density and chain length results in improved long-term colloidal stability in the protein-rich cell culture environment.

4.2.3 Macrophage uptake: an *in vitro* study

The amount of SPION uptake in macrophages is essentially an *in vitro* evaluation of the potential for removal of SPIONs from circulation by the mononuclear phagocytic system (see Chapter 3). Demonstrating low macrophage uptake is crucial in designing SPIONs with long blood circulation times – it enables blood pool imaging in MPI, while in MFH, the longer bioavailability of SPIONs increases the probability of reaching the disease site and delivering high concentrations for efficient hyperthermia therapy. In this section, we will discuss the phagocytic activity of PMAO-PEG coated SPIONs in THP-1 cells. The THP-1 cell line is a monocytic leukemia line that can be differentiated into active phagocytic macrophages using phorbol, 12-myristate, 13-acetate (PMA).

4.2.3.1 Methods

Experimental procedures for seeding and cell differentiation were adopted from a previously published method [88]. Briefly, cells were seeded overnight in a 96-well plate at 50,000 cells/well in RPMI+10%FBS cell culture medium containing 25 nM PMA. Following cell plating and macrophage activation, fresh RPMI+10%FBS media containing SPIONs at various concentrations were added to the adhered THP-1 cells. SPIONs and cells were incubated at 37°C and a 5% CO_2 atmosphere for 72 hours. After 72 hours, the supernatant was carefully decanted and cells were dispersed in sterile 1x phosphate buffered saline (PBS). Cells were incubated at 37°C for 10 minutes to promote cell release, which were then collected and washed three times with 1xPBS by spinning at 500 rpm for 10 minutes. The washing step was done to ensure excess SPIONs not phagocytized were removed. The pelleted cells were dispersed in 200μl 1xPBS and counted in a hemacytometer. For ICP iron quantification of phagocytized SPIONs, cells were digested overnight in 100μl concentrated HCl and diluted by a factor of 12.5 using DI water. Information of samples tested in this study is provided below in Table 4-4. The goal of the study was to evaluate the phagocytic activity as a function of PEG density in PMAO-

PEG(5000) coated SPIONs and subsequently compare with Resovist® – a SPION agent that is also the gold standard in MPI imaging amongst commercially synthesized iron oxide nanoparticles.

Table 4-4. Core and hydrodynamic size information of SPIONs tested in the macrophage uptake study

PEG/PMAO	VSM-d_c nm (σ)	DLS-d_h nm (PDI)
20	16.9 (0.20)	61.2 (0.15)
30	17.4 (0.25)	43.7 (0.18)
Resovist®	14.0 (0.45)	72.0 (0.17)

4.2.3.2 Results and discussion

Figure 4-10 summarizes results from two studies; in the first study, SPION uptake in cells was tested as a function of incubation concentration (left, referred to as concentration study), while the second study compared uptake of SPIONs coated with different polymers (right, referred to as the surface coating study). In the concentration study, SPIONs coated with PMAO-PEG(5000) and a PEG/PMAO density of 30 were tested at three different concentrations: 0.1, 0.2 and 0.4 gFe L^{-1}. In general, SPION uptake in cells increased with the incubation concentration and did not show any saturation for the range of concentrations tested.

Next, we look at the surface coating study, which offers some correlation between the nature of surface coatings and their role in SPION phagocytosis. The difference in macrophage uptake between the two PMAO-PEG coated SPIONs was small – despite having different PEG densities and hydrodynamic diameters (Table 4-4), the two samples showed similar phagocytic activity considering the overlap in their respective error bars. Resovist® however, showed about 6-fold more uptake in THP-1 cells than our

PEG coated SPIONs. Since Resovist® SPIONs have a negative surface charge, it is possible they attract a high degree of surface protein adsorption, which eventually results in increased phagocytic uptake. The results presented here corroborate with previously conducted studies that show charged nanoparticles (positive or negative) induce higher phagocytic activity than neutral-surface nanoparticles [70]. More information on the role of surface charge in phagocytic uptake and clearance is found in §3.2. It should be noted that charged nanoparticles do have advantages when non-specific labeling of cells is intended, such as in stem cell tracking studies [89,90]; however, the primary goal in this work was to design long-circulating SPIONs, in which case high phagocytic uptake is undesirable. Our results suggest that the PEG coated SPIONs synthesized in this work should demonstrate a longer blood circulation time than Resovist®.

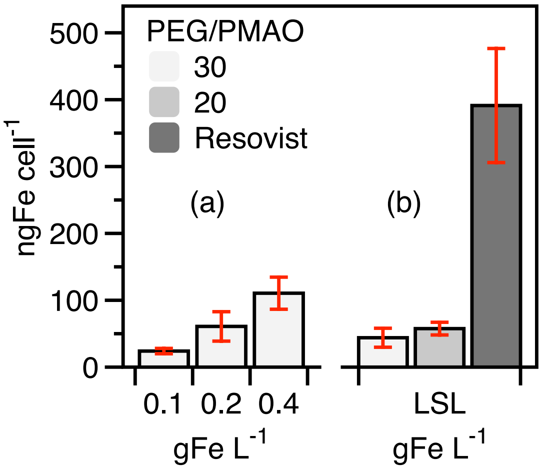

Figure 4-10. Cell uptake of various SPION samples (Table 4-4) in THP-1 cells differentiated as macrophages; samples were incubated for 72 hours. (a) Uptake as a function of concentration using the same sample and (b) for samples with different PEG surface densities; Resovist® is shown for comparison. The *in vitro* results in (b) suggest that the PEG-coated UW SPIONs should have a longer circulation time compared to Resovist®, which shows substantially higher phagocytic uptake.

4.2.4 Cytotoxicity

Colloidal stability in cell culture medium and macrophage uptake studies give critical information about SPION interaction with the physiological environment. However, additional information regarding the inherent cytotoxicity of SPIONs is needed. *In vitro* toxicity and viability studies, although not a replacement for *in vivo* studies, offer an effective and inexpensive platform for evaluating cytotoxicity of nanoparticles in cell cultures.

4.2.4.1 Methods

In this work, cytotoxicity of PMAO-PEG coated SPIONs was evaluated in Jurkat cells – an immortalized line of human T lymphocyte suspension cells. In a typical experiment, cells grown in RPMI 1640 medium+10% fetal bovine serum (FBS) were seeded at 20,000 cells/well in a 96-well plate under physiological conditions (37°C and 5% CO_2). In the results presented here, SPION concentrations of 150 μgFe/ml, 300 μgFe/ml and 450 μgFe/ml were tested for 24 hours incubation with cells. A Lactate Dehydrogenase (LDH) assay (Cytotox-ONE®, Promega) was used to determine SPION toxicity by measuring LDH release in medium due to cell membrane disintegration. To complement and verify the toxicity assay, a luciferase cell viability assay (Celltiter-GLO®, Promega) that measures ATP levels was conducted. Appropriate controls were included to ensure assay validity and test for any interference SPIONs or media may have with the assay. A microplate reader was used to measure fluorescence at λ_{ex} = 560 nm and λ_{em} = 590 nm for LDH assay, and a luminescence counter (TopCount, Perkin-Elmer) was used for the luciferase assay. Additionally, for qualitative analysis, bright field images of cells incubated with SPIONs were examined to observe any gross changes in cell morphology.

4.2.4.2 Results and discussion

Cytotoxicity results of PMAO-PEG coated SPIONs (PEG/PMAO = 20) in Jurkat cells are summarized in Figure 4-11. For the lowest concentration tested (150 μgFe/ml), cell viability (luciferase assay) decreased by 25%, but further decrease was limited even after concentration increased by a factor of 2 (300 μgFe/ml) and 3 (400 μgFe/ml). This trend is also observed in the LDH toxicity study, which is complementary to the viability study – it shows ~15% increase in toxicity at the lowest concentration, but negligible increase thereafter. Furthermore, the increase in toxicity (~15%) is less than the decrease in viability (~25%), which is probably due to fundamental differences between the measurement assays. The Luciferase assay reacts with ATP – the energy molecule that characterizes the metabolic activity in cells; in contrast, the LDH assay measures the amount of LDH released from cells with disintegrated cell membranes. Thus, strictly speaking the metabolic activity of Jurkat cells (not viability) decreases by ~25%, and the number of cells with compromised cell membranes (not toxicity) increases by ~15%. Finally, bright field images (Figure 4-12) show that Jurkat cells, which are non-adherent suspension cells (as indicated by their spherical shape), do not undergo any gross morphological changes compared to the cells only control (no SPIONs).

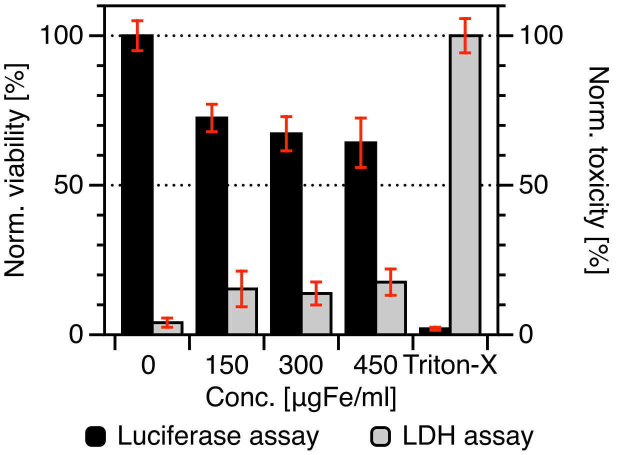

Figure 4-11. The Luciferase viability assay was used to measure the metabolic activity of live cells, while the toxicity assay measured the amount of LDH released from compromised cell membranes. Cytotoxicity data of PMAO-PEG(5000) coated SPIONs in Jurkat cells, showed that viability (left ordinate) decreased by ~25-30% as SPION concentration increased; in comparison, toxicity (right ordinate) was lower at ~15% (see discussion in §4.2.4.2 for more details).

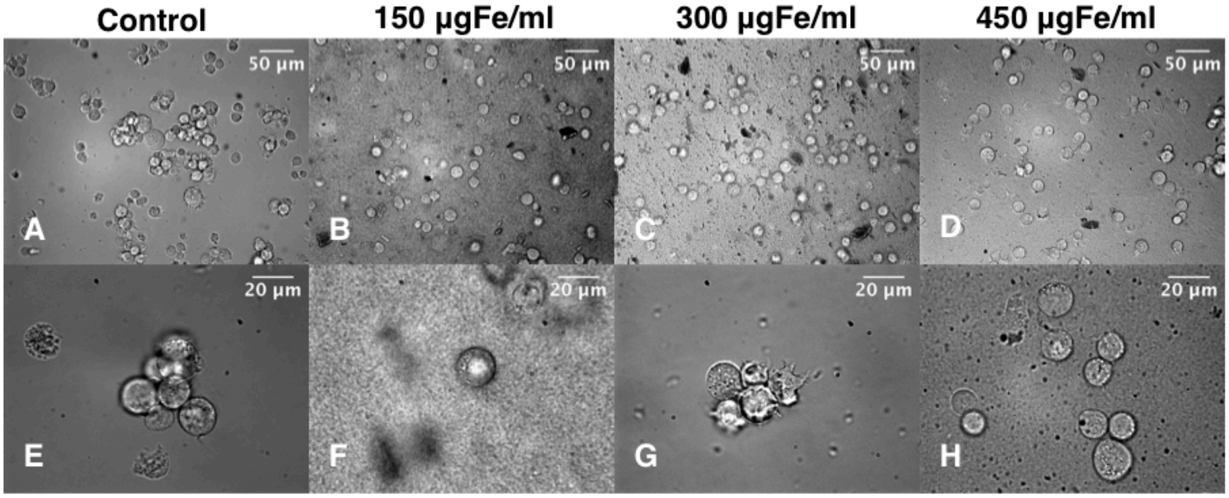

Figure 4-12. Bright field images of Jurkat cells after 24-h incubation with PMAO-PEG coated SPIONs. Images A–D were taken at 20X and E–H at 60X magnification.

4.3 SUMMARY

As discussed earlier in §2.2 and §2.3, performance optimization in MPI and MFH requires precise tuning of the SPION size and size distribution. While organic synthesis methods offer the best control over SPION size and size distribution, the as-synthesized monodisperse SPIONs are hydrophobic, and require additional processing before *in vivo* administration. In particular, SPIONs must be transferred to the aqueous phase and demonstrate long-term colloidal stability and biocompatibility/safety in physiological environments.

In this section, the phase transfer of hydrophobic oleic acid-coated SPIONs using a PEGylated amphiphilic polymer (PMAO-PEG) was discussed. The amphiphilic PMAO polymer presents numerous anhydride sites for PEGylation; thus, changing the PEG/PMAO molar ratio during synthesis varied the PEG density. The molecular weight of the PEG was also varied to study the effect of chain-length on colloidal stability in physiological environment.

The hydrodynamic diameter of PMAO-PEG coated SPIONs in DI water was found to range from 40-60 nm depending on the core diameter, PEG/PMAO ratio (20 or 30) and the PEG chain length; chain length had a greater impact on hydrodynamic size than density. Zeta potential measurements indicated a nearly neutral surface charge, suggesting SPIONs are stabilized primarily via steric repulsion. Furthermore, DLS data showed that increasing PEG density (PEG/PMAO) from 20 to 30 improved colloidal stability in cell culture medium, while increasing the PEG molecular weight from 5,000 Da to 20,000 Da showed the most improvement in stability; the higher mobility of longer PEG chains and surface density must be balanced to minimize protein adsorption to SPION surface.

In the macrophage uptake study, SPIONs coated with PEG/PMAO of either 20 or 30 showed negligible differences in phagocytic activity; instead, SPIONs coated with both variations of PEG showed significantly lower uptake than Resovist® SPIONs, which have a negative surface charge. Finally, a cytotoxicity study in Jurkat cells showed that PMAO-PEG coated SPIONs (PEG/PMAO = 20) in general exhibit low toxicity (~15% from LDH release assay) and reduced the cell metabolic activity by ~25% (from luciferase assay).

Chapter 5.

MPI AND MFH PERFORMANCE OF SIZE-TUNED SPIONS

In this chapter, we will discuss the effects of subjecting size-tuned SPIONs (discussed in Chapter 4) to alternating fields used in MPI and MFH systems, and characterize their corresponding performance; critically, we will explore the effects of core size and size distribution on both MPI and MFH performance. In addition to the core properties, the central role of surface coatings in translating the optimum performance of SPIONs in physiologically relevant environments will be discussed. It will be shown that optimum MPI and MFH performance is ensured only if particles are coated in a non-aggregating state, which allows SPIONs to respond independent of neighboring particles in ac-fields. Before discussing key experiments, an introduction to basic hardware used to characterize MPI and MFH performance of SPIONs is discussed below.

The MPI performance of SPIONs was evaluated experimentally using a home-built magnetic particle spectrometer (MPS). As discussed earlier (§2.2), MPS is a 0-dimension MPI scanner that measures the fundamental SPION *m'(H)* signal used in 3-d MPI scanners. The 25kHz ac-field frequency (f_{mps}) transmitted in the MPS was generated using an arbitrary function generator [Tektronix, Beaverton, OR], and amplified by a 200 W class A RF amplifier [Electronics & Innovation, Rochester, NY]; the excitation field amplitude ($\mu_o H_{p\text{-}p}$) was ~ 36 $\mathrm{mT_{p\text{-}p}}$, or a $\mu_o H_{max}$ ~ 18 mT. The SPION sample – 0.2 ml added to a 0.6 ml centrifuge tube – was inserted such that the sample was located in the center of the transmitter/receive coil assembly. The particle response function (*m'(H)*), introduced in §2.2, for each SPION formulation was obtained by gridding the received signal (*m'(H)*) to the driving field amplitude (*H(t)*). Samples were measured in triplicates and averaged to obtain the final *m'(H)*.

For MFH measurements, a commercial hyperthermia system [magneTherm™, Nanotherics, UK – Figure 5-1] operating at 375 kHz (f_{mfh}) and 17mT field amplitude ($\mu_o H_{max}$) was used. The field conditions used in this study are near the upper threshold of the safety limit ($H_{max} \bullet f_{AC} \sim 5 \text{ x } 10^{-9}$ A m^{-1}s^{-1}) mentioned earlier in §2.3.1. The instrument's transmit coil was wrapped around a hollow acrylic tube to prevent direct contact with the sample tube. Furthermore, the sample tube was insulated with Sytrofoam to minimize heat losses to the environment. For sample preparation, approximately 1 ml of SPIONs was added to the plastic tube and the Styrofoam insulated tube was placed in the center of the coil assembly (Figure 5-1). Temperature was monitored using a liquid immersion fiber-optic thermocouple [Luxtron industrial monitor, Lumasense], which was connected to a computer for real-time data acquisition using the provided TrueTemp software.

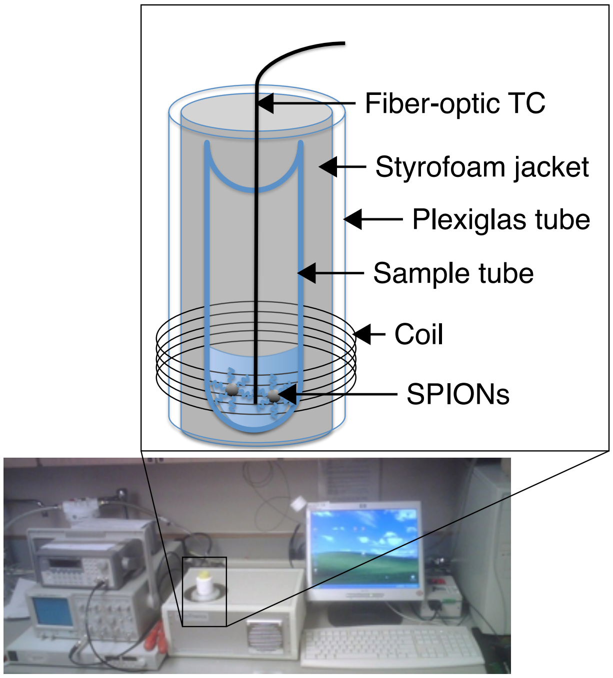

Figure 5-1. Photo showing setup of the commercial hyperthermia system, and a schematic illustration of sample insertion in the coil assembly.

5.1 OPTIMIZING SPIONS FOR MPI

In our previous work [R.M Ferguson, PhD thesis, 2011], we showed that tuning SPION size and size distribution was necessary to optimize MPI performance. The focus was primarily on ensuring the core size was uniformly distributed, and our results showed that maximum MPS signal was achieved for ~20 nm core diameter SPIONs dispersed in DI water. However, theoretical arguments in §2.2.1 suggest that the optimum size in a 25 kHz field is larger and in the size range of 20.6-27 nm, which is in stark contrast with our experimental findings [13]. This discrepancy was attributed to the presence of a broad distribution of sizes in the larger SPION samples, and the role of surface coatings (hydrodynamic size) was thought to be minimal in the experimental study. We later realized that even large SPION cores (>20 nm) with a fairly monodisperse size distribution can show poor MPS performance; hence, a closer inspection of the local SPION environment, and its effect on magnetization reversal, was necessary.

Large SPIONs, especially near the room temperature superparamagnetic transition size (~28 nm), pose a significant challenge in phase transferring due to the strong magnetic attractive forces; as a result, SPIONs bigger than 20 nm core diameter often end up with hydrodynamic diameters significantly larger than that anticipated for singly-coated nanoparticles. Early results indicated that the clustered SPIONs, though in a small fraction, had a mean hydrodynamic diameter of 100 nm and the resulting *m'(H)* was broad and shallow. As discussed earlier in Chapter 2, the energy barrier for magnetization reversal in aggregated nanoparticles increases due to dipole-dipole interactions; consequently, an otherwise monodisperse sample will have a distribution of coercive fields in the *m'(H)* plot if clusters or aggregates are present. One of the key goals of this thesis was to optimize the phase transfer process and tune the PEG-based polymer coating to prevent clustering; thus enabling the use of larger, optimally sized SPIONs for MPI.

5.1.1 The critical role of surface coatings

In this section, we examine the critical role of surface coatings in preserving the relaxation properties of iron oxide cores – the fundamental properties responsible for MPI signal generation – and demonstrating significant improvements in MPS performance; critically, we will examine the effect of removing clustered SPIONs – often the product of phase transfers – on the MPS signal. Nanoparticle clusters were removed via a series of centrifugation steps, followed by careful extraction of the dispersed SPIONs ensuring the pelleted SPIONs remain unperturbed from pipetting; subsequently, the mean hydrodynamic diameter and MPS signal were monitored. For instance, it was found that the hydrodynamic size of 22.5 nm core diameter SPIONs progressively decreased post-centrifugation (Figure 5-2 (a)), while the MPS signal [V $mgFe^{-1}$] and shape improved (Figure 5-2(b)). Specifically, the mean hydrodynamic diameter decreased from 137.9 nm (PDI = 0.33) to 54.8 nm (PDI = 0.147), the mass normalized MPS signal (Figure 5-2(b)-top) improved almost 1.7-fold, and the FWHM narrowed by ~24% (Figure 5-2(b)-bottom).

It is clear that the improved MPS performance is a direct consequence of removing clustered SPIONs and reduction in hydrodynamic size. Figure 5-3 shows the improvement in MPS performance compared to our previous results that showed MPS signal peaking at around 20 nm [13]. The MPS signal in 25 nm SPIONs is approximately 0.22 V $mgFe^{-1}$ – a 2.5-fold improvement from our results in [13]. These improvements are highlighted in a recent publication [55]. We also compare the performance of Resovist® SPIONs, which show significantly poor performance due to its bimodal size distribution [91]. The latter, despite its sub-optimal performance, offers the best MPI performance amongst commercially available SPIONs and was used to demonstrate the first 3-dimensional real-time *in vivo* MPI image in a mouse model [50]; thus, a direct comparison is useful for benchmarking. Table 5-1 highlights the 4.4x greater signal and 56% narrower FWHM from 25 nm UW sample in comparison to Resovist®.

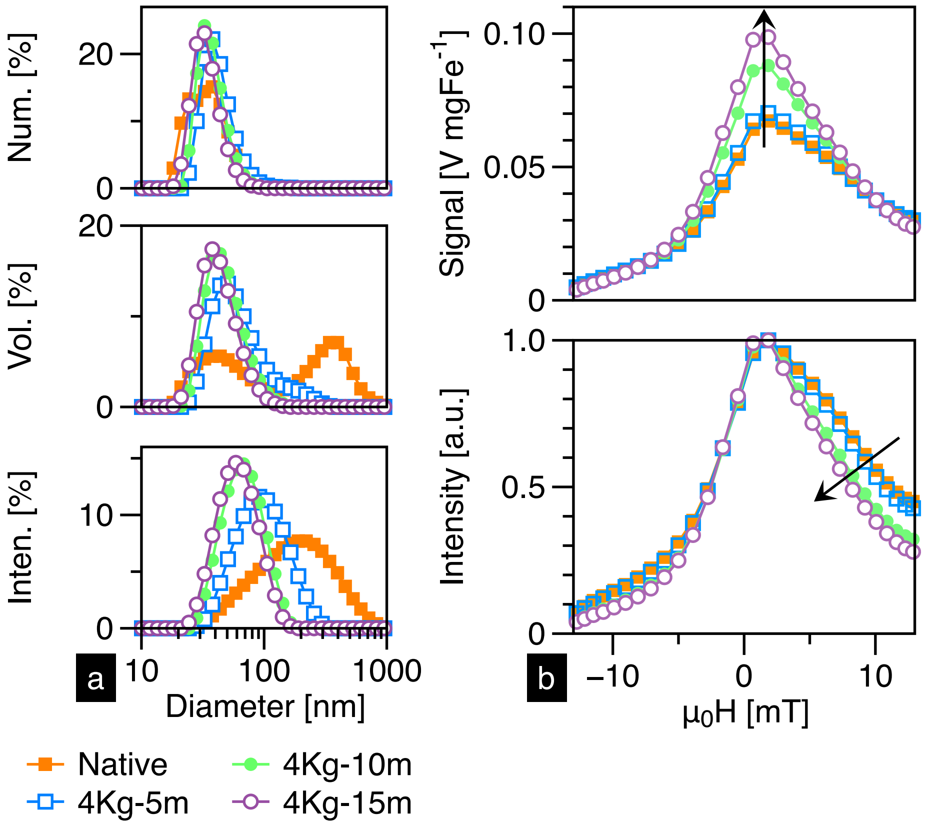

Figure 5-2. (a) Hydrodynamic diameter of 22.5 nm [core dia.] SPIONs decreases after removing clusters with centrifugation. The spin rate was held constant at 4,000g (4Kg), only varying the time from 5-15 minutes. (b) The mass (top) and intensity (bottom) normalized *m'(H)* plots of the same SPIONs showed that the signal increased and FWHM narrowed, respectively, after centrifugation. This study showed that removing clusters reduced hydrodynamic size, which correlated directly with improved MPS performance.

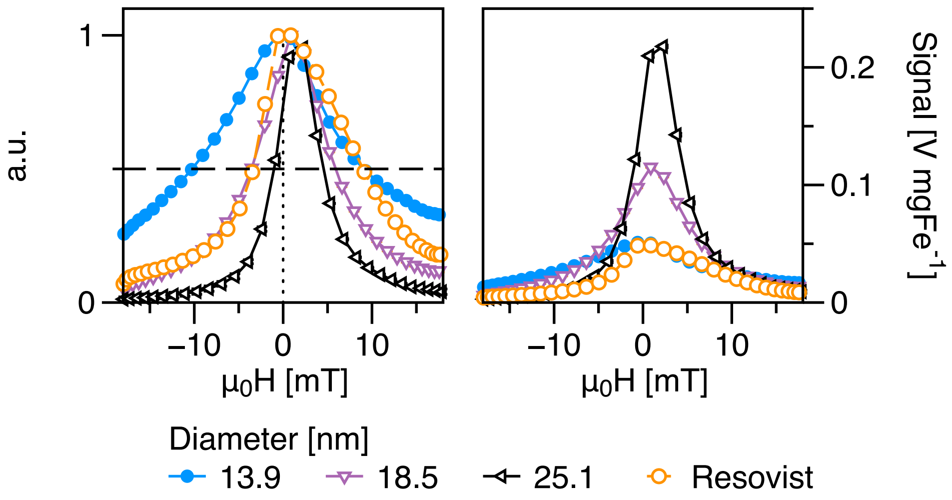

Figure 5-3. Intensity (left) and mass (right) normalized *m'(H)* curves of UW SPIONs with different core diameters and coated with PMAO-PEG (5000); measurements were done in DI water in our home-built MPS operating at 25 kHz and $36\mathrm{mT}\mu_0{}^{-1}{}_{\text{p-p}}$. These experimental measurements confirm theoretical arguments that increasing core size increases susceptibility (§2.1.2), and as a result, improves *m'(H)* response (§2.2.1). Resovist®, a commercially available carboxy-dextran coated SPION contrast agent designed for enhancing T2-MRI, is shown for comparison. All SPIONs, except for Resovist®, were centrifuged at 4,000 rcf for 15 minutes before MPS measurements.

Table 5-1. Comparison of physical properties and MPI performance between Resovist® and optimized SPIONs labeled as 'UW'. Resovist® is used for comparison because it offers the best MPI performance amongst commercially available SPION contrast agents; however, its performance is significantly below theoretical predictions. We show that tuning the size to ~25 nm (core dia.), which is optimal for the applied field conditions in MPI, the signal is 4.4-fold greater and FWHM is 56% narrower than Resovist®.

Sample	Coating	VSM-d_c [nm]	DLS-d_h [nm]	*Signal* [V mgFe^{-1}]	FWHM [mTμ_0^{-1}]
UW	PMAO-PEG(5000)	25.1 (0.14)	46.1 (0.13)	0.22	5.5
Resovist®	Carboxy-dextran	14.0 (0.47)	72.0 (0.17)	0.05	12.4

5.1.2 MPI performance of SPIONs in cell culture medium

So far, we have looked at the MPS signal of SPIONs dispersed in DI water, which is a highly favorable environment for preserving the colloidal stability of PEG-coated SPIONs. *In vivo*, however, SPIONs circulating in the blood face a host of proteins, such as opsonins, that can promote inter-particle aggregation and subsequent sequestration to the reticuloendothelial system (RES) if adsorbed to the surface (Chapter 3); hence, it is critical that the surface adsorption of such proteins is postponed to prolong SPION blood half-life. In order to test the colloidal stability of SPIONs in protein-rich environments, we characterized the MPI performance of optimized SPIONs in cell culture medium containing 10% fetal bovine serum (FBS). This study provided a critical metric for evaluating the robustness of surface coatings in preserving MPI performance of SPIONs in physiologically relevant environments.

Three SPION samples within the optimum size range (23-27 nm, core dia.) for MPI were coated with either one of three different kinds of PMAO-PEG polymers: PMAO-PEG(5KDa), with a PEG/PMAO density of 20 or 30 and a PMAO-PEG(20KDa) at a PEG/PMAO of 30. In contrast to the DLS data presented in Figure 4-9, MPS data provides insight into the relaxation behavior of SPIONs in the biological environment – together the two methods enable us to probe the physical changes in SPIONs that can affect MPS performance. In order to get a complete picture of the *m'(H)* plots, both forward and reverse scans are shown in Figure 5-4. The low PEG density SPIONs show immediate degradation in *m'(H)* after dispersing in RPMI medium; the appearance of peaks at –10 mTμ_0^{-1} and +10 mTμ_0^{-1} suggest a high coercive field required for magnetization reversal, which occurs when SPIONs are interacting due to potential agglomeration. The colloidal stability data for the same sample presented in Figure 4-9(a) confirms that SPIONs are indeed agglomerating. In contrast, the improvement in colloidal stability (Figure 4-9(b)) of SPIONs coated with a higher PEG density (PEG/PMAO = 30) translates to MPS measurements (Figure 5-4(b)), which show that *m'(H)* curve is relatively unperturbed even 24 hours post-RPMI dispersion.

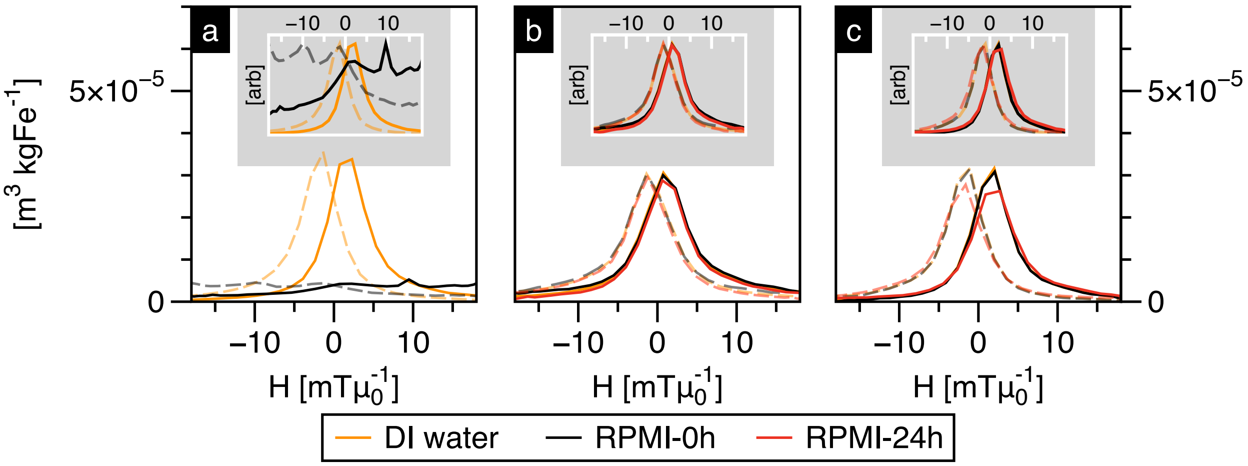

Figure 5-4. *m'(H)* plots in DI water and serum-rich cell culture medium of (a) 25 nm SPIONs [core dia.] coated with PEG(5K)/PMAO of 20, (b) 23 nm SPIONs coated with PEG(5K)/PMAO of 30 and (c) 25 nm SPIONs coated with PEG(20K)/PMAO of 30.

Finally, the effect of increasing PEG molecular weight from 5,000 Da to 20,000 Da – without changing PEG density (PEG/PMAO = 30) – also preserves the native *m'(H)* response of SPIONs in serum-rich medium. Note that the core size of SPIONs tested in (a) and (c) is identical, including their respective *m'(H)* curves in DI water. However, while the SPIONs coated with the 20,000 Da molecular weight PEG (PEG/PMAO = 30) performed excellent in cell culture medium, the 5,000 Da coated SPIONs, with a PEG/PMAO = 20 perform poorly.

Our results show that colloidal stability – measured using DLS (Figure 4-9) – correlates directly with MPS signal (Figure 5-4). By preventing the SPION cores from agglomerating and magnetically interacting, we preserve the magnetization reversal characteristics of SPIONs, which forms the physical basis of signal generation in MPI (§2.2). In summary, surface coatings play a critical role in preventing protein adsorption – important for long blood circulation (§3.3) – and preserving the MPS performance – important for acquiring images from circulating SPIONs – of MPI-optimized SPIONs in physiological environments.

5.1.3 Phantom imaging of MPI-optimized SPIONs

Before our MPI-optimized SPIONs can be administered *in vivo* for imaging in some of the world's first prototype MPI scanners at Philips Medical Imaging (Hamburg, Germany) and University of California (Berkeley, CA), it was critical to evaluate their imaging performance in simple phantoms, and perform a side-by-side comparison with Resovist® – the commercial SPION agent used to establish a benchmark in the first MPI images [1,50]. Phantom imaging experiments will also help determine the translation of MPS characterization to actual imaging, which is a necessary step before devoting large number of resources for future animal experiments.

Philips and UCB are two pioneers in MPI hardware development – both employ distinct approaches to image reconstruction. The former uses the fast *system matrix* approach and the latter uses the *x-space* imaging approach. The *system matrix* approach uses the fourier transform of the *m'(H)* signal to generate and store a system function that is unique for each SPION tracer – this enables rapid imaging using Lissajous trajectories for the FFP in the imaging volume. On the other hand, *x-space* image reconstruction correlates the *m'(H)* MPI signal from SPIONs to the current position of the FFP – for details on the two image reconstruction methods, see [52,53]. Regardless of the image reconstruction approach, SPIONs remain the centerpiece of MPI physics, and optimizing their properties for the field conditions used in MPI (25 kHz and 20 $\mathrm{mT}\mu_o^{-1}{}_{max}$) applies to both imaging approaches.

5.1.3.1 Methods

For the phantom images acquired at Philips and UCB, SPIONs with a core diameter of 25 nm and a hydrodynamic diameter of 50 nm were compared side-by-side with Resovist®. Both scanners applied a 25 kHz modulating field to excite SPIONs. The Philips scanner applied a 16 $\mathrm{mT}\mu_o^{-1}{}_{max}$ field amplitude and the field gradient was 1.25 $\mathrm{T}\mu_o^{-1}\mathrm{m}^{-1}$ in the x and y directions, and 2.5 $\mathrm{T}\mu_o^{-1}\mathrm{m}^{-1}$ in the z-direction. The field amplitude in the UCB scanner was 23 $\mathrm{mT}\mu_0^{-1}{}_{\mathrm{max}}$ and the field gradients were 7 $\mathrm{T}\mu_0^{-1}\mathrm{m}^{-1}$ in the x direction, and 3.5 $\mathrm{T}\mu_0^{-1}\mathrm{m}^{-1}$ in the y and z directions. Phantoms prepared at Philips – the letters “P” and “H” – were constructed from clear plastic tubing with inner diameter of 1.5 mm (Figure 5-5(a and b)). The UCB phantoms containing the letters “U” and “W” were laser-cut in 1.5 mm (width) x 1.5 mm (depth) channels in clear acrylic (Figure 5-5(d and e)). The concentration of both UW and Resovist® SPIONs was equivalent in the corresponding phantoms: 0.95 gFe/L in the Philips image, and 0.29 gFe/L in UCB image. In order to quantitatively compare signal and spatial resolution of UW SPIONs with Resovist®, point-source phantoms containing 0.8 gFe/L nanoparticles were imaged (Figure 5-5(f)) in the UCB scanner.

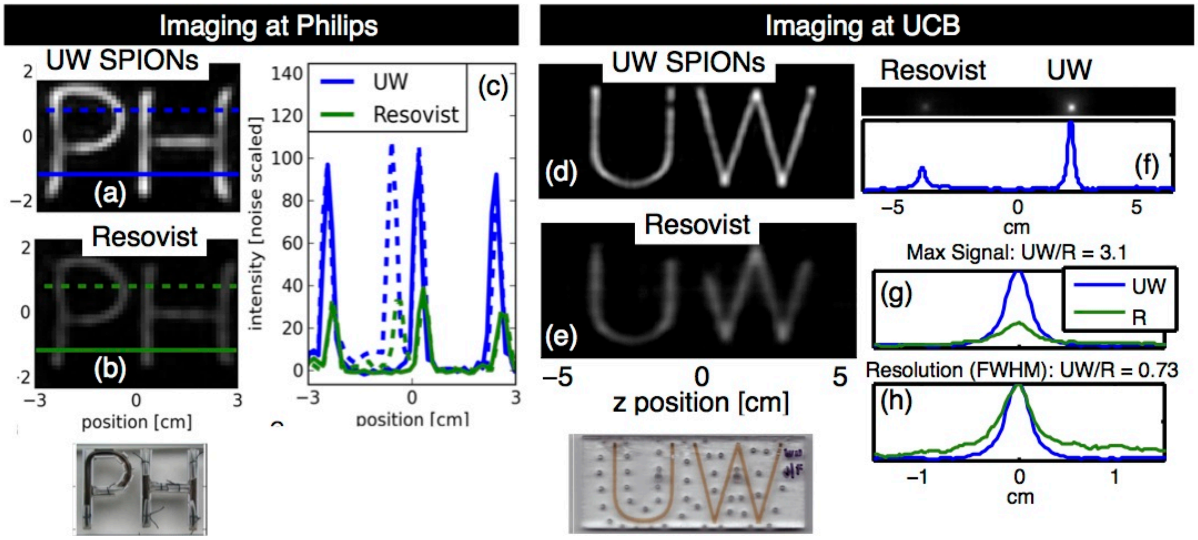

Figure 5-5. Phantom imaging experiments showing side-by-side MPI image comparison between UW SPIONs and Resovist®. Imaging was performed independently in prototype MPI systems at Philips (a and b) and UCB (d and e). For comparative purposes, concentrations of both UW and Resovist® SPIONs are identical. In both scanners, images from UW SPIONs (a and d) are visibly brighter than from Resovist® (b and e). (c) Intensity line profile across the phantom shows that signal from UW SPIONs is 3x greater than Resovist®. (f) In order to quantify the signal and spatial resolution, point-source measurements (3µl SPIONs at 0.8 gFe/L; samples were contained in 1.59 (dia.) x 1.5 mm (len.) cylinders) were performed in the UCB scanner. UW SPIONs showed 3.1x greater signal (g) and 27% better spatial resolution than Resovist® (h).

5.1.3.2 Results and discussion

Images taken in both Philips and UCB scanners show that UW SPIONs are visibly brighter than Resovist®. The intensity profile of the "PH" phantoms in Figure 5-5(c) shows that UW SPIONs produce a 3x brighter image than Resovist® SPIONs. Point-source measurements in the UCB scanner provide a quantitative comparison between UW and Resovist® SPIONs – UW SPIONs show 3.1x greater signal and 27% better spatial resolution than Resovist® SPIONs. A key conclusion of the phantom images is that UW SPIONs, which are optimized for MPI performance, show consistently better performance than Resovist®, regardless of the imaging approach; critically, both imaging approaches demonstrate a 3-fold improvement in signal. Spatial resolution is difficult to compare in the Philips phantom image, but the FWHM of the point-source image in Figure 5-5(h) shows a linear spatial resolution of 2.9 mm for UW SPIONs and 3.9 mm for Resovist® SPIONs. It should be mentioned that the FWHM of 25 nm UW SPIONs from MPS measurements ($6.5\ \mathrm{mT}\mu_0^{-1}$; Figure 5-3) predicts a 0.9 mm spatial resolution in the $7\ \mathrm{T}\mu_0^{-1}\mathrm{m}^{-1}$ field-gradient used in UCB's MPI scanner. This discrepancy in spatial resolution is not yet understood, and may be due to fundamental differences in SPION relaxation behavior in the 0D MPS and 3D MPI scanner, which consists of a large $7\ \mathrm{T}\mu_0^{-1}\mathrm{m}^{-1}$ field-gradient.

5.2 Optimizing SPIONs for MFH

Like MPI, MFH uses alternating magnetic fields to excite the superparamagnetic response of SPIONs; however in MFH, the field performs additional work on magnetization reversal, which results in energy loss in the form of heat. Theoretical discussions in §2.3 suggest that the optimum size for MFH depends on the anisotropy constant (Table 2-2 and Table 2-3). However, experimental measurement of the anisotropy constant is nontrivial and requires special equipment, such as ac-susceptometers or magnetic relaxometers, that are not readily accessible. Secondly, the anisotropy constant is found to vary with the core size – often increasing with decreasing nanoparticle volume; as a result, using a single anisotropy value to predict the optimum diameter is not ideal. Here we demonstrate an empirical approach to find the optimum SPION size by measuring SLP as a function of nanoparticle core diameter. The latter is possible thanks to exceptional ability of the thermal decomposition synthesis method to control SPION core size and size distribution over a wide range (5-30 nm). Finally, as was the case with SPION optimization for MPI, measurements in samples containing clusters were performed first [92]. After adopting the centrifugation step to remove clusters, larger SPION samples were tested again and compared with past results.

5.2.1 Methods

In this work, a commercially available MFH system was used to transmit a 375 kHz ac-field frequency with an amplitude of 17 $\mathrm{mT}\mu_0^{-1}{}_{\mathrm{max}}$. Prior to measuring the heating rates (*dT/dt*) of samples in the ac-field, the background temperature was measured for 60 seconds with the field turned off. The field was then turned on for 300 seconds and the liquid immersion fiber-optic thermocouple was used to record real-time temperature data. Figure 5-6 shows the concentration normalized heating rates of different core diameter SPIONs in DI water. Data on the left was acquired before the centrifugation step was adopted as a routine step, and shows that 16 nm SPIONs show maximum rise in temperature – over 6°C in the 300 seconds of heating. On the other hand, after incorporating the centrifugation step for removing clusters, larger SPIONs show even higher heating rates – a maximum temperature rise of over 8°C was observed in 27 nm SPIONs. The specific loss power (SLP; W/gFe_3O_4) was subsequently calculated from the heating rates according to Eq. 2-26, where the slope of the heating curve from 70 to 130 seconds is used to find *dT/dt*. SPION concentration – referred to as "MNP conc." in the figure – was determined from ICP analysis of the samples.

5.2.2 Results and discussion

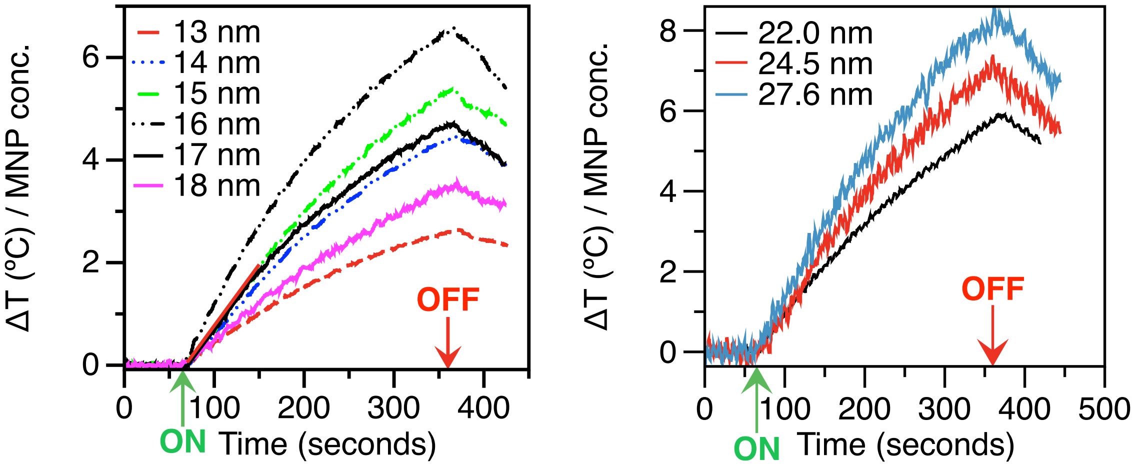

Figure 5-6. Concentration normalized heating rates of SPIONs with different core diameters. Heating rates on the left were measured before employing the cluster-removal step; on the right, clustered nanoparticles were removed.

Like the figure above, Figure 5-7 shows SLP measurements as a function of core diameter (d_c) both prior (Figure 5-7(a)) and after (Figure 5-7(b)) adoption of the centrifugation step. In Figure 5-7(a), SLP is categorized for two sets of SPION samples based on their average size distribution, where σ_{avg} is the average standard deviation of $\ln(d_c)$ – see §2.2.3 for more information on the lognormal distribution function. The data suggests that there is a peak in SLP at 16 nm for the frequency and amplitude used.

Assuming 16 nm is indeed the optimum diameter, we can use Eq. 2-31[§§] to find the corresponding anisotropy constant, which comes out to ~26 kJ m^{-3} – more than twice the bulk anisotropy value of magnetite (11 kJ m^{-3}). Additionally, SPIONs with a broader average size distribution (σ_{avg} = 0.33) showed an overall drop in the peak SLP value relative to SPIONs with a σ_{avg} = 0.15. This general result agrees with theoretical models that suggest a decrease in SLP as size distribution increases [34,35,41]; hence, it is critical that size distribution must be as narrow as possible to get maximum heating in MFH.

Next, we turn our attention to more recent SLP measurements that were performed with SPION samples that were centrifuged to remove clusters (Figure 5-7(b)). Note that there is no peak in SLP as a function of size, as it continues to increase with size. The slope does reduce, which in fact corroborates well with the Stoner-Wohlfarth model used to predict power losses. The solid line is the fit to the raw data assuming the Stoner-Wohlfarth model; best fit was obtained by allowing the anisotropy constant, K_{eff}, and the standard deviation, σ_{avg}, to vary freely. The fitting curve expression was derived from substituting Eq. 2-29 and Eq. 2-31 in eq. Eq. 2-30; the resulting expression for hysteresis area was used to plot SLP, which is $\frac{Af_{AC}}{\rho_{Fe_3O_4}} * f(d_c)$, where $\rho_{Fe_3O_4}$= 5.2 g cc^{-1} and $f(d_c)$ is the lognormal size distribution function. Fitting the raw data with the SLP equation gives a K_{eff} ~ 22 kJ m^{-3} and a σ_{avg} ~ 0.3. The anisotropy value falls in the range expected for nanoparticles: 23-40 kJ m^{-3} [41].

[§§] For the field conditions and sizes used in this study, LRT is not valid since $\xi > 1$.

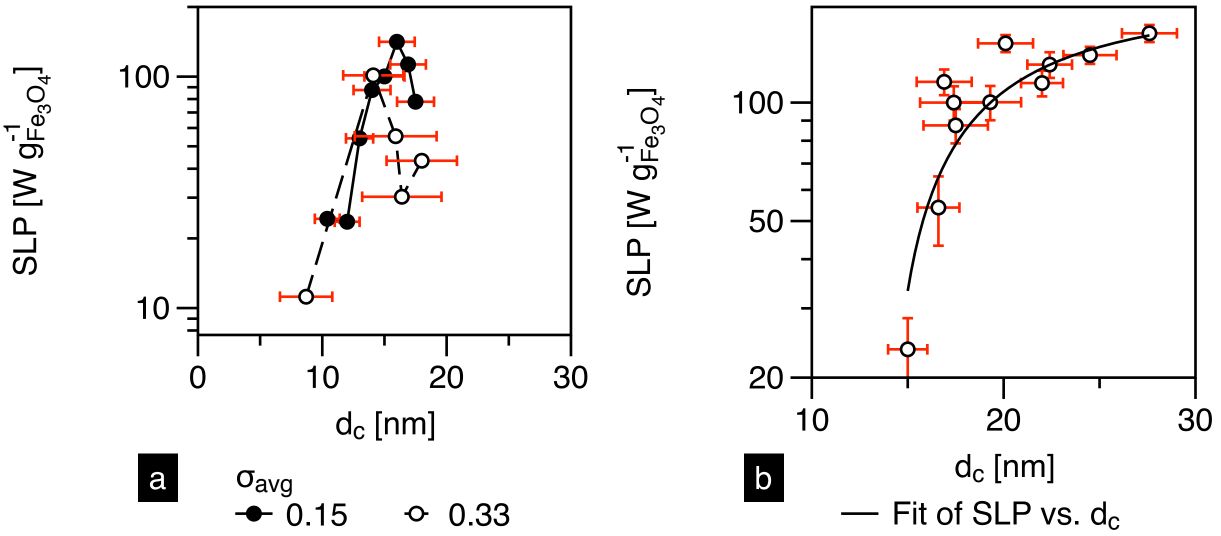

Figure 5-7. Specific loss power (W $g^{-1}Fe_3O_4$) as a function of size and size distribution measured at 375 kHz and 17 mT_{max}. (a) Results from 2011 [92] and (b) recent results after removing clusters from larger SPION samples.

In conclusion, recent results presented in Figure 5-7(b) show that SLP continues to increase with size for the field conditions used in this work (375 kHz; 17 mT_{max}), unlike the previous case that suggested a peak in SLP around 16 nm. The reason for this change can be attributed to the removal of clusters, which broaden the overall size distribution and also exhibit coercive fields potentially higher than the field amplitude.

5.3 *IN VITRO* MFH PERFORMANCE

In order to demonstrate MFH efficacy, we measured *in vitro* viability of Jurkat cells (immortalized T lymphocytes cell line) after incubation with SPIONs and application of an ac-field. Jurkat cells were cultured in triplicates at a density of 10,000 cells/well in 96-well plates. The SLP of three samples with core diameters of 12 (σ = 0.09), 13 (σ = 0.22) and 16 (σ = 0.16) nm samples were measured at 375 kHz and 17mT field amplitude ($\mu_o H_{max}$) in the magneTherm™ hyperthermia system; SLP values were 23.6, 54.1 and 140.0 W/gFe_3O_4 for the 12, 13 and 16 nm SPIONs, respectively. SPIONs with varying concentrations (0–600 μgFe/ml) were added to the cultured cells and incubated at 37°C for 15 minutes to stabilize temperature prior to turning the ac-field on. After temperature equilibration, the ac-field in the magneTherm device was applied for 15 minutes, and cells were returned again to the 37°C incubator for 15 minutes. Finally, cells were allowed to equilibrate to room temperature for an additional 30 minutes before viability measurements were performed using the Celltiter-GLO® luciferase assay.

As expected, increasing SPION concentration increases the absolute power loss; consequently *% viability* decreases with increase in concentration (Figure 5-8), but inducing cell death by increasing SPION concentration does not reflect an improvement in the overall therapeutic potency of MFH due to possible interference from some cytotoxic effects of incubating cells with SPIONs. Figure 5-9 demonstrates the significant decrease in *% viability* due to the 16 nm sized SPIONs compared to the 12 and 13 nm SPIONs at similar concentrations, suggesting the higher SLP of the larger SPIONs is responsible for the improvement in therapeutic potency of MFH. It is possible to get even greater cell death using bigger nanoparticles that show higher heating rates; however, at the time of the aforementioned experiment, bigger SPIONs contained clusters that deteriorated overall MFH performance and were unsuitable for the study.

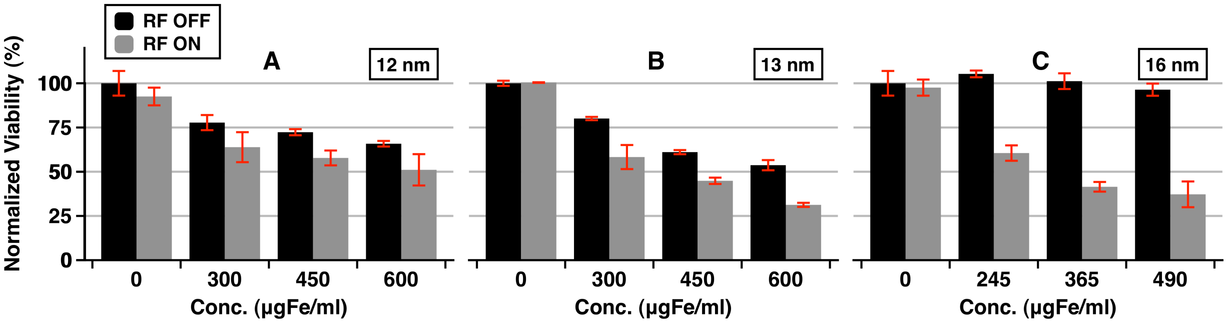

Figure 5-8. In vitro heating of Jurkats using SPIONs of diameters (A) 12 nm, (B) 13 nm and (C) 16 nm. The 375 kHz (17 $mT_{p\text{-}p}\mu_0^{-1}$) radiofrequency (RF) field was applied for 15 minutes.

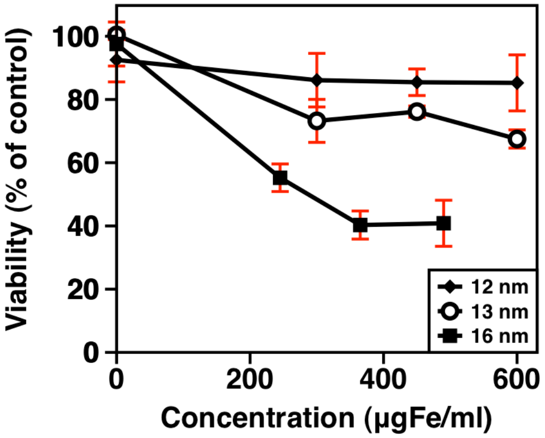

Figure 5-9. Decrease in cell viability relative to the control calculated as RF $OFF_{avg.}$ – RF $ON_{avg.}$ The higher SLP of 16 nm SPIONs (140 W/gFe_3O_4) resulted in the maximum decrease in cell viability due to heating in an RF field compared to 12 nm (SLP = 23.6 W/gFe_3O_4) and 13 nm (SLP = 54.1 W/gFe_3O_4) SPIONs.

5.3.1 Intracellular MFH

The hyperthermia efficacy experiments presented above were conducted with the SPIONs dispersed in the same environment as the Jurkat cells; critically, cells were not allowed to uptake SPIONs due to the short incubation times, and thus heating was primarily thought to be extracellular. In this section, we attempted to test the efficacy of hyperthermia therapy when cells are allowed to internalize SPIONs. Jurkat cells were chosen for this experiment to facilitate a direct comparison between extra- and intracellular MFH experiments.

5.3.1.1 Methods

In order to promote internalization in Jurkat cells, a modified protocol on electroporation (EP) of Jurkat cells was adopted [93]. 1×10^6 Jurkat cells were dispersed in 500 µl serum-free RPMI medium containing SPIONs, and transferred to 0.4 cm electroporation cuvette. The core and hydrodynamic diameter of SPIONs were 21 nm (σ = 0.13) and 63 nm (PDI = 0.08), respectively, and the SLP was 110 W $g^{-1}Fe_3O_4$. Controls for each SPION concentration (a total of 3 were tested) included cells+SPIONs, cells+SPIONs+EP and cells+SPIONs+AC, where AC refers to the ac-field. The three controls are referred to as “control”, “EP” and “AC” in the figure below to remove redundancy and the test sample is labeled as “EP+AC”. The change in viability was measured w.r.t. a single ‘cells only’ control (not shown in plot). The various mixtures were place on ice for 10 minutes before EP, after which they were electroporated using the following conditions: 250 V, 720 Ω and 100 µF. After electroporation, the various mixtures (including controls) were diluted to get the desired SPION concentrations for incubations: 33,333 and 667 µgFe/ml. Cells were allowed to recover for 48 hours, then harvested, washed to remove excess non-internalized SPIONs and tested for viability using the luciferase assay.

5.3.1.2 Results and discussion

Unfortunately, it was found that electroporation had a significant toxic effect (Figure 5-10) on Jurkat cells even after using a much lower capacitance than the recommended value of 960 μF. Furthermore, the 'control' samples also showed significant toxicity; as a result, the lack of appropriate controls for reference, the results are for the most part inconclusive. In future experiments, it is recommended an alternative approach to internalization be used. Secondly, the 48 hours incubation time with SPIONs might be too long and consequently show significant toxicity to cells; it is suggested that shorter incubation times be used.

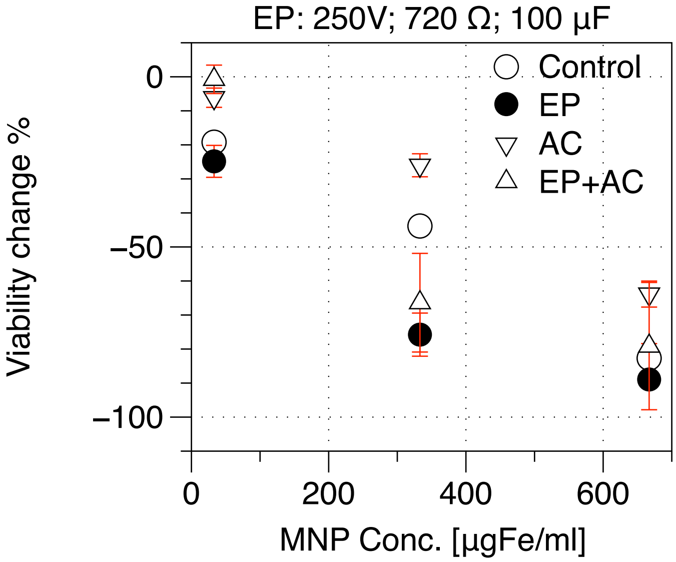

Figure 5-10. Results from a preliminary experiment conducted to study the efficacy of intracellular MFH. To promote SPION internalization in Jurkat cells, electroporation was used.

5.4 SUMMARY

The thermal decomposition method gives precise control over SPION size and size distribution, and thus their magnetic properties – a critical requirement for synthesizing size-tuned SPIONs that optimize MPI or MFH performance for any applied frequency. In MPI, the role of surface coatings in ensuring non-interacting cluster-free SPIONs following their transfer to aqueous phase was found to be critical in translating the tailored core properties for optimum *m'(H)* in the serum-rich physiological environment. From DLS data (Figure 4-9) and *m'(H)* plots (Figure 5-4) measured in the 25 kHz home-built MPS, it was found that increasing the PEG density from 20 to 30 improved colloidal stability and preserved MPS performance in serum-rich cell culture medium. Furthermore, increasing the PEG molecular weight from 5,000 Da to 20,000 Da also provided excellent protection from protein adsorption as demonstrated by the DLS and MPS data. By tuning the PEG-based surface coatings to prevent aggregation of the magnetic cores, we were able to correct usage of bigger SPIONs (>20 nm dia.), which showed a substantial factor of improvement over the commercial MPI standard Resovist® – a factor of 4.4 improvement in signal and 2.25 in FWHM resolution (Table 5-1) as characterized in MPS. Such optimized SPIONs show promise as angiography tracers and blood-pool agents for the emerging MPI imaging modality. However, it is critical to evaluate the imaging performance of optimized SPIONs in phantoms before devoting resources to animal experiments, and determine whether MPS evaluation of SPIONs translates to imaging in 3-d MPI scanners. Regardless of the imaging system – Philips and UCB MPI scanners operating at 25 kHz drive frequency were used – 25 nm (core dia.) UW SPIONs consistently showed 3x greater signal than Resovist® SPIONs. Furthermore, a point-source measurement showed a 27% improvement in spatial resolution over Resovist®.

In MFH, SPIONs were evaluated in a 375 kHz/17 $\mathrm{mT_{max}}$ alternating field applied using a commercial hyperthermia system. Previous results [94] had shown a peak at approximately 16 nm in SLP as a function of nanoparticle diameter; however, recent measurements showed that SLP continued to increase with diameter. Unlike the previous case, recent samples underwent a post-processing step that helped remove clustered SPIONs – the result was improved heating performance in bigger SPIONs that was consistent with the Stoner-Wohlfarth model's predicted SLP behavior (Figure 5-7). *In vitro* heating in Jurkat cells using SPIONs dispersed in the surrounding medium (extracellular) demonstrated the feasibility of MFH therapy, whereas preliminary intracellular heating experiment was inconclusive in determining whether intracellular heating is superior than extracellular heating. The author Y. Rabin [95] argues through models that there is no real advantage in intracellular hyperthermia; however, experimental evidence is still lacking.

So far we have investigated the MPI and MFH performance of SPIONs in physiologically relevant environments, including serum-rich cell culture medium and cell cultures. In the next section, *in vivo* biodistribution and pharmacokinetics of PMAO-PEG coated SPIONs in mice are discussed.

Chapter 6.

IN VIVO BIODISTRIBUTION AND PHARMACOKINETICS OF SPIONS

In Chapter 3, the physiological barriers that affect nanoparticle biodistribution and pharmacokinetics were discussed. SPIONs with a neutral surface charge and adequate surface coating coverage prevent protein adsorption and are prerequisites to developing long-circulating SPIONs. Furthermore, based on biodistribution and circulation characteristics of previously developed SPIONs, a small hydrodynamic diameter – though no smaller than fenestrations in kidney capillaries (~15 nm) – is preferred. The surface characteristics of PMAO-PEG coated SPIONs discussed in §4.2.1 suggest they are good candidates for long-circulation times.

In this section, *in vivo* studies designed to examine the tissue biodistribution and circulation characteristics of PMAO-PEG coated SPIONs in mice are discussed. The main objectives of the study were to (1) investigate tissue biodistribution and clearance of intravenously injected SPIONs and (2) measure the blood circulation time in mice using MPS. While objective (1) is a preliminary assessment of biocompatibility and safety, objective (2) represents a crucial step in developing SPION tracers for future applications in MPI-based vascular imaging. Since pre-clinical and clinical scanners are still under development, MPS offers a rapid and accurate method for assessing SPIONs. Here we will discuss *in vivo* results from a series of SPION samples listed in Table 6-1. The UW samples are labeled so as to reflect their core (d_c) and hydrodynamic size (d_h): UW-d_c-d_h. Furthermore, coating information is also provided; for the PMAO-PEG coated SPIONs, the label 5K/20 refers to the PEG molecular weight (5K Da) and density (PEG/PMAO = 20) respectively. In the case of Resovist®, CD is the abbreviation for carboxy-dextran.

In the first set of *in vivo* studies, which were published in [96], a comprehensive analysis of UW-17-86 was performed. Both biodistribution and blood circulation studies were performed in mice. Since the blood circulation time was characterized using MPS, Resovist® – the only commercial tracer that provides reasonably good MPI performance – was also included for benchmark evaluation. Next, a series of studies were done to evaluate SPIONs as a function of their surface properties. Tissue biodistribution of UW-17-86 was compared with UW-19-51 – both samples had similar core diameters from TEM data and were coated with 5K/20 PMAO-PEG, but the hydrodynamic diameters were different possibly due to the presence of SPION clusters in UW-17-86, and the lack thereof in the case of UW-19-51. Finally, the blood circulation of UW-17-86 was compared with UW-20-42, which has similar core properties but a significantly smaller hydrodynamic size and a higher PEG density coating.

6.1 PREPARATION OF SPIONS FOR *IN VIVO* STUDIES

Details of nanoparticle core synthesis are provided in Appendix A, and the PMAO-PEG coatings were applied according to the procedures discussed in §4.2. For injections in mice, excess polymer and trace organic solvents were removed using sephacryl S-200 HR gel columns [GE Healthcare]. For sterilization, SPIONs were filtered with sterile 0.2-µm syringe filters and dispersed in USP-grade 1X phosphate buffered saline (PBS) at concentration of 0.5, 1.0 or 2.0 gFe/L. Resovist® (~27.9 gFe/L) was acquired from Bayer Schering Pharma AG[***] and was diluted to 2 gFe/L using USP-grade 1X PBS.

6.1.1 Physical properties of SPIONs tested *in vivo*

Physical characterization data of all SPION samples used for *in vivo* studies is summarized in Table 6-1 (details of size characterization methods are presented in Appendix B). Measurements shown in Figure 6-1 confirm that the magnetic properties of UW SPIONs, as determined from VSM (Figure 6-1(c)) and MPS (Figure 6-1(d)) measurements, are quite similar. Comparing the differences in MPS signal between UW SPIONs, the FWHM – determined from the normalized signal plots shown in the inset of Figure 6-1(d) – showed less than 3% difference, while the difference in signal intensity ($VmgFe^{-1}$) was no greater than 5-10%. Resovist®, on the other hand, showed ~20% broader FWHM and ~50% less signal than all UW SPIONs. Furthermore, DLS data in Figure 6-1(b) shows appreciable differences in hydrodynamic size due to the differences in surface coatings. Note that TEM data for Resovist® in Table 6-1 is adapted from Eberbeck et al, who have extensively characterized the commercial agent using various complementary techniques [91]. Their results suggest that Resovist® has a bimodal distribution – it is composed of 5 nm and 24 nm particles. The larger size is a result of ag-

---

[***] Production of Resovist® was discontinued in 2009.

gregated nanoparticles that are frequently observed in TEM images of Resovist® [13]. As a result, the overall size distribution of Resovist® is considerably broader than all UW SPIONs.

Table 6-1. Information of samples tested *in vivo*.

		d_c [nm] (σ)[a]			MPS		14T-MRI	
Sample	Coating	VSM	TEM	d_h [nm] (PDI)	Signal [VmgFe^{-1}]	FWHM [mT]	r2 [mM^{-1} s^{-1}]	Cent.[c]
UW-17-86	5K/20	17 (0.20)	19 (0.15)	86 (0.18)	0.102	9.9	209	No
UW-19-51	5K/20	19 (0.19)	18 (0.09)	51 (0.14)	0.115	9.6	435	Yes
UW-20-42	5K/30	20 (0.14)	-	42 (0.14)	0.110	9.9	348	Yes
Resovist	CD	14 (0.47)	5 (0.37)[b]	72 (0.17)	0.048	12.4	268	No

[a] σ is the standard deviation of the lognormal distribution function

[b] TEM data from Eberbeck et al

[c] Centrifugation conditions were 4,000 rcf for 15 minutes

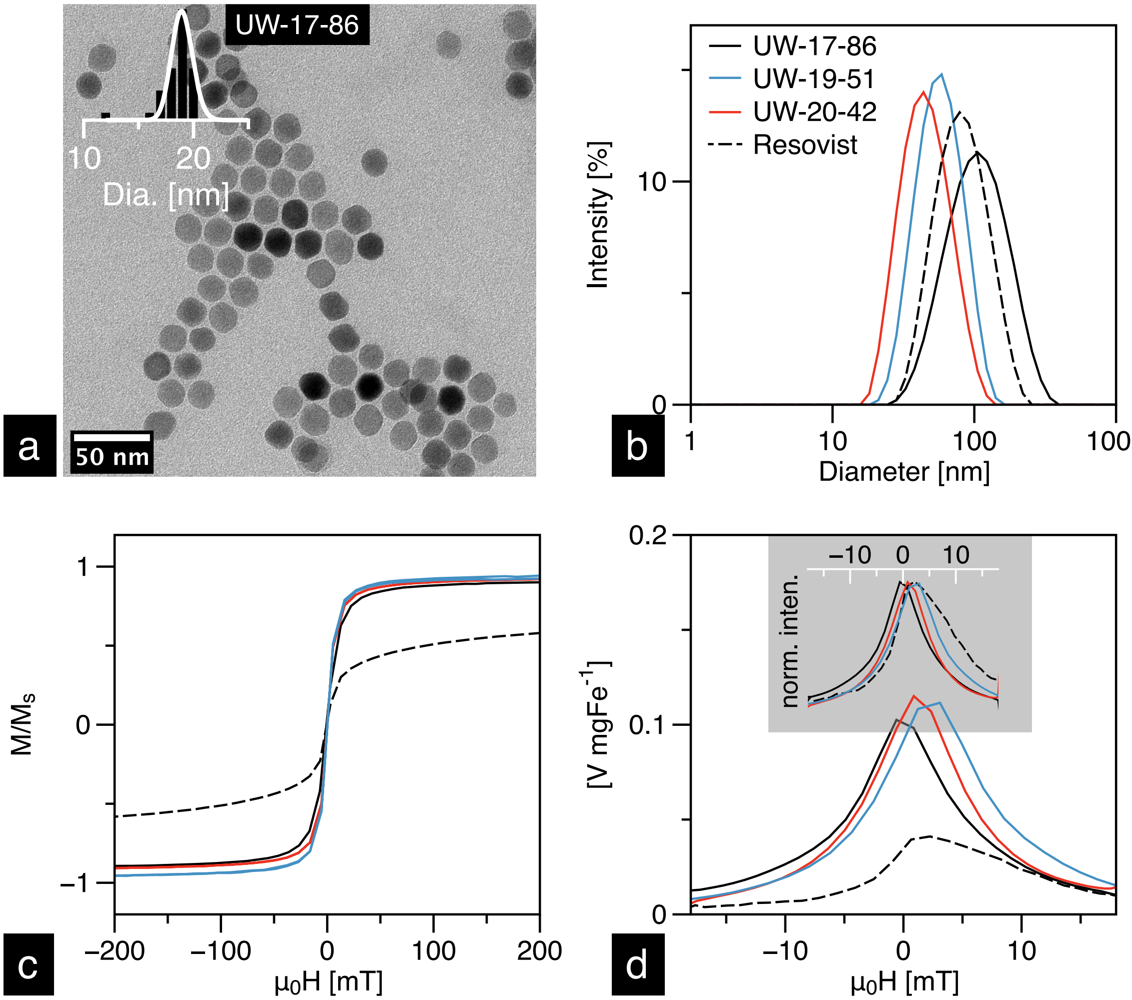

Figure 6-1. (a) TEM image of UW-17-86 and its corresponding histogram (inset) fit to a lognormal size distribution. Characterization of various UW samples (solid colored lines) and Resovist® (dashed) SPIONs in DI water: (b) hydrodynamic size measured using DLS; (c) static magnetization response measured in VSM; (d) intensity (top) and mass (bottom) normalized *m'(H)*s measured in our 25 kHz MPS. A summary of the characterization results of all samples is provided in Table 6-1.

6.1.2 Methods and animal protocols

Female CD-1 mice [Charles River Laboratories], 25-30 grams, were used for all animal studies. All studies were performed according to protocol # 4281-01 (approval dates: 11/10/11 – 11/09/14), approved by the University of Washington's IACUC. Details of the studies as described in the IACUC protocol are presented in Appendix C.

6.1.2.1 *In vitro* evaluation

Prior to injecting SPIONs in animals, SPIONs were screened for MPI performance *in vitro*. The *m'(H)* of tracers was measured using our MPS in biological environments such as whole blood and RPMI+10% FBS cell culture medium. In order to simulate the effect of physical immobilization in tissues, *m'(H)* of tracers dispersed in a tissue equivalent 1-wt.% agar gel phantom [97] was measured.

6.1.2.2 *In vivo* circulation study

Mice (n = 15) were injected with 100 µl 2.0 gFe/L SPIONs dispersed in 1X PBS through the tail-vein. From each mouse, approximately 100 µl of blood was drawn retro-orbitally at two time points, after which the mouse was euthanized. A total of 5 mice were used for 10 time points and the experiment was repeated a total of 3 times to account for variability; thus, 15 mice were used per formulation. Similar data sets were obtained for the control (n = 15) and Resovist® groups (n = 15), which were administered 100 µl 1x PBS and 2.0 gFe/L Resovist® solution dispersed in 100 µl 1x PBS, respectively. Blood samples were characterized in our 25 kHz MPS (36 mT_{p-p}), while parallel characterization in VSM was performed to compare the static (VSM) and dynamic (MPS) measurements. For SPION quantification, a series of ICP-quantified dilutions were used to calibrate the MPS and VSM signals as a function of concentration. Whole blood samples (100 µl), extracted at various time points after tail-vein injections, were transferred in 0.6 ml Eppendorf tubes and measured directly in the MPS; no processing steps were necessary. The same samples were then transferred to polycarbonate capsules for measurements in the VSM.

6.1.2.3 Biodistribution study

Mice were injected with either 0.5 (n = 3) or 2.0 (n = 3) gFe/L SPIONs through the tail-vein. Control mice (n = 3) were injected with 100 µl 1X PBS. Mice were anesthetized using 5% isoflurane and maintained at 1-2% during the imaging period in the 14-tesla MRI [Bruker Biospin]. Respiration rate was monitored and maintained between 100-150 breaths/min. To acquire reference scans, all mice were imaged before injection. After injection, mice were imaged at 0.5-hour, 1-hour and 24-hour time points. T2-relaxivities (*R2*) of liver, spleen and kidneys were analyzed to quantify nanoparticle uptake. Following the 24-hour time point, mice were euthanized and their organs were harvested, fixed in 10% formalin and embedded in paraffin for histological analysis. Liver, spleen, kidneys, heart, lungs and brain were collected. Tissue sections were stained for iron using Prussian blue.

Note there are fundamental differences between SPION detection using MRI and histology. MRI contrast is due to the superparamagnetic nature of SPIONs; on the other hand, Prussian blue stain identifies the ionic form of iron.

6.1.2.4 Imaging parameters

A 14-tesla (600 MHz) vertical bore Bruker Magnetic Resonance Spectrometer was used for imaging. Bruker's MSME-T2 protocol was used to acquire a T2-map: 12 echo times; TR/TE = 4,000/6.28…12 x 6.28. For iron oxide quantification, the T2-relaxivity as a function of concentration ($r2$ mMFe^{-1} s^{-1}) was measured in 1 wt.% agar gel (Figure 6-2), which is often used as a tissue equivalent phantom material for measuring contrast agent relaxivity [97]. Five concentrations were used for *r2* acquisition: 9.0, 17.9, 44.8, 89.5 and 179.0 µM Fe, including a 1 wt.% agar control. For animal imaging, 25 slices, each 1-mm thick, were imaged using the sequence described above, and analyzed using ImageJ software. T2-relaxation times were calculated using the following equation:

$$I = I_0 \exp\left(-\frac{t}{T}\right)$$

Eq. 6-1

where, *I(t)* is the MRI signal as a function of time, I_o is the initial signal and *T2* (units: s) is the relaxation time required to reach 37% of the original signal (I_o). The T2-relaxivity, *R2* (units: s^{-1}), is the inverse of *T2* and is used to estimate SPION concentration in liver, spleen and kidneys according to the following equation:

$$R2_{SPION} = R2_0 + r2 * C$$

Eq. 6-2

where, $R2_{SPION}$ is the T2-relaxivity after SPION injection, $R2_o$ is T2-relaxivity before SPION injection, *r2* is the T2-relaxivity as a function of concentration (units: $mMFe^{-1}$ s^{-1}) and *C* is SPION concentration (units: mMFe). Thus, from equation (28), SPION concentration *C* is given by $\Delta R2/r2$, where $\Delta R2 = R2_{SPION} - R2_o$.

The relative tissue contrast before and after injections was also used for a qualitative analysis of SPION uptake in liver, spleen and kidneys. For each organ, gray scale intensities from five randomly selected regions of interest (ROI) were measured and averaged. After 24 hours, mice were euthanized, their tissues harvested, and stained for iron using Prussian blue.

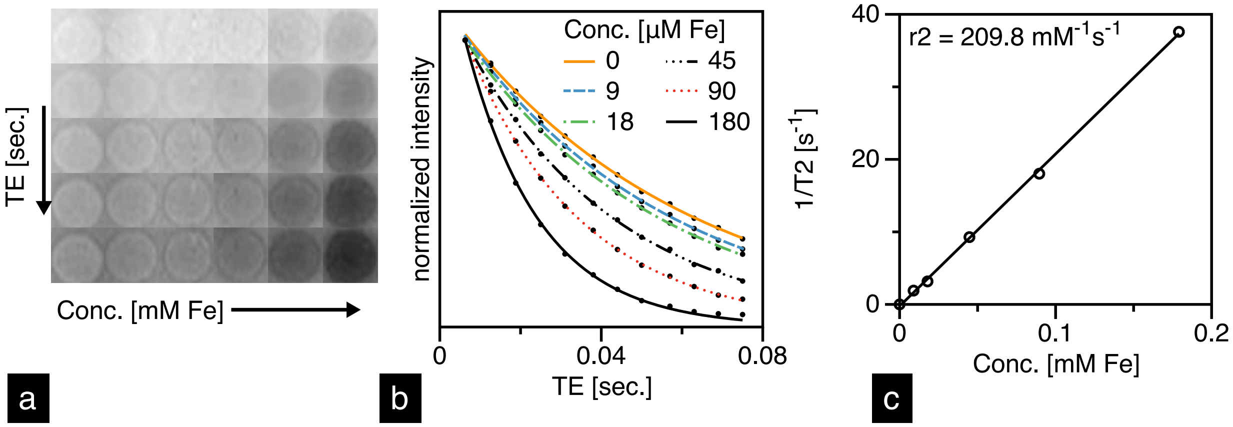

Figure 6-2. (a) T2-weighted images of UW-17-86 SPIONs prepared at 5 concentrations in 1-wt% agar gel and (b) their corresponding intensity-decay profiles fit to Eq. 6-1. (c) Linear fit to T2-relaxivity (1/T2) as a function of SPION concentration; slope of fit is r2 [mM^{-1} s^{-1}]

6.1.3 Results: *in vitro* SPION evaluation

In vitro evaluation of MPS performance proved critical to understanding SPIONs relaxation behavior in biological environments, and thus predicting their *in vivo* MPI performance. There are clear differences in the *m'(H)* of UW-17-86 and Resovist® SPIONs (Figure 6-3) relative to their corresponding *m'(H)*s in DI water. UW-17-86 SPIONs showed no loss in MPS signal when dispersed in either blood or RPMI+10%FBS cell-culture medium, while in 1-wt% agar gel, the signal decreased marginally (~8%). Resovist®, on the other hand, showed an 8% signal loss in blood, and significant loss in cell-culture medium (53%), and 1-wt% agar gel (74%).

Our results indicate that magnetization reversal in UW-17-86 SPIONs is independent of changes in surrounding media, and thus predominantly Néel, whereas Resovist® has a significant contribution from Brownian relaxation.

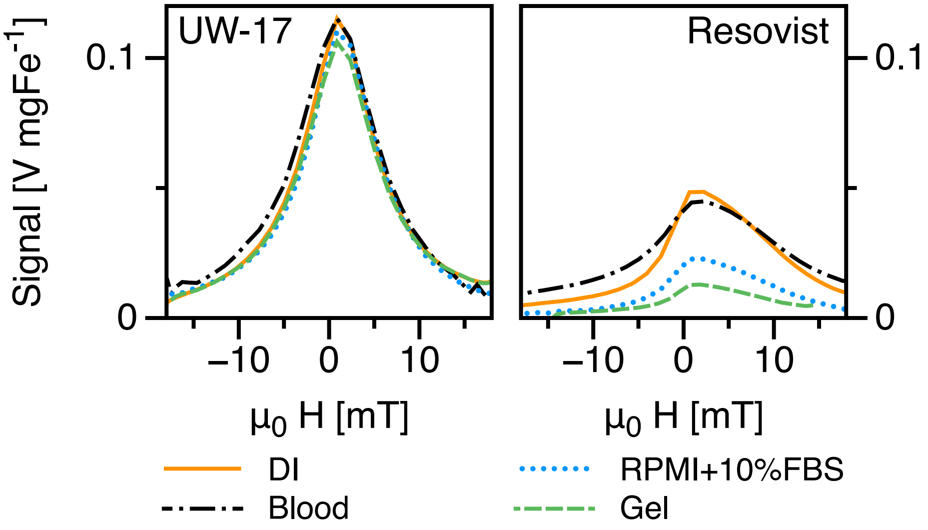

Figure 6-3. *In vitro* MPS characterization of UW-17-86 SPIONs (left) showed nearly no change in *m'(H)* in various biological media unlike Resovist® (right)

6.1.4 Results: *in vivo* circulation study

To test the *in vivo* MPI performance of SPIONs, CD-1 mice were injected with 100 µl-2.0 gFe/L of either UW-17-86 or Resovist® via the tail-vein, and measured the MPS signal from blood samples collected at various time intervals. Calibration curves of UW-17-86 (Figure 6-4) showed that the signal was linear with concentration in both MPS and VSM measurements (Resovist® also shows a linear relationship). Thus, they were used to quantify the raw SPION signal (Figure 6-5.), which was normalized to mouse body weight (in kg) and plotted as a function of time (Figure 6-6). Our results highlight key features that distinguish the *in vivo* performance of MPI-tailored SPIONs (UW-17-86) from traditional MRI-based SPIO contrast agents (Resovist®). First, as UW-17-86 SPIONs are cleared from circulation, the MPS signal, defined by the *m'(H)* peak-height (Figure 6-5(b)), decreases with time; it takes ~5 minutes for the signal to reach half its initial detected value, and nearly 15 minutes to reach the noise floor (Figure 6-6(a)). On the other hand, MPS signal from Resovist® nanoparticles is considerably low and nearly absent past 5 minutes of circulation (Figure 6-6(b)). The increase in signal detected at 5 minutes suggests that the injected bolus takes 0-5 minutes for uniform distribution, and is subsequently cleared from circulation. Second, unlike Resovist®, UW-17-86 shows notable agreement between MPS (f = 25 kHz) and VSM ($f \approx 5.0 \times 10^{-6}$ kHz) measurements. The latter leads us to conclude that the circulating UW-17-86 SPIONs are superparamagnetic, as confirmed in the static VSM measurement, but more importantly, are also suitable for MPI since the MPS signal is detected readily for up to 10 minutes after injection. On the other hand, Resovist® SPIONs detected in VSM are negligibly detected in MPS, suggesting that even though nanoparticles are in circulation, only a fraction of Resovist® SPIONs are MPI-active; indeed, the inventors of MPI hypothesized that only 3% of Resovist® contributes to MPI [1].

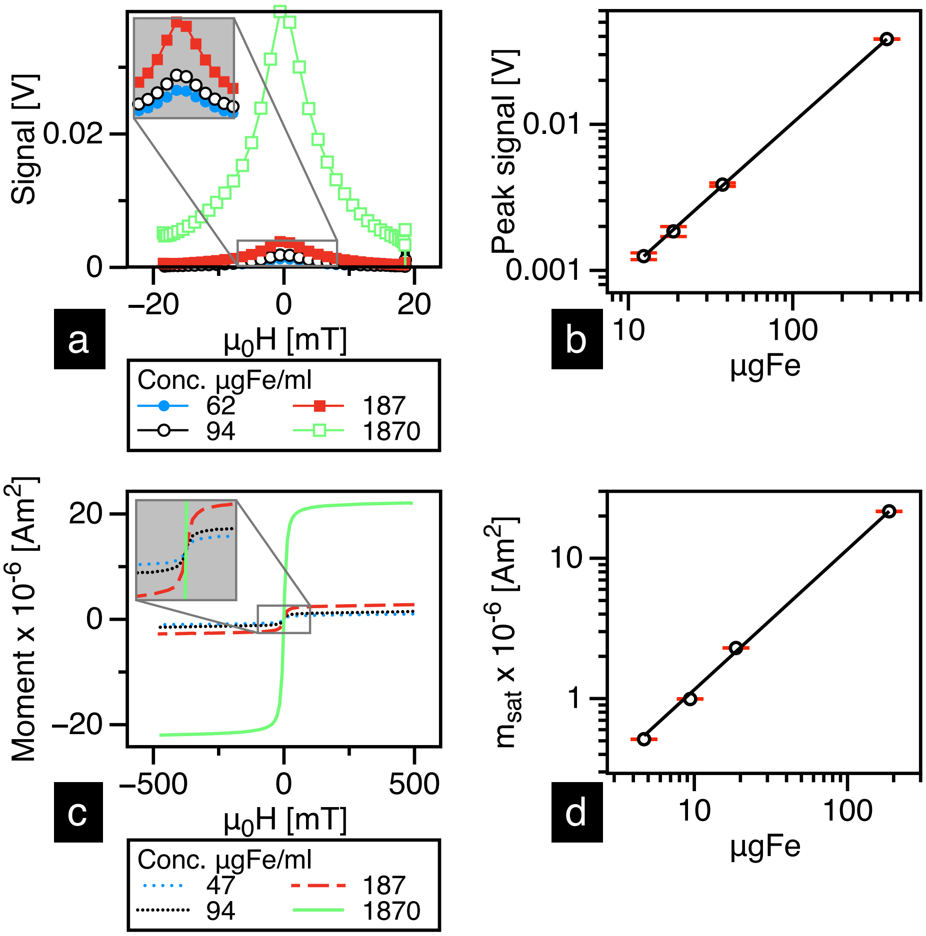

Figure 6-4. The (a) MPS and (c) VSM signals of UW-17-86 SPIONs are linear as a function of concentration, (b) and (d) respectively. For clarity, the MPS signal and magnetization response at low concentrations are magnified and included in insets.

There are several factors that affect circulation time of nanoparticles, including hydrodynamic size, surface coating and charge, and opsonization dynamics (Chapter 3). While it is important that the properties affecting circulation time of SPIONs are optimized, it is also critical that the physical properties optimizing MPI response are preserved. Our *in vitro* study shows that the MPI response of UW-17-86 is predominantly governed by Néel relaxation; thus magnetization reversal is independent of changes in the environment and preserved *in vivo*. Further improvement in circulation time will entail simultaneous optimization of the surface coating and the core. For instance, decreasing hydrodynamic size to 30-40 nm, while maintaining colloidal stability in biological media, will prolong circulation time and enable use of 20 nm (or larger) SPIONs that show excellent MPI performance.

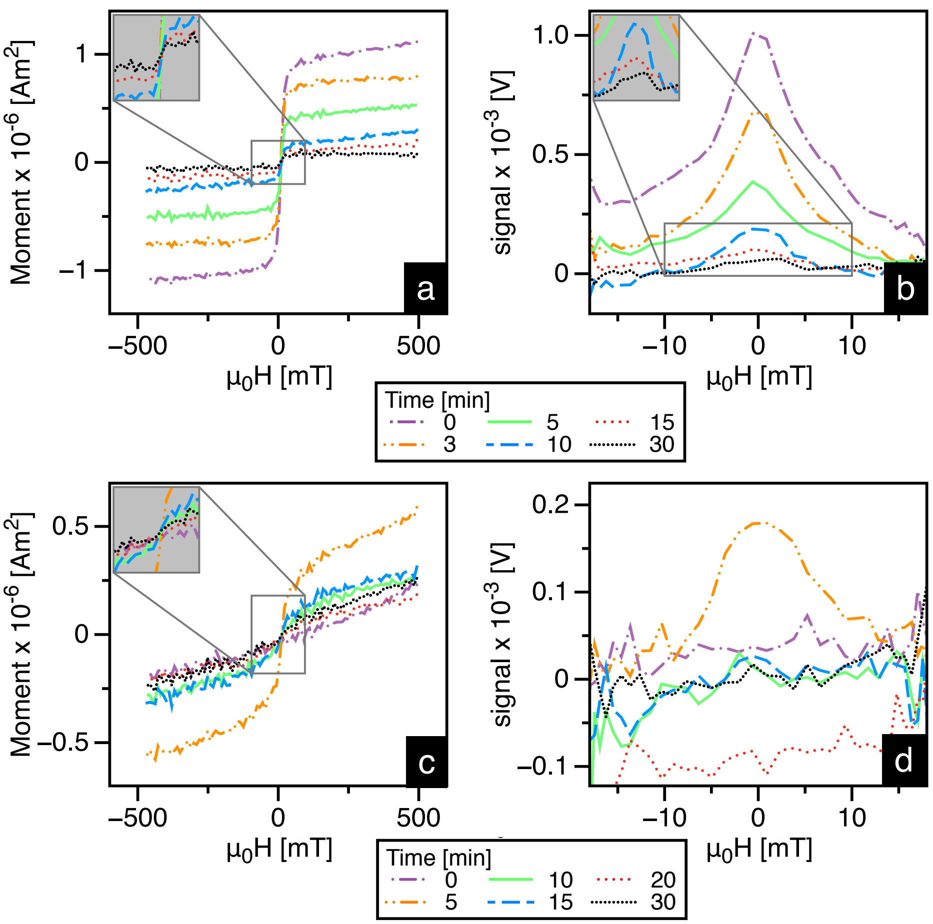

Figure 6-5. VSM and MPS measurements of blood samples drawn retro-orbitally at different time points from mice injected with either UW-17-86 (a & b) or Resovist® (c & d) SPIONs. Compared to the rapid clearance of Resovist® SPIONs, mice injected with UW-17-86 SPIONs showed a gradual decline in signal from both MPS and VSM measurements.

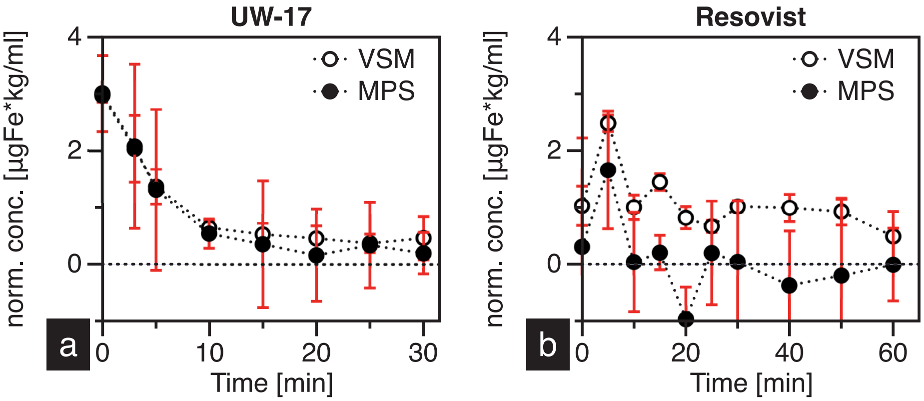

Figure 6-6. (a) UW-17-86 and (b) Resovist® concentration in mouse blood as a function of time. Concentration was determined by comparing the raw VSM and MPS signal with the calibration curves constructed from known SPION standards (e.g. Figure 6-4). Note the excellent correlation between concentrations predicted by MPS and VSM measurements in (a), suggesting the MPS signal from circulating UW-17-86 SPIONs is available for up to 10 minutes; in comparison, Resovist® SPIONs, though circulating, show negligible signal in MPS.

6.1.5 Results: Biodistribution of UW-17-86 SPIONs

SPIONs designed for MPI or MFH are tailored precisely by controlling size to respond optimally to an applied frequency. This biodistribution study in mice provides preliminary biocompatibility and safety assessment of UW-17-86 SPIONs.

For qualitative biodistribution analysis, the relative MRI contrast from axial slices across the abdomen (Figure 6-7 a-c) was used, and the rate of MRI-signal decay (T2-relaxivity) was used for quantitative analysis (Figure 6-7 d & e). It should be noted that the MRI signal from mice dosed at 2.0 gFe/L UW-17-86 was quenched (Figure 6-7 (e)), suggesting a high degree of SPION uptake in the liver. Since the quenched signal is difficult to quantify, an additional group of mice that was administered a 75% lower dose (0.5 gFe/L) was included. At 0.5 hours post-injection, both groups (0.5 gFe/L: Figure 6-7(b), and 2.0 gFe/L: Figure 6-7(c) showed an increase in relative contrast in the liver and spleen, while contrast in kidneys was similar to pre-injection state. At the 24-hour end-point, a substantial signal recovery to pre-injection levels in the 0.5 gFe/L group (Figure 6-7(b)) was observed – suggesting SPION digestion through metabolic pathways in the liver and spleen – while the 2.0gFe/L group showed only marginal recovery (Figure 6-7(c)).

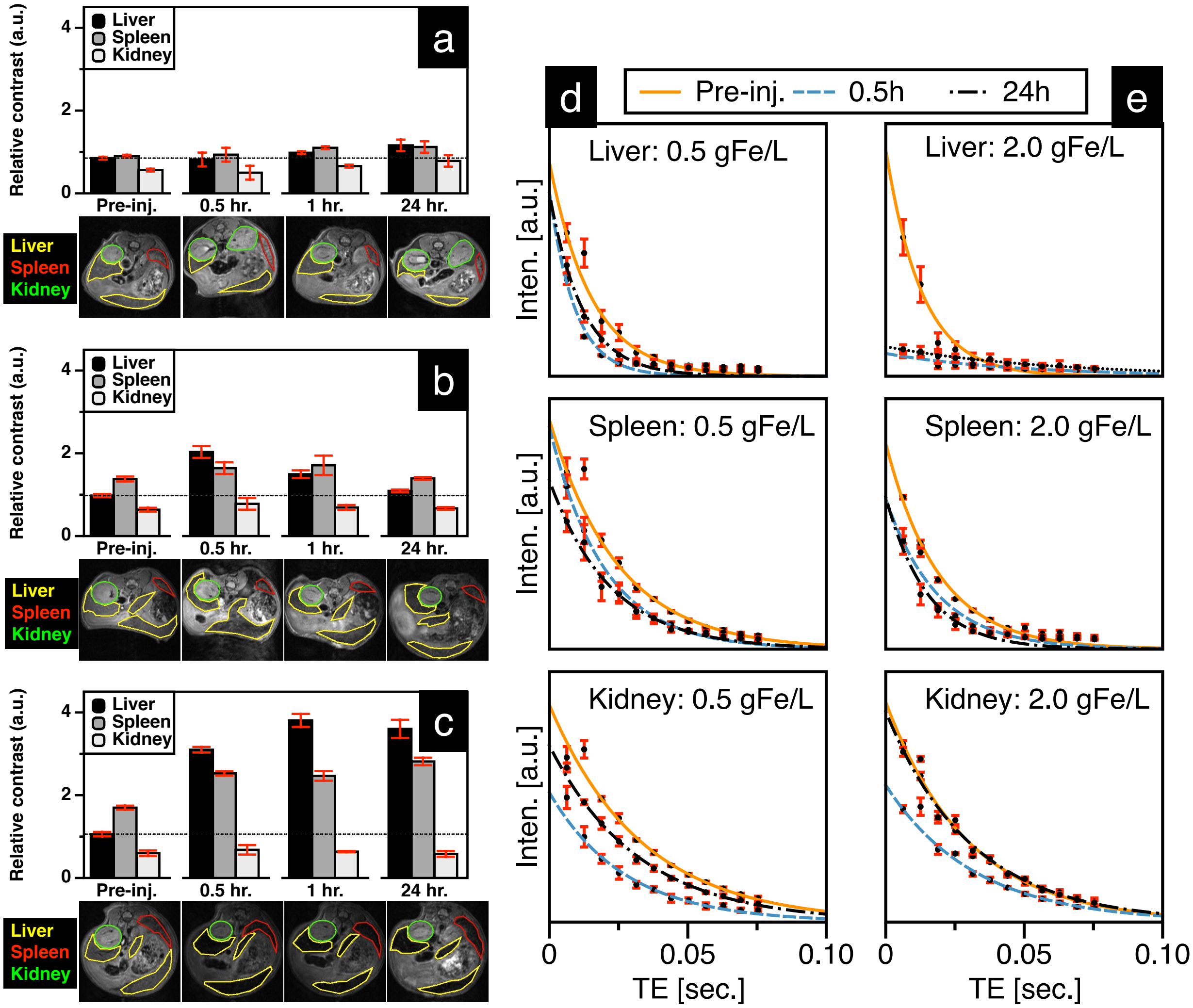

Figure 6-7. Image analysis of mice injected with (a) 1X PBS, (b) 0.5 gFe/L and (c) 2.0 gFe/L UW-17-86 SPIONs; relative contrast in T2-weighted images (TE = 6.28 ms) is the ratio of gray intensity value in ROI relative to the vertebrae in the same slice. (d & e) T2-plots for measuring change in relaxivity (*ΔR2*) were used to quantitatively determine SPION uptake in liver, spleen and kidney.

Quantitative analysis of the 0.5 gFe/L-group supported the qualitative assessment (Table 6-2): from 0.5 to 24 hours, *ΔR2* decreases 58.6% (42.3 s^{-1} to 17.5 s^{-1}) in the liver and 54.8% (10.4 s^{-1} to 4.7 s^{-1}) in the spleen. Kidney *ΔR2*, in comparison, decreases by a significant 84.8% (6.6 s^{-1} to 1.0 s^{-1}) from 0.5 hours to 24 hours. After 0.5 hours post-injection, there was a 21.9% increase (*ΔR2* = 6.6 s^{-1}) in kidney *R2* value, which indicates SPIONs are still circulating. However, the difference in *R2* values ($\Delta R2$ = 1.0 s^{-1}) between pre-injection and 24 hours post-injection is less than the 5% variability in signal measurement, thus negligible. Quantitative analysis of the 2.0 gFe/L group is summarized in Table 6-3; liver signal in the 2.0 gFe/L group was quenched and thus not quantifiable. However, signal in the spleen was quantified and showed an increase in $\Delta R2$ from 0.5 hours to 24 hours post-injection, suggesting continued nanoparticle uptake till the 24-hour endpoint. Histological analysis (Figure 6-8) of tissue sections stained with Prussian blue further confirms MRI analysis – SPIONs accumulate primarily in the liver and spleen. In summary, preliminary safety assessment of our tracers is promising, since biodistribution and clearance routes are analogous to clinically approved SPION contrast agents (Feridex and Resovist®) that are cleared via the RES [98] with no long-term renal involvement.

Table 6-2. Relaxivities of liver, spleen and kidney before and after injection with 100-µl 0.5 gFe/L UW-17-86 SPIONs. Equation 2 was used to estimate SPION concentration

	$R2_0$ [s^{-1}]	$R2_{MNT}$ [s^{-1}]		$\Delta R2 = R2_{MNT} - R2_0$ [s^{-1}]		*C* [uMFe]	
	pre-MNT	t=0.5h	t=24h	t=0.5h	t=24h	t=0.5h	t=24h
Liver	65.9	108.2	83.4	42.3	17.5	201.6	83.4
Kidney	30.1	36.7	31.1	6.6	1	31.5	4.8
Spleen	40.4	50.8	45.1	10.4	4.7	49.6	22.4

Table 6-3. Relaxivities of liver, spleen and kidney before and after injection with 100-µl 2.0 gFe/L UW-17-86 SPIONs.

	$R2_0$ [s^{-1}]	$R2_{MNT}$ [s^{-1}]		$\Delta R2 = R2_{MNT} - R2_0$ [s^{-1}]		*C* [uMFe]	
	pre-MNT	t=0.5h	t=24h	t=0.5h	t=24h	t=0.5h	t=24h
Liver	76.2	-[a]	-[a]	-[a]	-[a]	-[a]	-[a]
Kidney	33.8	31.2	32.3	-2.6	-1.5	-[b]	-[b]
Spleen	52.4	53.8	67.1	1.4	14.7	6.7	69.6

a – T2-fit not possible due to quenched signal (see plot for liver in Figure 8e)
b – $\Delta R2$ values negative

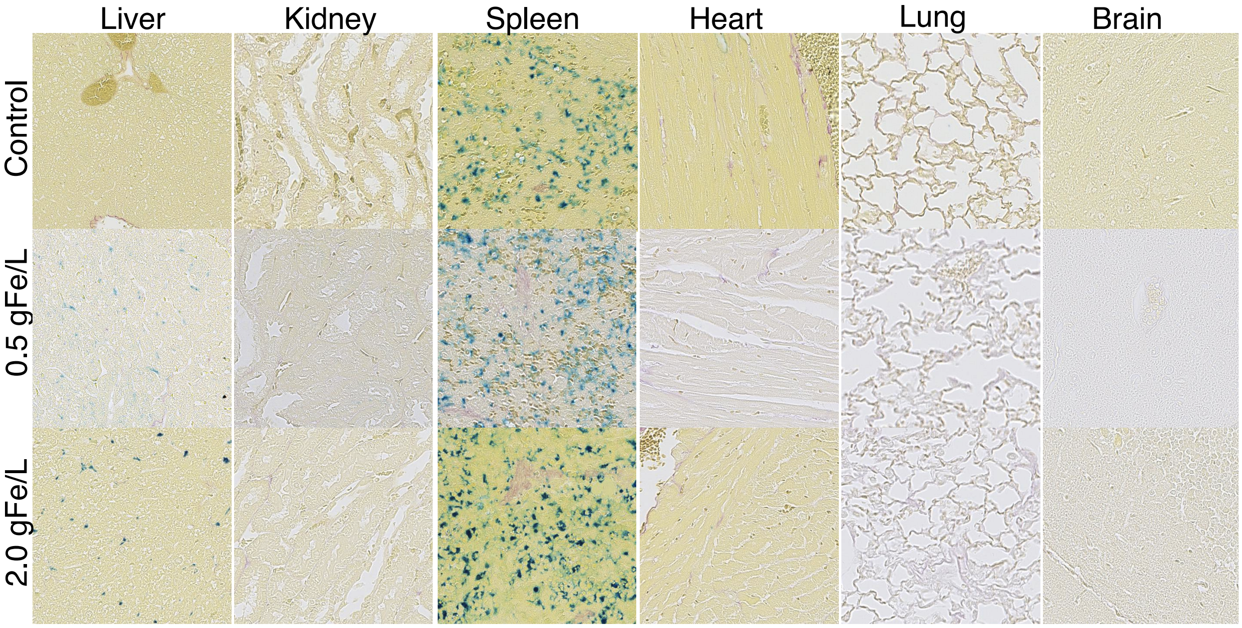

Figure 6-8. Histology images confirmed MRI observation that nanoparticles accumulated primarily in the liver and spleen, with no accumulation in kidneys. Furthermore, tissue analysis of heart, lungs and brain showed no nanoparticle accumulation. Tissue sections collected 24 hours post-injection and stained with Prussian blue (20x magnification). Control group was injected with 1x PBS. Note the naturally high concentration of ferric iron in the spleen control makes qualitative comparison between control and SPION group difficult.

6.2 EFFECT OF HYDRODYNAMIC SIZE ON BIODISTRIBUTION

In this section we will look at the biodistribution of SPIONs as a function of hydrodynamic diameter. The biodistribution results of UW-17-86 SPIONs presented in the previous section are now compared with UW-19-51, which has a 41% smaller hydrodynamic diameter (Table 6-1). Animal and MR-imaging protocols were similar to that described in §6.1.2.3 and 6.1.2.4. In the case of UW-17-86, which has an r2 value half of UW-19-51, MRI signal in the liver was mostly quenched and unusable at the 2.0 gFe/L high dose (Table 6-3); as a result, mice were only administered the low dose (0.5 gFe/L in 100 µl 1x PBS) in the case of UW-19-51. However, due to the high r2 value, the low dose also quenched the signal and made quantification difficult; thus, only a qualitative image comparison with UW-17-86 was possible (Figure 6-9). Immediately, the effect of UW-19-51's large r2 is evident from the high relative contrast observed in the liver – since this is only a qualitative comparison, the higher contrast should *not* be attributed to a greater quantity of SPION uptake. Furthermore, UW-19-51 shows almost no renal involvement similar to UW-17-86. Unlike UW-17-86, however, UW-19-51 does show a gradual increase in liver contrast from 0.5 hour to 1 hour time points, which suggests a potentially longer circulation time. More importantly, relative to UW-17-86, the differences in contrast between liver and spleen are substantial in the case of UW-19-51; critically, UW-19-51 shows significantly low contrast in the spleen. It is possible that the smaller hydrodynamic diameter of UW-19-51 increases the probability of SPIONs escaping through the spleen's interendothelial slits (see Chapter 3 and Figure 3-1) and minimizes their phagocytic uptake by spleen macrophages present in the red pulp [62]. Furthermore, the liver contrast does not show a complete return to pre-injection contrast levels like UW-17-86; as a result, mice were monitored for a week (Figure 6-10). During the 7-day monitoring period, MRI signal in the liver gradually declined, suggesting some of the SPIONs potentially cleared from the liver; however, signal still did not reach pre-injection levels potentially because of conversion and storage of excess iron in the ferritin protein. Elevated levels of ferritin in the liver is known to impact liver contrast [99].

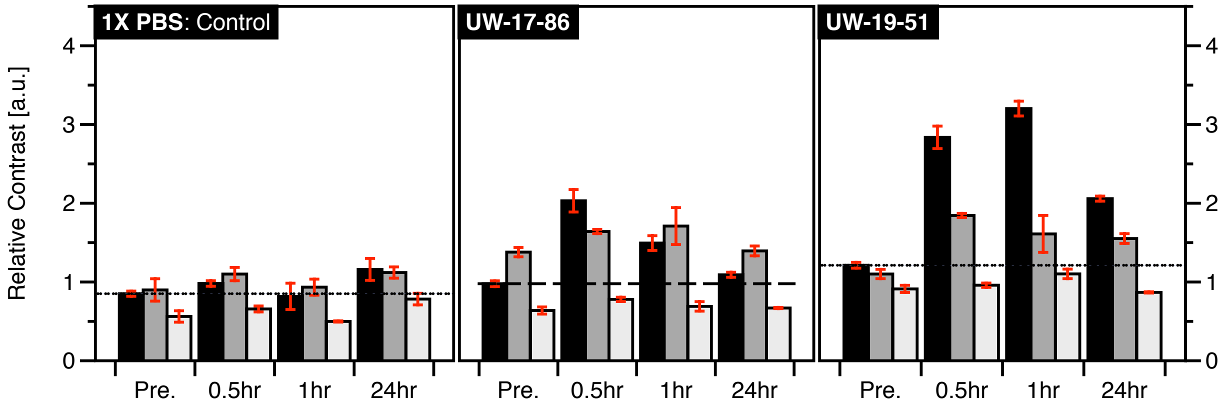

Figure 6-9. Image analysis of mice injected with 1X PBS, 0.5 gFe/L of UW-17-86 and 0.5 gFe/L of UW-19-51; relative contrast in T2-weighted images (TE = 6.28 ms) is the ratio of gray intensity value in ROI relative to the vertebrae in the same slice.

After 7 days of MRI monitoring, mice were euthanized and tissue sections from the liver, spleen, kidneys, heart, lungs and brain were stained for iron with the Prussian blue stain (Figure 6-11). Compared to the 24 hour post-histology analysis of mice injected with 0.5 gFe/L UW-17-86 (Figure 6-8), both the liver and spleen show visually low amounts of iron 7 days post-injection with 0.5 gFe/L UW-19-51. Needless to say, the end-points of the two experiments are 6 days apart, and it is possible that UW-17-86 SPIONs would also show some clearance given longer time. Nevertheless, the decrease in MRI image contrast with time observed in Figure 6-9 and Figure 6-10 suggest that both UW-17-86 and UW-19-51 show some clearance of SPIONs from the liver.

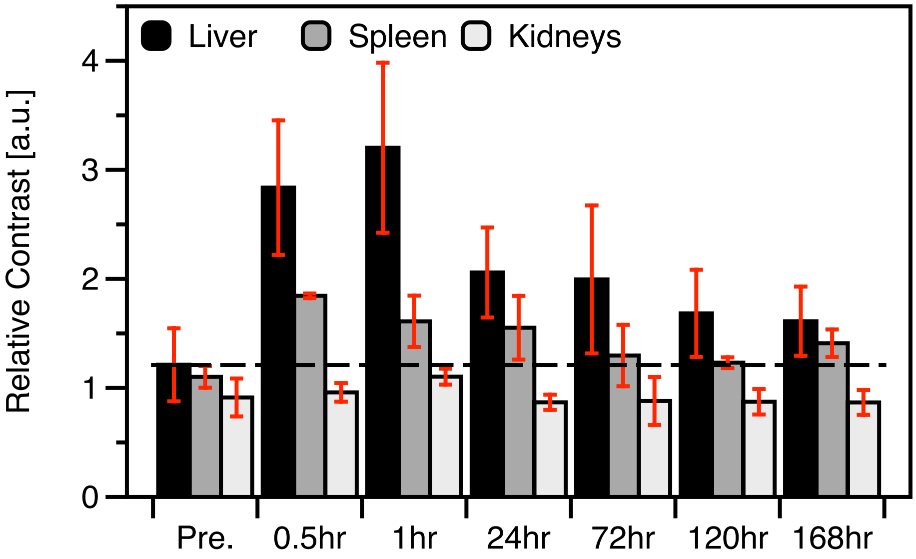

Figure 6-10. Biodistribution of UW-19-51 in mice monitored over a period of 7 days using MRI

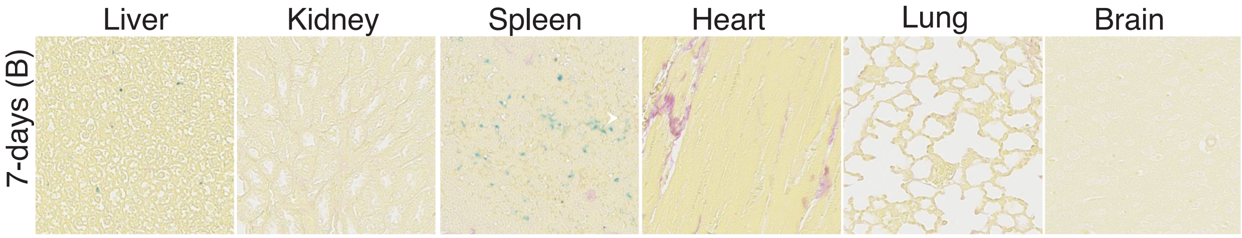

Figure 6-11. Histology analysis of a mouse euthanized 7-days post-injection with UW-19-51. The tissue sections were stained with Prussian blue stain.

6.3 EFFECT OF HYDRODYNAMIC SIZE ON CIRCULATION TIME

After evaluating the effects of hydrodynamic size on biodistribution in the previous section, we now turn our attention to the impact it has on blood circulation time – a critical performance evaluation parameter for applications of SPIONs in MPI-based vascular imaging or disease site-specific MFH therapy. In this study, the blood circulation time of UW-17-86, presented earlier in §6.1.4, is compared with UW-20-42, which has ~50% smaller hyrdoydnamic diameter. Animal protocols were similar to those discussed in §6.1.2.2. Mice (n = 12) were weighed before injection and as in the case of UW-17-86, administered 2.0 gFe/L UW-20-42 dispersed in 100 µl sterile 1x PBS solvent.

Raw MPS signal from blood samples collected at various time points and the calibration curve for UW-20-42 is shown in Figure 6-12. Results of the circulation study and comparison with UW-17-86 are shown in Figure 6-13 below. SPIONs appear to clear according to the one-compartment pharmacokinetic model, which treats the body as a single homogenous compartment. According to this model, clearance happens exponentially with a single clearance rate constant:

$$I = I_0 \exp(-R * t)$$

Eq. 6-3

where, I is the SPION concentration at any given time t, I_o is the initial concentration and R is the clearance rate constant. After fitting the data, which is presented as % initial concentration (I/I_o x 100%) vs. time, the blood half-life was determined – blood half-life is the time it takes for the concentration to reach 50% initial concentration, which is indicated by the dashed horizontal line in Figure 6-13.

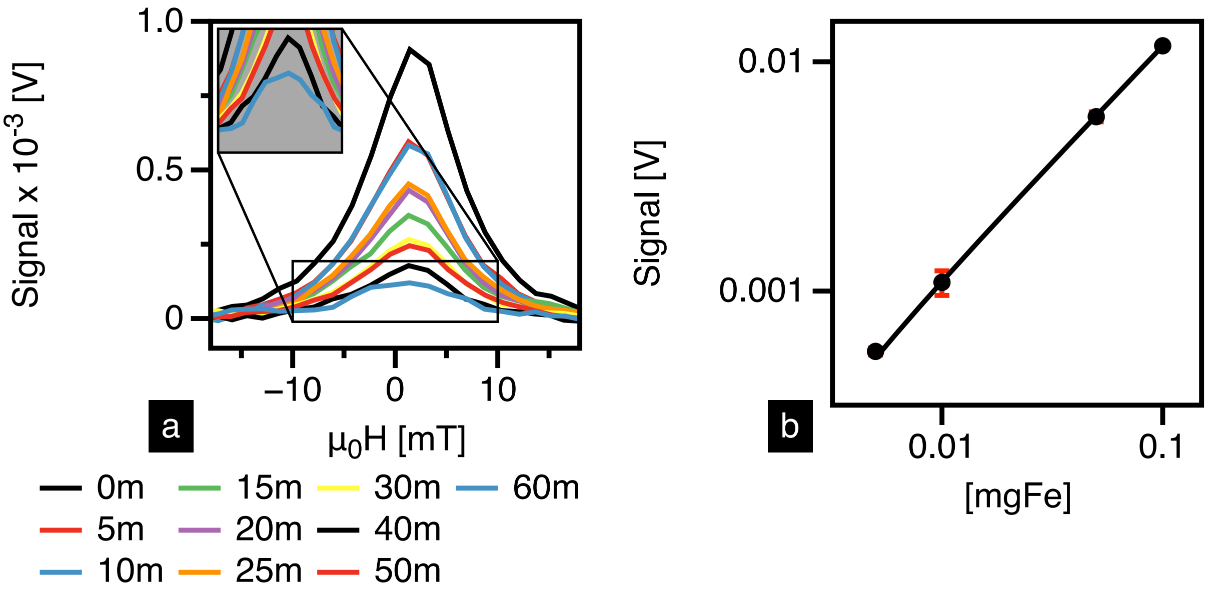

Figure 6-12. (a) Raw MPS data from blood samples collected at various time points. Mice were injected with 100 μl 2.0 gFe/L UW-20-42 SPIONs. (b) MPS calibration curve for UW-20-42.

The results below clearly show that UW-20-42 has a longer circulation time than UW-17-86; specifically, the blood half-life of UW-20-42 was ~18 minutes compared to ~4 minutes for UW-17-86. Since the core properties of the two samples are very similar (Table 6-1), it is likely the differences in circulation characteristics are due to the differences in surface coating and hydrodynamic diameter. Our results seem to agree with the general notion that blood half-life tends to increase with a decrease in hydrodynamic size (§3.1).

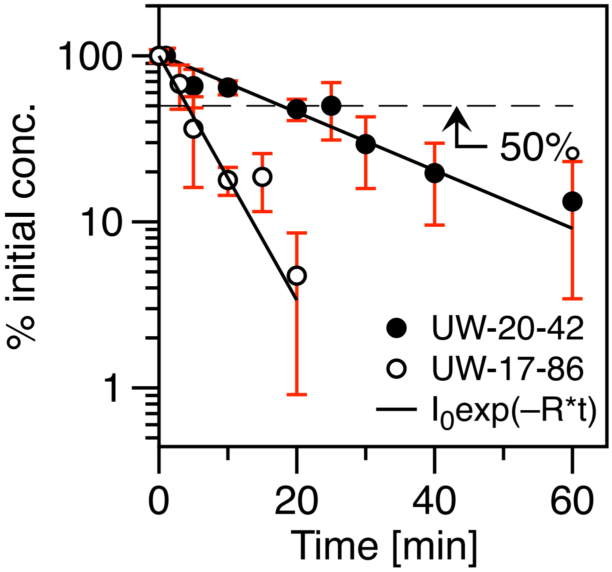

Figure 6-13. Blood circulation study shows that SPIONs clear according to the one-compartment pharmacokinetic model. The blood half-life of UW-20-42 SPIONs was 18 minutes, ~4.5x longer than UW-17-86, which also had twice the hydrodynamic diameter compared to UW-20-42.

6.3.1 One month clearance study of UW-20-42

In addition to circulation time, the clearance of UW-20-42 SPIONs was studied over a 1 month time period. Mice were administered the low dose – 0.5 gFe/L – due to the high r2 value of UW-20-42 (Table 6-1). During the 1-month time period, the mice were routinely monitored and did not show any overt signs of discomfort or deviation from normal social and eating behavior; on average (n = 3), mice gained approximately 4-8% of their original body weight after the first week of SPION injections. MRI contrast data averaged from 3 mice is presented in Figure 6-14; tissue histology data is also included.

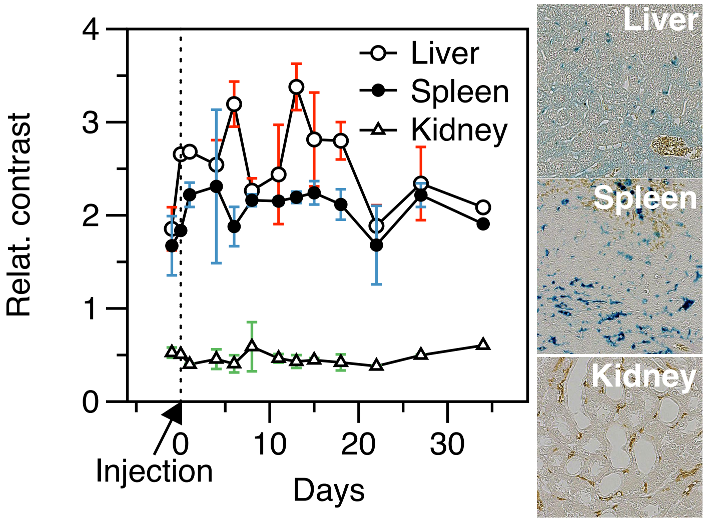

Figure 6-14. MRI contrast data from liver, spleen and kidneys of mice administered UW-20-42 and monitored for a period of 1 month. Images from tissue histology slides are also included on the left.

The 1-month clearance study of UW-20-42 SPIONs reveals interesting results that were not seen previously in the shorter-term studies discussed earlier. The MRI signal in the liver and spleen continued to increase approximately 7 days into the study, after which the signal in the liver dropped significantly; signal in the spleen stayed relatively flat during this period. After approximately 11 days, the liver signal spiked again and then gradually started to decline with time. The signal in the spleen follows the same trend as the liver after ~15 days. Meanwhile, signal in the kidney always remains close to the pre-injection levels, suggesting renal involvement is minimal, similar to the observations with UW-17-86 an UW-19-51 samples. Prussian blue stained tissue sections show a large amount of iron present in the liver and spleen, while the kidney is mostly free of iron.

The transient drop in signal 7 days after administration is yet not understood and further investigation is recommended. However, we can still hypothesize based on existing understanding about the iron metabolic cycle [100-102] and previous studies on SPION pharmacokinetics [103,104]. In the body, iron is stored in several forms; majority of it is stored in the hemoglobin protein, where it plays the crucial role of delivering oxygen and removing carbon dioxide from cells. Transferrins (Tfs) are a series of Fe-binding proteins that regulate the amount of free iron in circulation. One of them is serum-Tf – found in the serum, it circulates to deliver wherever needed. Finally, ferritin is also an iron-binding protein that stores iron in the ferrihydrite form [102]; it is found primarily in liver parenchymal cells and is antiferromagnetic [99]. Our results, including several studies on iron oxide biodistribution and clearance, have shown that SPIONs accumulate mostly in the liver, most likely by the Kupffer cells lining the sinusoidal capillary walls. Kupffer cells are mainly responsible for recycling iron from senescent erythrocytes and returning it back to one of the iron-binding proteins mentioned above. It is highly likely that iron captured from metabolized SPIONs is similarly incorporated in one of the proteins. In fact, ferritin can store upto 4,500 iron atoms in its cage-like structure. It is possible that this protein is overexpressed in the liver due to the presence of excess iron after breakdown of SPIONs in the Kupffer cells, and in large amounts, ferritin is known to affect the T2-relaxivity of the liver for long periods of time as observed in our results [99]. Further investigation on the exact metabolic pathway of SPIONs should be done using radiolabeling techniques [98,105]. Independent labeling of the core and shell should provide the ability to trace the two components as they are cleared or metabolized in the body.

6.4 SUMMARY OF *IN VIVO* RESULTS

Monodisperse SPIONs synthesized in non-aqueous solvents and subsequently transferred to aqueous phase using PMAO-PEG were administered in mice to study their biodistribution and pharmacokinetics. UW-17-86 SPIONs showed 2-fold greater signal per unit mass and 20% better spatial resolution than Resovist® in our 25 kHz MPS. In the first set of experiments, i*n vitro* evaluation showed that the MPI response of UW-17-86 SPIONs, unlike Resovist®, was independent of changes in hydrodynamic size and the carrier fluid's viscosity – a critical feature that ensures relaxation will be preserved in the physiological environment. Furthermore, i*n vivo* circulation time of UW-17-86 in mice, as measured in our MPS (f = 25 kHz), was 3x longer than Resovist® and showed excellent agreement with the corresponding static (VSM: t_m = 100s) measurement. The latter confirmed that the UW-17-86 SPIONs still in circulation are MPI-capable *in vivo*, while Resovist® SPIONs though circulating, are unsuitable for MPI. The biodistribution of UW-17-86 SPIONs in mice was similar to clinically approved SPIO agents, primarily distributing in the liver and spleen.

Furthermore, biodistribution study of UW-17-86 SPIONs was compared with UW-19-51, which has a similar coating but smaller hydrodynamic diameter due to the exclusion of SPION clusters. Both formulations showed minimal accumulation in the kidneys, which demonstrates their potential safety for CKD patients (§1.1) and a potential pathway for clearance or breakdown of the iron oxide nanoparticles in the liver. On the other hand, comparison of blood circulation time with UW-20-42 showed that a smaller hydrodynamic size resulted in a prolonged blood half-life; specifically, UW-20-42 had a half-life of 18 minutes, which was 4.5x longer than UW-17-86.

Chapter 7.

CONCLUSIONS

Optimizing MPI and MFH performance of SPIONs for their respective radiofrequency ac-field conditions (MPI: 25 kHz; $40\ \mathrm{mT}_{p\text{-}p}\mu_o^{-1}$ and MFH: 375 kHz; $17\ \mathrm{mT}_{p\text{-}p}\mu_o^{-1}$) imposes strict constraints on their magnetic relaxation properties, which must be tailored with precise control of SPION size and size distribution. Unfortunately, existing SPIONs designed for MRI contrast lack such tailored properties, and a new class of SPIONs with precisely tuned properties and systematically characterized physiological responses are required. Previous work in our group, conducted in optimizing SPIONs for MPI (R. M. Ferguson, "Tracer design for Magnetic Particle Imaging: modeling, synthesis, and experimental optimization of biocompatible iron oxide nanoparticles", PhD thesis, 2011) and MFH (M. Gonzales-Weyhmiller, "Synthesis, modeling and optimization of iron oxide nanoparticles for magnetic fluid hyperthermia", PhD thesis 2007) has focused on tuning the magnetic core properties of SPIONs by controlling their size and size distribution. In this thesis, the focus was on translating the optimized performance of SPIONs to physiological environments and demonstrating *in vivo* biocompatibility; as a result, the core and shell properties were tailored in concert. Since the SPION shell bridges this translational gap, particular emphasis was given to optimizing and characterizing the surface coating of SPIONs and the process of transferring SPIONs to the aqueous phase. The key results of this work, and the resulting publications are summarized below:

1. Hydrophobic SPIONs synthesized from the thermal decomposition of Fe^{3+}-oleate were transferred to the aqueous phase using a PEGylated poly(maleic anhydride-alt-1-octadecen) (PMAO) amphiphilic polymer. The hydrodynamic diameter of SPIONs, measured using dynamic light scattering, was between 40-60 nm, and the nonionic methoxy-poly(ethylene glycol) (m-PEG; M_w = 5,000 Da or 20,000 Da) polymer re-

sulted in a neutral surface charge, suggesting steric stabilization of SPIONs (Figure 4-8). Furthermore, it was found from DLS data that increasing PEG density from a PEG/PMAO of 20 to 30 inhibited protein adsorption and improved colloidal stability of SPIONs in serum-rich cell culture medium (Figure 4-9(a) and (b)). However, the density of PEG did not suggest any major differences in macrophage uptake, rather SPIONs coated with both variations of PEG showed significantly lower uptake than carboxy-dextran coated Resovist® (Figure 4-10). Increasing the PEG molecular weight from 5,000 Da to 20,000 Da was also tested, though still in early stages, the 20,000 Da PEGylated PMAO is promising, showing improved colloidal stability of bigger SPIONs (~25-27 nm) in serum-rich cell culture medium. Finally, cytotoxicity study in Jurkat cells (Figure 4-11) showed that PMAO-PEG coated SPIONs (PEG/PMAO = 20) in general exhibit low toxicity (~15% from LDH release assay) and reduced the cell metabolic activity by ~25% (from luciferase assay).

Publications:

AP Khandhar, RM Ferguson, JA Simon, KM Krishnan, "Tailored magnetic nanoparticles for optimizing magnetic fluid hyperthermia", *J. Biomed. Mater. Res.*, 100A:728-37 (2011)

2. For MPI, phase transfer using a suitable density of PEG was found to be critical in demonstrating optimal particle response function (*m'(H)*) in serum-rich media. Hydrodynamic diameter measurements in DLS (Figure 4-9) and *m'(H)* measurements in the 25 kHz magnetic particle spectrometer (MPS) (Figure 5-4) combined to show that either increasing the PEG density from PEG/PMAO of 20 to 30, or increasing the PEG molecular weight from 5,000 to 20,000 Da prevented (1) protein adsorption on SPION surface – necessary for demonstrating long-circulation times – and

preserved (2) the optimum relaxation properties of large core diameter SPIONs for MPI applications.

Publications:

RM Ferguson, **AP Khandhar**, KM Krishnan, "Tracer design for magnetic particle imaging (invited)", *J. Appl. Phys.*, 111(7):07B318 (2012)

AP Khandhar, RM Ferguson, H Arami, KM Krishnan, "Physical and biological optimization of core-shell nanoparticle tracers for *in vivo* MPI", *2013 International Workshop on Magnetic Particle Imaging (IWMPI)*, doi: 10.1109/IWMPI.2013.6528377

3. Using our 25 nm (core dia.) MPI-optimized SPIONs, we performed phantom imaging in independently developed MPI scanners at Philips Medical Imaging (Hamburg, Germany) and University of California, Berkeley (Prof. Steven Conolly group). These first images showed that UW's size-tuned SPIONs produced 3x brighter images than Resovist® independent of the imaging system. Furthermore, a point-source measurement in the UCB scanner operating at 7 $T\mu_0^{-1}m^{-1}$ field gradient showed an imaging resolution of 2.9 mm from UW SPIONs compared to 3.9 mm from Resovist®. Our preliminary results in collaboration with MPI hardware developers establishes a benchmark in MPI imaging; however, further improvement in imaging resolution will be required if MPI is to compete on the clinical platform – the current approach of coordinating SPION tracer development with MPI hardware development is a key step towards achieving these goals.

Publications:

RM Ferguson, **AP Khandhar**, E Saritas, L Croft et al, “Magnetic Particle Imaging with Safe, Tailored Iron Oxide Nanoparticle Tracers”, *IEEE T Med Imaging*, in press.

4. In MFH studies, systematic evaluation of SPIONs at 375 kHz (17 $\mathrm{mT}_{p\text{-}p}\mu_o^{-1}$) in a commercial hyperthermia system showed that SLP of monodisperse SPIONs after removing clustered SPIONs increased with size according to the Stoner-Wohlfarth model for predicting power losses (Figure 5-7). Furthermore, extracellular heating in Jurkat cells with 16 nm SPIONs demonstrated a significant decrease in cell viability (Figure 5-9). In contrast, the efficacy of intracellular heating was not clear due to the preliminary nature of the experiments.

Publications:

AP Khandhar, RM Ferguson, JA Simon, KM Krishnan, “Enhancing cancer therapeutics using size-optimized magnetic fluid hyperthermia”, *J. Appl. Phys.*, 111(7):07B306 (2012)

AP Khandhar, RM Ferguson, KM Krishnan, “Monodispersed magnetite nanoparticles optimized for magnetic fluid hyperthermia: Implications in biological systems”, *J. Appl. Phys.*, 109:07B310 (2011)

5. Biodistribution in mice from MRI analysis showed that SPIONs accumulated primarily in the liver, and to some extent in the spleen (Figure 6-10). Prussian blue stains of tissue sections confirmed liver accumulation. However, large amounts of iron in the control spleen (injected with 1x PBS) made it difficult to differentiate between SPIONs and pre-existing iron (Figure 6-8). Critically, MRI data suggested that

SPIONs showed some clearance or breakdown pathway, mostly in the liver, with some contribution from the spleen. A one-month clearance study also indicated some long-term iron retention in the liver, but the nature of the iron – whether iron oxide or stored in ferritin compartments – was unclear and needs further investigation.

6. Blood circulation studies in mice showed that PMAO-PEG coated SPIONs in general circulated substantially longer than carboxy-dextran coated Resovist® SPIONs. Furthermore, excellent correlation between static (VSM) and dynamic (MPS) measurements confirms that the circulating PEG-coated SPIONs are indeed suitable for MPI. Finally, SPIONs with 42 nm hydrodynamic diameter showed 4.5x longer blood half-life than 86 nm SPIONs, consistent with the general understanding that reducing hydrodynamic size prolongs circulation time.

Publications for (5) and (6):

AP Khandhar, RM Ferguson, H Arami, KM Krishnan, "Monodisperse magnetite nanoparticle tracers for *in vivo* magnetic particle imaging", *Biomaterials*, 34(15):3837-45 (2013)

RM Ferguson, **AP Khandhar**, H Arami, L Hua, et al, "Tailoring the magnetic and pharmacokinetic properties of iron oxide magnetic particle imaging tracers", *Biomed. Tech.*, 19:1-15 (2013)

The key results and conclusions of this thesis summarized above highlight the importance of tailoring the core and shell properties of nanoparticles in concert; critically, because the superparamagnetic core is responsible for the physical properties needed in MPI and MFH, and the polymer shell is responsible for ensuring the core properties are preserved in physiological environments, the two are intimately coupled. In order to accomplish clinical translation of promising technologies like MPI and MFH, progress in both hardware and SPION design is necessary. Here, we have demonstrated an approach to optimizing SPIONs by using *in vivo* mouse models to provide critical feedback on SPION performance. In the process, we have already developed a prototype SPION formulation that offers sufficient blood half-life and sustained MPI signal for future applications in real-time cardiovascular imaging.

7.1 FUTURE WORK

In this thesis, a lot of emphasis was put on optimizing the surface coatings of SPIONs to preserve the fundamental properties of the core responsible for optimum MPI and MFH performance. The surface coatings were primarily designed to protect the iron oxide cores from the physiological environment; as a result, prolong the circulation time of SPIONs for future applications involving vascular imaging and passive targeting of tumors for site-specific therapy – passive targeting refers to the accumulation of SPIONs in the affected site due to the EPR effect [59], and without any active targeting or binding mechanism. The next step is to find ways to functionalize the surface coatings so as to attach targeting moieties that enable active targeting of disease sites. Targeted SPIONs will also enable disease diagnosis at a molecular level – further work on designing SPIONs for specific clinical indications should be done.

Secondly, the SPIONs designed in this thesis are already capable of bimodal imaging using MRI and, in the future, MPI imaging scanners. SPIONs with multimodal imaging capabilities will offer clinicians a dynamic diagnostic tool and should be further researched.

Finally, from a safety perspective, more information on the *in vivo* toxicity and metabolism of SPIONs is required. Radiolabeling of SPIONs with radioisotopes of iron (e.g. Fe^{59}) should enable researchers to chase the iron specifically linked to the SPIONs and determine the eventual fate of SPIONs. Similar studies should be done on the surface coating materials as well.

APPENDICES

A. Synthesis of magnetite nanoparticles

A.1 Fe^{3+}-oleate precursor synthesis

Magnetite SPIONs were synthesized according to a procedure based on the pyrolysis of the Fe^{3+}-oleate metal fatty acid salt in high boiling point organic solvents. The Fe^{3+}-oleate precursor was prepared according to published methods [106,107]. In a typical reaction, 3.23 g (20 mmol) of anhydrous $FeCl_3$ (Alfa Aesar) and 17.3 g of oleic acid (90% tech. grade; Alfa Aesar) were dissolved in 100 ml of anhydrous methanol. A sodium hydrodxide solution (2.4 g of NaOH dissolved in 200 ml methanol) was added drop wise to the iron chloride + oleic acid solution. The solution was constantly stirred to ensure uniform mixing of the NaOH solution. After approximately 2 hours of stirring, a brown sticky precipitate was formed. After decanting the solvent, the precipitate was washed 5 times in methanol and subsequently dried under a steady flow of argon gas. Next, the dry precipitate was dissolved in ~30 ml hexane and washed 4x with DI water (~300 ml) in a 500 ml separatory funnel. After vigorous mixing, the emulsion was allowed to separate before removing the bottom water layer. Finally, the hexane was removed in a rotary evaporator and the washed Fe^{3+}-oleate was dissolved in 1-octadecene (ODE, technical grade 90%) to obtain the precursor stock solution, which was protected from light with aluminum foil and stored at 4°C. The final concentration was typically set to 18 wt%.

A.2 Synthesis of hydrophobic oleic acid coated Fe_3O_4 nanoparticles

Synthesis of Fe_3O_4 was based on the La Mer model for synthesizing monodisperse nanoparticles. It was accomplished by the thermal decomposition of Fe^{3+}-oleate precursor in the presence of excess oleic acid surfactant; critically, varying the precursor to oleic acid ratio allowed precise and repeatable control over SPION size from 10 to approximately 22 nm (core diameter). For instance, synthesis of 15 nm particles required 0.2 mmol/g of Fe^{3+}-oleate and 3 mmol/g of oleic acid in 2.5 g of reaction solvent (ODE). The mixture was refluxed overnight (24 h) at 320°C under an argon blanket and vigorous stirring. Nucleation of nanoparticles was observed as a sudden change in color, from clear to black and the time for nucleation usually varied linearly with the surfactant to precursor ratio as shown in Figure A.1. Furthermore, increasing the initial Fe-oleate precursor concentration from 0.5 mM to 1.0 mM delayed the time for nucleation for the same oleic acid/Fe-oleate ratio, suggesting that scaling up of the reaction will require calibration of the synthesis to ensure repeatable SPION synthesis. The final product was collected and washed to remove excess surfactant and solvent. SPIONs were washed 5-6 times with a mixture of chloroform and methanol (1:1 by volume), and separated using a magnet. Vacuum dried SPION powder was coated with oleic acid and could be easily dispersed in organic solvents such as toluene or chloroform. Synthesis of iron oxide nanoparticles in the 23-27 nm (core dia.) range, which is also the optimal size range for MPI at 25 kHz, reproducibility of the synthesis was found to be low; thus, further research on their nucleation and growth kinetics is currently underway.

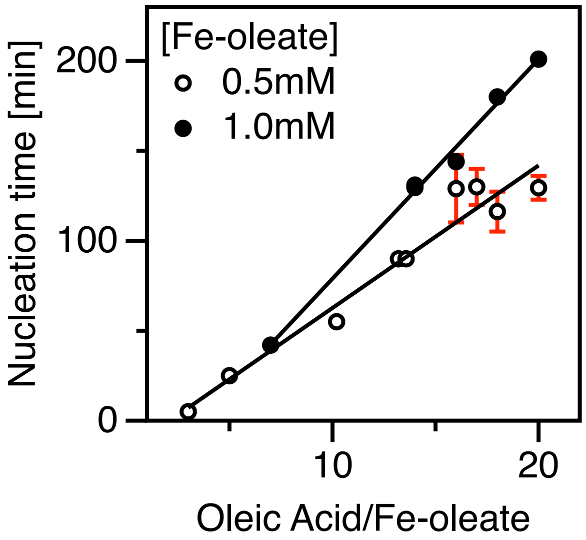

Figure A.1. Nucleation time shows a linear relationship with oleic acid/Fe-oleate ratio. Furthermore, the initial concentration of the precursor also affects the nucleation time.

B. Core and hydrodynamic size characterization

Since the choice in magnetic nanomaterials for medical applications is restricted to the iron oxides (maghemite or magnetite), tailoring the size and size distribution of SPIONs is the quintessential approach to optimizing their performance for MPI and MFH applications. Hence, size characterization is a basic requirement for evaluating SPION performance.

B.1 Size measurements using VSM

The magnetic core diameter of SPIONs is determined from fitting the Langevin function (Eq. 2-8) to the magnetization curve. Since a typical nanoparticle ensemble consists of a distribution of sizes, the overall magnetization response is a weighted average of the particle size distribution (Eq. 2-23). While bigger particles in the ensemble dictate the initial susceptibility (χ_o), smaller particles dictate the degree of magnetic saturation ($m_s = \varepsilon M_s$) achieved in the SPION dispersion, where M_s is the bulk saturation value and ε is the volumetric packing fraction. Both χ_o and m_s are determined from the magnetization curve measured in a VSM as shown in Figure B.1, which is an experimentally measured magnetization curve. The slope of the linear region (left) is χ_o, and the y-intercept from the linear fit of m vs. $1/\mu_o H$ (right) gives m_s – the average of the positive and negative saturation values is used.

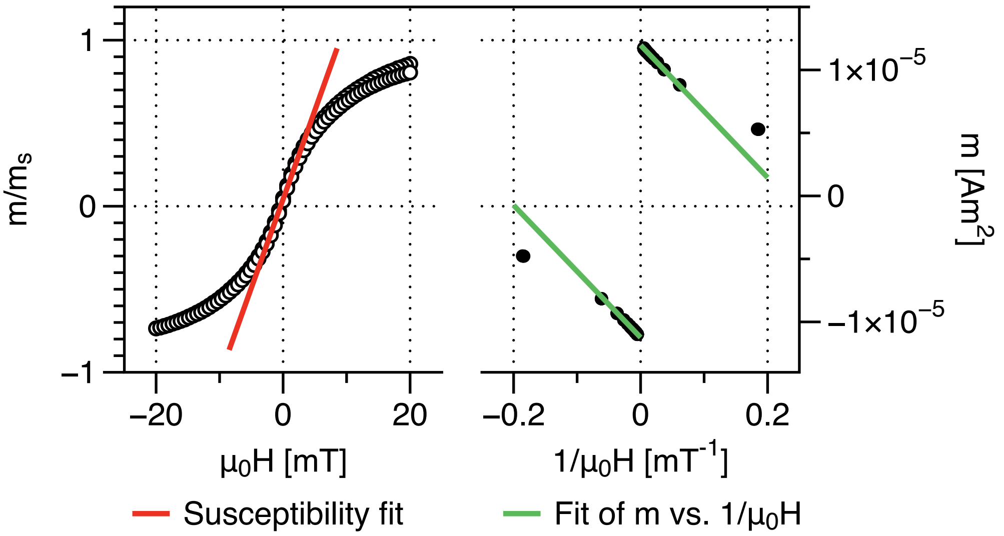

Figure B.1. (left) Slope of the linear magnetization region is the susceptibility, χ_0, and (right) the y-intercept from fitting *m* vs $1/\mu_0 H$ is the saturation moment, m_s, of the SPION dispersion.

Chantrell et al [43] used the lognormal size distribution to derive the following expression for the median diameter (d_o) of superparamagnetic nanoparticles:

$$d_0 = \left[\frac{18 k_b T}{\pi M_s}\sqrt{\left(\frac{\chi_0}{3m_s}\right)\left(\frac{1}{\mu_0 H_0}\right)}\right]^{\frac{1}{3}}$$

Eq. 7-1

where, $1/\mu_o H_o$ is the x-intercept from the linear fit of m vs. $1/\mu_o H$ in Figure B.1. The standard deviation, σ, of the lognormal distribution is expressed as:

$$\sigma = \frac{\left[\ln\left(\frac{3\chi_0}{m_s\left(\frac{1}{\mu_0 H_0}\right)}\right)\right]^{\frac{1}{2}}}{3}$$

Eq. 7-2

The effect of size distribution on the magnetization response is illustrated in Figure B.2. The magnetization curves shown are actual measurements from SPION samples with similar median diameters. In general, a broader size distribution deteriorates the overall magnetization response – lower susceptibility and saturation are observed when σ ~ 0.5 vs. 0.3 in Figure B.2.

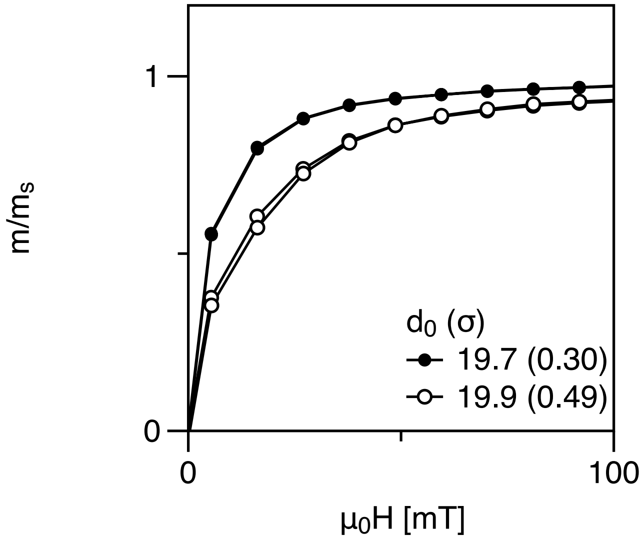

Figure B.2. Magnetization curves of two SPION samples with similar median diameters but different size distributions. For clarity, only the positive quadrant of the magnetization measurement is shown.

Note that the median diameter in Eq. 7-1 is volume weighted and reflects the median magnetic core diameter; as a result, it is difficult to resolve individual nanoparticle cores in an ensemble that consists of aggregated nanoparticles because each aggregate behaves like one large nanoparticle. Secondly, at very high concentrations, nanoparticles can magnetically interact; hence, it is critical that the VSM measurement is done in a non-aggregating and fairly dilute dispersion of nanoparticles. The results of the fitting shown in Figure B.1 are summarized in Figure B.3 – SPIONs have a 17 nm median diameter and a standard deviation of 0.2. The solid line shows that the Langevin function constructed using the same parameters fits the experimental data (filled circles) well.

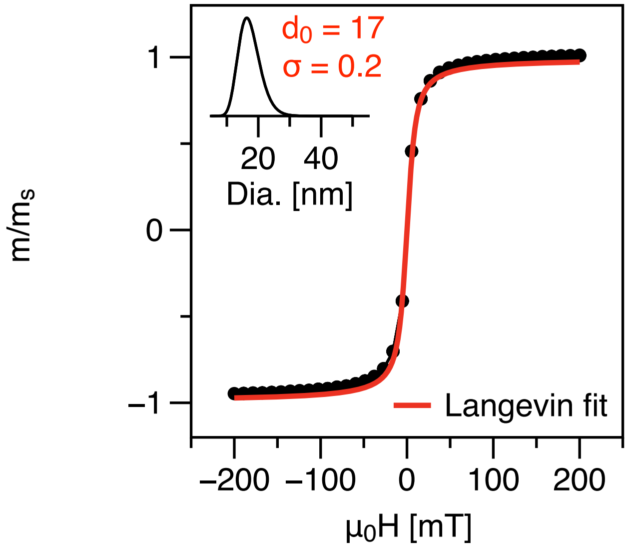

Figure B.3. Langevin function fitting to experimental data shows excellent agreement.

B.2 Size measurements using TEM

TEM images provide a direct visual characterization of the physical size of SPIONs; however, unlike VSM measurements that measure the entire sample in a dispersed state, TEM measures only a fraction of the sample visible in the images. Nevertheless, it is possible to analyze several hundreds of particles using digital counting methods, such as the particle size analysis plugin available in the imageJ software. TEM analysis of the same sample characterized above in Figure B.3. is shown in Figure B.4. The results show that the TEM size is slightly larger than the VSM size, which is probably due to the VSM not accounting for the layer of disordered surface spins [108]. Secondly, TEM size measurements are number weighted since particles are individually counted; on the other hand, since VSM measures the magnetic moment of the particles – a volume dependent property – the size is volume weighted. In summary, the contribution of a given size of particles in a number weighted distribution is proportional to d_c, while in the volume distribution the contribution is proportional to d_c^3.

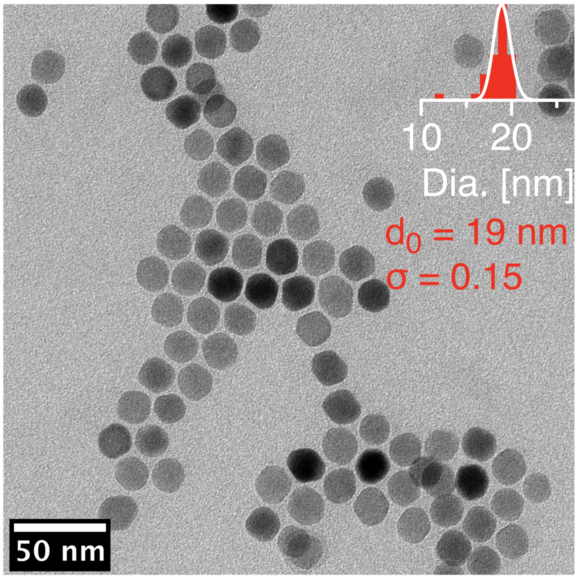

Figure B.4. TEM image of the sample characterized in Figure B.3; the median diameter, which is number weighted, is 19 nm and the standard deviation of the lognormal distribution is 0.15. In contrast, VSM analysis derives a 17 nm volume weighted median diameter with a 0.2 standard deviation.

B.3 Size measurements using DLS

Unlike VSM and TEM measurements, DLS measures the hydrodynamic diameter of SPIONs. Briefly, the hydrodynamic diameter is the total size of the SPIONs that diffuses when dispersed in water, which includes the polymer shell, and often the hydration layer that is bound strongly to hydrodphilic polymer chains such as PEG. DLS actually relates the Brownian diffusion of particles to the particle size – bigger particles diffuse slower than smaller ones. The hydrodynamic diameter d_h is given by the Stoker-Einstein equation:

$$d_h = \frac{k_b T}{3\pi\eta D}$$

Eq. 7-3

where, η is the carrier fluid's viscosity (η_{water} = 1 x 10^{-3} Pa s) and D is the translational diffusion coefficient of the particles. The Zetasizer Nano S DLS instrument from Malvern shines a laser on particles and measures the intensity of scattered light using a time-correlator. The latter constructs a correlogram of intensity as a function of time, which the software runs through various algorithms to determine the diffusion coefficient; typically, the intensity correlation as a function of time drops of faster for smaller particles than bigger ones. The software processes the data and presents the data as an intensity distribution, which is proportional to d_h^6, as derived from the Rayleigh scattering approximation [109]. Due to the d_h^6 dependence, the contribution from bigger particles dominates the signal and a lot of information in the smaller size particles is often unresolved; hence, it is important to look at volume and number weighted distributions as well to get a complete picture of the nanoparticles in the dispersion. The software converts the intensity-weighted distribution into volume (~ d_h^3) and number-weighted distributions (~ d_h). The final data consists of all three distributions, and in perfectly monodisperse samples, all three distributions align perfectly together; however, in real dispersions with a relatively monodisperse size distribution, the intensity distribution is skewed furthest to bigger sizes, followed by volume and number distributions, respectively. DLS data of the same sample characterized using TEM and VSM above is shown in Figure B.5. Note that the intensity distribution only indicates a single size distribution with an average diameter of 86 nm, but the volume distribution shows the presence of some aggregates as indicated by the shoulder located at larger sizes. Furthermore, the number distribution suggests that the actual number of aggregates is fairly small due to the predominant single peak at ~ 40 nm.

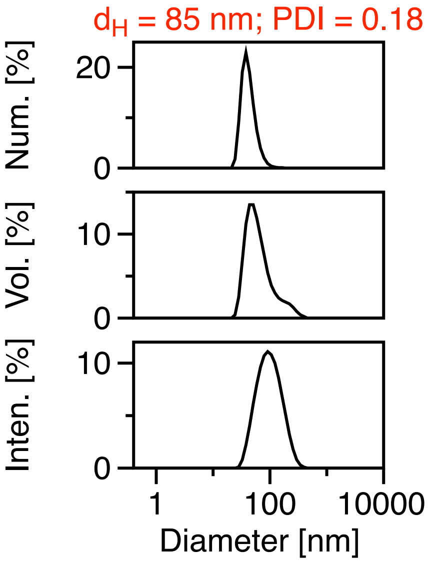

Figure B.5. Intensity, volume and number-weighted distributions obtained from a DLS measurement shows the sample has a uniform size distribution. The shoulder in the volume distribution shows the presence of clusters bigger than 100 nm; however, the actual number is relatively small as indicated by the single peak at ~40 nm in the number-weighted distribution.

C. Animal protocols

C.1 Justification

SPION tracers are designed for biomedical imaging and therapeutic applications in humans; thus, it is important to perform biodistribution and blood circulation studies to accurately determine the fate of the imaging tracers in living animals. SPIONs were tested in 8-week old female CD1 mice (Charles River).

C.2 Biodistribution study

The goal of this study was to determine the distribution of the tracers within the organs of the animals, and thus the ultimate fate of the tracers. Specifically, organs responsible for clearance of foreign materials, but not restricted to, from the body, such as liver, gall bladder, kidneys and spleen may be inspected. SPIONs were injected in a bolus form via the tail vein of the mouse using a 27 or 30-gauge needle. The injection volume was 100 µl and the SPION dose – characterized as low, medium or high – was either 2.5, 5 and 10 mg Fe_3O_4/kg body weight, respectively. Prior to injection, animals were restrained or sedated according to usual procedures provided in Animal Use Training Session and Mouse Lab Handouts. Mice were imaged in a 14 T Magnetic Resonance Imaging (MRI) scanner located at UW medicine's South Lake Union campus. Prior to imaging in the MRI scanner, 5% isoflurane anesthesia was administered in an induction chamber until mice were recumbent. During the imaging procedure, which typically took 15-30 minutes, isoflurane was maintained at 1-2% using a nose cone. The 14 T MRI's circulating water-bath gradient heater was used to provide thermal support to the mice. Once endpoint was reached, which ranged from 24 hours to 1 month depending on the study, mice were euthanized via CO_2 exposure as per standard IACUC methods. Additionally, cervical dislocation was performed as a secondary method of euthanasia.

Tissues were harvested and then fixed using 10% neutral buffered formalin for histology analysis.

C.3 Blood circulation study

The goal of this study was to determine the blood half-life of the SPIONs, and the time taken for complete blood clearance. For each SPION formulation tested, a total of 15 mice were required – see Table C.1. SPIONs were injected as a bolus in the tail vein of the mouse using a 27 to 30 gauge needle. The injection volume was 100 μl and the SPION concentration was 2.0 gFe/L. Prior to injection, animals were restrained or sedated according to usual procedures provided in Animal Use Training Session and Mouse Lab Handouts. From each mouse, blood was collected at 2 different time points to determine the iron concentration – see Table C.1 below for experimental design. The total collection volume was not to exceed 1% of the body weight. For example, 200 μl is the maximum allowed for a 20 g mouse. Retro-orbital bleeding under anesthesia (1-4% isoflurane) was used to collect blood samples at various time points. Mice were euthanized by isoflurane overdose, followed by cervical dislocation as the secondary method.

Table C.1: Experimental design for the blood circulation study. Each SPION formulation required a total of 10 mice (5 samples+5 controls), and each mouse was bled twice to get a total of 10 data points per SPION sample or 1x PBS control tested.

Blood collection time points (min)	**# of mice/SPION formulation**
Total of 10 data points PER formulation (e.g. time points shown)	**Formulation-1**
5,15	1 x 3 rep.
25,35	1 x 3 rep.
45,55	1 x 3 rep.
65,75	1 x 3 rep.
85,95	1 x 3 rep.
Total mice	**15**

BIBLIOGRAPHY

1. Gleich B, Weizenecker J. Tomographic imaging using the nonlinear response of magnetic particles. Nature. 2005;435:1214–7.

2. Kochanek KD, Xu J, Murphy SL, Miniño AM, Kung H-C. Deaths: Final Data for 2009. National Vital Statistics Reports. 2011;60.

3. Krishnan KM. Biomedical Nanomagnetics: A Spin Through Possibilities in Imaging, Diagnostics, and Therapy. IEEE T Magn. 2010;46:2523–58.

4. Katzberg RW, Haller C. Contrast-induced nephrotoxicity: Clinical landscape. Kidney Int. 2006;69:S3–S7.

5. Ix JH, Mercado N, Shlipak MG, Lemos PA, Boersma E, Lindeboom W, et al. Association of chronic kidney disease with clinical outcomes after coronary revascularization: The arterial revascularization therapies study (ARTS). Am Heart J. 2005;149:512–9.

6. Weinstein JS, Varallyay CG, Dosa E, Gahramanov S, Hamilton B, Rooney WD, et al. Superparamagnetic iron oxide nanoparticles: diagnostic magnetic resonance imaging and potential therapeutic applications in neurooncology and central nervous system inflammatory pathologies, a review. J Cerebr Blood F Met. 2010;30:15–35.

7. Neuwelt EA, Hamilton BE, Varallyay CG, Rooney WR, Edelman RD, Jacobs PM, et al. Ultrasmall superparamagnetic iron oxides (USPIOs): a future alternative magnetic resonance (MR) contrast agent for patients at risk for nephrogenic systemic fibrosis (NSF)? Kidney Int. 2009;75:465–74.

8. Sarin H. Physiologic upper limits of pore size of different blood capillary types and another perspective on the dual pore theory of microvascular permeability. J Angiogenes Res. 2010;2:14.

9. Lu M, Cohen MH, Rieves D, Pazdur R. FDA report: Ferumoxytol for intravenous iron therapy in adult patients with chronic kidney disease. Am J Hematol. 2010;85:315–9.

10. Ferguson RM, Minard KR, Krishnan KM. Optimization of nanoparticle core size for magnetic particle imaging. J Magn Magn Mater. 2009;321:1548–51.

11. Weizenecker J, Borgert J, Gleich B. A simulation study on the resolution and sensitivity of magnetic particle imaging. Phys Med Biol. 2007;52:6363–74.

12. Knopp T, Biederer S, Sattel TF, Erbe M, Buzug TM. Prediction of the Spatial Resolution of Magnetic Particle Imaging Using the Modulation Transfer Function of the Imaging Process. IEEE T Med Imaging. 2011;30:1284–92.

13. Ferguson RM, Khandhar AP, Krishnan KM. Tracer design for magnetic particle imaging (invited). J Appl Phys. 2012;111:07B318.

14. Goodwill PW, Tamrazian A, Croft LR, Lu CD, Johnson EM, Pidaparthi R, et al. Ferrohydrodynamic relaxometry for magnetic particle imaging. Appl Phys Lett. 2011;98:262502.

15. Marmor JB, Hahn N, Hahn GM. Tumor Cure and Cell Survival after Localized Radiofrequency Heating. Cancer Research. 1977;37:879–83.

16. Hahn GM. Hyperthermia for the Engineer: A Short Biological Primer. Biomed Eng. 1984.

17. Overgaard J. The current and potential role of hyperthermia in radiotherapy. International Journal of Radiation Oncology Biology Physics. 1989;16:535–49.

18. Jordan A, Scholz R, Wust P, Fähling H, Felix R. Magnetic fluid hyperthermia (MFH): Cancer treatment with AC magnetic field induced excitation of biocompatible superparamagnetic nanoparticles. J Magn Magn Mater. 1999;201:413–9.

19. Jordan A, Scholz R, Maier-Hauff K, Johannsen M, Wust P, Nadobny J, et al. Presentation of a new magnetic field therapy system for the treatment of human solid tumors with magnetic fluid hyperthermia. J Magn Magn Mater. 2001;225:118–26.

20. Ivkov R. Application of High Amplitude Alternating Magnetic Fields for Heat Induction of Nanoparticles Localized in Cancer. Clinical Cancer Research. 2005;11:7093s–7103s.

21. Moroz P, Jones SK, Gray BN. Magnetically mediated hyperthermia: current status and future directions. Int J Hyperther. 2002;18:267–84.

22. Hergt R, Hiergeist R, Zeisberger M, Glöckl G, Weitschies W, Ramirez LP, et al. Enhancement of AC-losses of magnetic nanoparticles for heating applications. J Magn Magn Mater. 2004;280:358–68.

23. Hilger I, Kießling A, Romanus E, Hiergeist R, Hergt R, Andrä W, et al. Magnetic nanoparticles for selective heating of magnetically labelled cells in culture: preliminary investigation. Nanotechnology. 2004;15:1027–32.

24. Byrne JD, Betancourt T, Brannon-Peppas L. Active targeting schemes for nanoparticle systems in cancer therapeutics. Adv Drug Deliver Rev. 2008;60:1615–26.

25. Fang J, Nakamura H, Maeda H. The EPR effect: Unique features of tumor blood vessels for drug delivery, factors involved, and limitations and augmentation of the effect. Adv Drug Deliver Rev. 2011;63:136–51.

26. Fortin J-P, Gazeau F, Wilhelm C. Intracellular heating of living cells through Néel relaxation of magnetic nanoparticles. Eur Biophys J. 2007;37:223–8.

27. Hilger I, Hergt R, Kaiser WA. Use of magnetic nanoparticle heating in the treatment of breast cancer. IEE Proc, Nanobiotechnol. 2005;152:33.

28. Hou C-H, Chen C-W, Hou S-M, Li Y-T, Lin F-H. The fabrication and characterization of dicalcium phosphate dihydrate-modified magnetic nanoparticles and their performance in hyperthermia processes in vitro. Biomaterials. 2009;30:4700–7.

29. Hergt R, Dutz S. Magnetic particle hyperthermia—biophysical limitations of a visionary tumour therapy. J Magn Magn Mater. 2007;311:187–92.

30. Cornell RM, Schwertmann U. The Iron Oxides: Structure, Properties, Reactions, Occurrences and Uses. 1996.

31. Kittel C. Physical theory of ferromagnetic domains. Reviews of Modern Physics. 1949;21:541–83.

32. Krishnan KM, Pakhomov AB, Bao Y, Blomqvist P, Chun Y, Gonzales M, et al. Nanomagnetism and spin electronics: materials, microstructure and novel properties. J Mater Sci. 2006;41:793–815.

33. Bedanta S, Kleemann W. Supermagnetism. J Phys D: Appl Phys. 2008;42:013001.

34. Mamiya H, Jeyadevan B. Hyperthermic effects of dissipative structures of magnetic nanoparticles in large alternating magnetic fields. Sci Rep. 2011;1:1–7.

35. Carrey J, Mehdaoui B, Respaud M. Simple models for dynamic hysteresis loop calculations of magnetic single-domain nanoparticles: Application to magnetic hyperthermia optimization. J Appl Phys. 2011;109:083921.

36. Stoner EC, EP W. A Mechanism of Magnetic Hysteresis in Heterogenous Alloys. Philosophical Transactions of the Royal Society of London Series A: Mathematical and Physical Sciences. 1948;240:599–642.

37. Tannous C, Gieraltowski J. The Stoner–Wohlfarth model of ferromagnetism. Eur J Phys. 2008;29:475–87.

38. Brown W. Thermal Fluctuations of a Single-Domain Particle. Phys Rev. 1963;130:1677–86.

39. Goya GF, Berquó TS, Fonseca FC, Morales MP. Static and dynamic magnetic properties of spherical magnetite nanoparticles. J Appl Phys. 2003;94:3520.

40. Luo W, Nagel SR, Rosenbaum TF, Rosensweig RE. Dipole Interactions with Random Anisotropy in a Frozen Ferrofluid. Physical Review Letters. 1991;67:2721–4.

41. Rosensweig RE. Heating magnetic fluid with alternating magnetic field. J Magn Magn Mater. 2002;252:370–4.

42. Řezníček R, Chlan V, Štěpánková H, Novák P, Maryško M. Magnetocrystalline anisotropy of magnetite. J Phys: Condens Matter. 2012;24:055501.

43. Chantrell RW, Popplewell J, Charles SW. Measurements of Particle Size Distribution Parameters in Ferrofluids. IEEE T Magn. 1978;14:975–8.

44. Fannin PC, Charles SW. Measurement of the Neel relaxation of magnetic particles in the frequency range 1 kHz to 160 MHz. J Phys D: Appl Phys. 1991;24:76–7.

45. Ferguson RM, Khandhar AP, Jonasson C, Blomgren J, Johansson C, Krishnan. Size-Dependent Relaxation Properties of Monodisperse Magnetite Nanoparticles Measured Over Seven Decades of Frequency by AC Susceptometry. IEEE T Magn. 49:3441–4.

46. Fannin PC. Investigating magnetic fluids by means of complex susceptibility measurements. J Magn Magn Mater. 2003;258-259:446–51.

47. Fannin PC, Mac Oireachtaigh C. Investigating the isotropic properties of a magnetic fluid following the removal of a polarising field. J Magn Magn Mater. 2007.

48. Kneller EF, Luborsky FE. Particle Size Dependence of Coercivity and Remanence of Single-Domain Particles. J Appl Phys. 1963;34:656.

49. Yoshida T, Enpuku K. Simulation and Quantitative Clarification of AC Susceptibility of Magnetic Fluid in Nonlinear Brownian Relaxation Region. Jpn J Appl Phys. 2009;48:127002.

50. Weizenecker J, Gleich B, Rahmer J, Dahnke H, Borgert J. Three-dimensional real-time in vivomagnetic particle imaging. Phys Med Biol. 2009;54:L1–L10.

51. Goodwill PW, Saritas EU, Croft LR, Kim TN, Krishnan KM, Schaffer DV, et al. X-Space MPI: Magnetic Nanoparticles for Safe Medical Imaging. Adv Mater. 2012;24:3870–7.

52. Rahmer J, Weizenecker J, Gleich B, Borgert J. Signal encoding in magnetic particle imaging: properties of the system function. BMC Med Imaging. 2009;9:4.

53. Goodwill PW, Conolly SM. The X-Space Formulation of the Magnetic Particle Imaging Process: 1-D Signal, Resolution, Bandwidth, SNR, SAR, and Magnetostimulation. IEEE T Med Imaging. 2010;29:1851–9.

54. Ferguson RM, Minard KR, Khandhar AP, Krishnan KM. Optimizing magnetite nanoparticles for mass sensitivity in magnetic particle imaging. Med Phys. 2011;38:1619–26.

55. Ferguson RM, Khandhar AP, Arami H, Hua L, Hovorka O, Krishnan KM. Tailoring the magnetic and pharmacokinetic properties of iron oxide magnetic particle imaging tracers. Biomed Tech. 2013;19:1–15.

56. Chantrell RW, Coverdale GN, Hilo El M, O'grady K. Modelling of interaction effects in fine particle systems. J Magn Magn Mater. 1996;157/158:250–5.

57. Mørup S, Hansen MF, Frandsen C. Magnetic interactions between nanoparticles. Beilstein J Nanotechnol. 2010;1:182–90.

58. Hansen MF, Mørup S. Models for the dynamics of interacting magnetic nanoparticles. J Magn Magn Mater. 1998;184:262–74.

59. Greish K. Enhanced Permeability and Retention (EPR) Effect for Anticancer Nanomedicine Drug Targeting. Methods Mol Biol. 2010. pp. 25–37.

60. Hume DA. The mononuclear phagocyte system. Current Opinion in Immunology. 2006;18:49–53.

61. Almeida JPM, Chen AL, Foster A, Drezek R. In vivo biodistribution of nanoparticles. Nanomedicine. 2011;6:815–35.

62. Cesta M. Normal Structure, Function, and Histology of the Spleen. Toxicologic Path. 2006;34:455–65.

63. Moghimi SM, Hunter AC, Murray JC. Long-Circulating and Target-Specific Nanoparticles: Theory to Practice. Pharmacological Reviews. 2001;53:283–318.

64. Fang C, Shi B, Pei Y-Y, Hong M-H, Wu J, Chen H-Z. In vivo tumor targeting of tumor necrosis factor-α-loaded stealth nanoparticles: Effect of MePEG molecular weight and particle size. Eur J Pharm Sci. 2006;27:27–36.

65. Cole AJ, David AE, Wang J, Galbán CJ, Hill HL, Yang VC. Polyethylene glycol modified, cross-linked starch-coated iron oxide nanoparticles for enhanced magnetic tumor targeting. Biomaterials. 2011;32:2183–93.

66. Jokerst JV, Lobovkina T, Zare RN, Gambhir SS. Nanoparticle PEGylation for imaging and therapy. Nanomedicine. 2011;6:715–28.

67. Albanese A, Tang PS, Chan WCW. The Effect of Nanoparticle Size, Shape, and Surface Chemistry on Biological Systems. Annu Rev Biomed Eng. 2012;14:1–16.

68. Bourrinet P, Bengele HH, Bruno B, Anne D, Idee J-M, Jacobs PM, et al. Preclinical Safety and Pharmacokinetic Profile of Ferumoxtran-10, an Ultrasmall Superparamagnetic Iron Oxide Magnetic Resonance Contrast Agent. Invest Radiol. 2006;41:313–24.

69. Chouly C, Poliquen D, Lucet I, J JJ, Jallet P. Development of superparamagnetic nanoparticles for MRI: effect of particle size, charge and surface nature on biodistribution. J Microencapsul. 1996;13:245–55.

70. Metz S, Bonaterra G, Rudelius M, Settles M, Rummeny E, Daldrup-Link H. Capacity of human monocytes to phagocytose approved iron oxide MR contrast agents in vitro. Eur Radiol. 2004;14:1851–8.

71. Matuszewski L, Persigehl T, Wall A, Schwindt W, Tombach B, Fobker M, et al. Cell Tagging with Clinically Approved Iron Oxides: Feasibility and Effect of Lipofection, Particle Size, and Surface Coating on Labeling Efficiency. Radiology. 2005;235:155–61.

72. Owens DE III, Peppas NA. Opsonization, biodistribution, and pharmacokinetics of polymeric nanoparticles. Int J Pharm. 2006;307:93–102.

73. Alexis F, Pridgen E, Molnar LK, Farokhzad OC. Factors Affecting the Clearance and Biodistribution of Polymeric Nanoparticles. Mol Pharm. 2008;5:505–15.

74. Storm G, Belliot SO, Daemen T, Lasic DD. Surface modification of nanoparticles to oppose uptake by the mononuclear phagocyte system. Adv Drug Deliver Rev. 1995;17:31–48.

75. Aggarwal P, Hall JB, McLeland CB, Dobrovolskaia MA, McNeil SE. Nanoparticle interaction with plasma proteins as it relates to particle biodistribution, biocompatibility and therapeutic efficacy. Adv Drug Deliver Rev. 2009;61:428–37.

76. Shuai X, Merdan T, Unger F, Wittmar M, Kissel T. Novel Biodegradable Ternary Copolymers hy-PEI- g-PCL- b-PEG: Synthesis, Characterization, and Potential as Efficient Nonviral Gene Delivery Vectors. Macromolecules. 2003;36:5751–9.

77. Plank C, Vlaskou D, Schillinger U, Mykhaylyk O. Research Spotlight: Magnetofection™ platform: from magnetic nanoparticles to novel nucleic acid therapeutics. Therapeutic Delivery. 2011;2:717–26.

78. Gong P, Grainger DW. Nonfouling surfaces: A review of principles and applications for microarray capture design assays. In: Rampal JB, editor. Microarrays Volume 1: Synthesis Methods. 2nd ed. 2007. pp. 59–92.

79. Chantrell R, Walmsley N, Gore J, Maylin M. Calculations of the susceptibility of interacting superparamagnetic particles. Phys Rev B. 2000;63:024410.

80. Crocombette JP, Pollak M, Jollet F, Thromat N, Gautier-Soyer M. X-ray-absorption spectroscopy at the Fe L2,3 threshold in iron oxides. Phys Rev B. 1995;52:3143–50.

81. Pellegrino T, Manna L, Kudera S, Liedl T, Koktysh D, Rogach AL, et al. Hydrophobic Nanocrystals Coated with an Amphiphilic Polymer Shell: A General Route to Water Soluble Nanocrystals. Nano Lett. 2004;4:703–7.

82. Atici OG, Akar A, Rahmian R. Modification of Poly(maleic anhydride-co-styrene) with Hydroxyl Containing Compounds. Turk J Chem. 2001;25:259–66.

83. Yu WW, Chang E, Sayes CM, Drezek R, Colvin VL. Aqueous dispersion of monodisperse magnetic iron oxide nanocrystals through phase transfer. Nanotechnology. 2006;17:4483–7.

84. Knop K, Hoogenboom R, Fischer D, Schubert US. Poly(ethylene glycol) in Drug Delivery: Pros and Cons as Well as Potential Alternatives. Angew Chem Int Ed. 2010;49:6288–308.

85. Gref R, Luck M, Quellec P, Marchand M, Dellacherie E, Harnish S, et al. “Stealth” corona-core nanoparticles surface modified by polyethylene glycol (PEG): influences of the corona (PEG chain length and surface density) and of the core composition on phagocytic uptake and plasma protein adsorption. Colloid Surface B. 2000;18:301–13.

86. Maldiney T, Richard C, Seguin J, Wattier N, Bessodes M, Scherman D. Effect of Core Diameter, Surface Coating, and PEG Chain Length on the Biodistribution of Persistent Luminescence Nanoparticles in Mice. ACS Nano. 2011;5:854–62.

87. Häfeli UO, Riffle JS, Harris-Shekhawat L, Carmichael-Baranauskas A, Mark F, Dailey JP, et al. Cell Uptake and in Vitro Toxicity of Magnetic Nanoparticles Suitable for Drug Delivery. Mol Pharm. 2009;6:1417–28.

88. Raynal I, Prigent P, Peyramaure S, Najid A, Rebuzzi C, Corot C. Macrophage Endocytosis of Superparamagnetic Iron Oxide Nanoparticles. Invest Radiol. 2004;39:56–63.

89. Golovko DM, Henning T, Bauer JS, Settles M, Frenzel T, Mayerhofer A, et al. Accelerated stem cell labeling with ferucarbotran and protamine. Eur Radiol. 2009;20:640–8.

90. Mailänder V, Lorenz MR, Holzapfel V, Anna M, Karin F, Markus W, et al. Carboxylated Superparamagnetic Iron Oxide Particles Label Cells Intracellularly Without Transfection Agents. Mol Imaging Biol. 2008;10:138–46.

91. Eberbeck D, Wiekhorst F, Wagner S, Trahms L. How the size distribution of magnetic nanoparticles determines their magnetic particle imaging performance. Appl Phys Lett. 2011;98:182502.

92. Khandhar AP, Ferguson RM, Krishnan KM. Monodispersed magnetite nanoparticles optimized for magnetic fluid hyperthermia: Implications in biological systems. J Appl Phys. 2011;109:07B310.

93. Sosinowski T, Pandey A, Dixit VM, Weiss A. Src-like Adaptor Protein (SLAP) Is a Negative Regulator of T Cell Receptor Signaling. J Exp Med. 2000;191:463–73.

94. Khandhar AP, Ferguson RM, Simon JA, Krishnan KM. Tailored magnetic nanoparticles for optimizing magnetic fluid hyperthermia. J Biomed Mater Res. 2011;100A:728–37.

95. Rabin Y. Is intracellular hyperthermia superior to extracellular hyperthermia in the thermal sense? Int J Hyperther. 2002;18:194–202.

96. Khandhar AP, Ferguson RM, Arami H, Krishnan KM. Monodisperse magnetite nanoparticle tracers for in vivo magnetic particle imaging. Biomaterials. 2013;34:3837–45.

97. Mitchell MD, Kundel HL, Axel L, Joseph PM. Agarose as a tissue equivalent phantom material for NMR imaging. Magn Reson Imaging. 1986;4:263–6.

98. Reimer P, Balzer T. Ferucarbotran (Resovist): a new clinically approved RES-specific contrast agent for contrast-enhanced MRI of the liver: properties, clinical development and applications. Eur Radiol. 2003;13:1266–76.

99. Briley-S b K, Hustvedt S-O, Haldorsen A, Bj rnerud A. Long-term imaging effects in rat liver after a single injection of an iron oxide nanoparticle based MR contrast agent. J Magn Reson Imaging. 2004;20:622–31.

100. Beard JL, Dawson H, Piñero DJ. Iron metabolism: a comprehensive review. Nutr Rev. 1996;54:295–317.

101. Richardson DR, Ponka P. The molecular mechanisms of the metabolism and transport of iron in normal and neoplastic cells. Biochimica et Biophysica Acta. 1997;1331:1–40.

102. Kondo H, Saito K, Grasso J, Aisen P. Iron metabolism in the erythrophagocytosing Kupffer cell. Hepatology. 1988;8:32–8.

103. Briley-Saebo K, Johansson L, Hustvedt S-O, Haldorsen A, Bjornerod A, Fayad Z, et al. Clearance of Iron Oxide Particles in Rat Liver. Invest Radiol. 2006;41:560–71.

104. Majumdar S, Zoghbi SS, Gore JC. Pharmocokinetics of superparamagnetic iron-oxide MR contrast agents in the rat. Invest Radiol. 1990;25:771–7.

105. Weissleder R, Bogdanov A, Neuwelt EA, Papisov M. Long-circulating iron oxides for MR imaging. Adv Drug Deliver Rev. 1995;16:321–34.

106. Jana NR, Chen Y, Peng X. Size- and Shape-Controlled Magnetic (Cr, Mn, Fe, Co, Ni) Oxide Nanocrystals via a Simple and General Approach. Chem Mater. 2004;16:3931–5.

107. Kalele S, Narain R, Krishnan KM. Probing temperature-sensitive behavior of pNIPAAm-coated iron oxide nanoparticles using frequency-dependent magnetic measurements. J Magn Magn Mater. 2009;321:1377–80.

108. Pal S, Dutta P, Shah N, Huffman GP, Seehra MS. Surface Spin Disorder in Fe3O4 Nanoparticles Probed by Electron Magnetic Resonance Spectroscopy and Magnetometry. IEEE T Magn. 2007;43:3091–3.

109. Tech Note: Dynamic Light Scattering: An Introduction in 30 Minutes. 2005;:1–8.